MEASUREMENT OF THE PARITY-VIOLATING SPIN-ROTATION OF POLARIZED NEUTRONS PROPAGATING THROUGH LIQUID HELIUM

Christopher Dale Bass

Submitted to the faculty of the University Graduate School
in partial fulfillment of the requirements
for the degree
Doctor of Philosophy
in the Department of Physics,
Indiana University
February 2008

Accepted by the Graduate Faculty, Indiana University, in partial fulfillment of the requirement for the degree of Doctor of Philosophy.

Doctoral Committee

_____

William M. Snow, Ph.D.

_____

Hermann Nann, Ph.D.

_____

Adam Szczepaniak, Ph.D.

_____

Rex Tayloe, Ph.D.

February 08, 2008

Acknowledgements

I would like to acknowledge the financial support from the National Science Foundation grant NSF PHY-0457219 supporting the Neutron Spin Rotation project, and the Department of Commerce through the NIST Neutron Interactions and Dosimetry Group at the NCNR in Gaithersburg, Maryland.

This thesis would not have been possible without the support of many people. I first want to thank my advisor Professor Mike Snow for reading my numerous revisions and helping make sense of the confusion. He offered motivation and guidance throughout my graduate career.

I want to thank the members of my thesis committee, Professor Hermann Nann, Professor Adam Szczepaniak, and Professor Rex Tayloe for taking the time to work with me during this endeavor. I am grateful for the help from numerous people in the IU physics department, at IUCF, and at the NIST Neutron Interactions and Dosimetry Group over the course of the spin rotation project. I spent many hours at the IU Swain Hall physics machine shop consulting with Phil Childress. Without his help and patience, this experiment might not have become a reality. Bill Lowsowski was also extremely helpful and had parts to spare when we needed them. Jay MacFarland at IUCF computer support arranged for extended use of laptops when I was in Bloomington so that I could work on the thesis. Cathi Eagan and the McNair Scholars Program provided financial and well-timed emotional support throughout my graduate career. I am still indebted to her for keeping me in school after I dropped out in my second year.

I would like to thank all of the collaboration members – past and present – who helped me understand what exactly we were actually trying to accomplish with all that liquid helium and expensive-looking apparatus. They were extremely helpful in preparation of this thesis and provided me with graphs, plots, explanations and the occasional diversion as needed for sanity. I especially want to thank Diane Markoff. She endured the previous neutron spin-rotation experiment, wrote her thesis, and survived to

tell the tale. I regard her thesis as the benchmark for evaluating my own thesis for this incarnation of the experiment, and that mark is set high. It was because of her attention to detail that every time I read her thesis during my years on the project, I was able to understand a little more about the experiment, and so my own thesis became more comprehensible.

Finally, I would like to thank (and apologize to) my fiancée, Tiffany. Not only did she begin my caffeine addiction, but she spent countless nights listening to my ravings about the experiment and this paper, and cheering me up in general. She kept me focused on the reasons why I was writing the thesis in the first place. Tiffany sacrificed many hours of family time so that I could work on the thesis and we that could move beyond graduate school. She endured this long process with me, always offering support, love and offerings of espresso.

Christopher Dale Bass

MEASUREMENT OF THE PARITY-VIOLATING SPIN ROTATION OF POLARIZED NEUTRONS PROPAGATING THROUGH LIQUID HELIUM

In the forward elastic scattering of transversely polarized neutrons propagating through a medium, the most prominent parity-violating observable is the rotation of the neutron spin vector about its momentum vector, which is due to the nucleon-nucleon (NN) weak interaction. A phenomenological model for the NN weak interaction uses nucleons and mesons as the important degrees of freedom, but values for the nucleon-meson weak coupling amplitudes are not well constrained by measurement or theory. A measurement of the parity-violating spin rotation of cold neutrons passing through liquid helium enables a quantitative theoretical interpretation of the poorly-understood properties of the NN weak interaction. Additionally, parity-violating neutron spin rotation in liquid helium is sensitive to the weak neutral current, which is not well-known from the current nuclear data set.

The measurement is conducted by introducing a liquid helium target between a neutron polarizer/analyzer pair and manipulating the target and neutron spin to isolate the parity-violating rotation in the presence of much larger parity-conserving rotations due to residual magnetic fields. A previous measurement was performed in 1996 at the NIST Center for Neutron Research in Gaithersburg, Maryland with the result

$$\varphi_{PV}\left(n,\ ^4He\right) = (8.0 \pm 14[\text{stat}] \pm 2.2[\text{syst}]) \times 10^{-7}\ \text{rad/m}$$

We describe a redesigned apparatus that can use superfluid helium to increase statistics and the installation of additional magnetic shielding to reduce systematics in an effort to reach a sensitivity goal of 3×10^{-7} rad/m at NIST with an upper bound of 1×10^{-7} rad/m on systematic effects. We describe the apparatus, the design of the new liquid helium target, and show preliminary data from this ongoing experiment.

Table of Contents

List of Figures

List of Tables

1 Introduction

Symmetries and their associated conservation laws offer physicists a powerful tool for simplifying model calculations or gaining a deeper understanding of incomplete theories. A symmetry is an operation that can be performed on a system that leaves it invariant. Some symmetries are formulated from principle, such as the invariance of the laws of physics with respect to choice of coordinate origin, while other symmetries are based on experimental observations, such as baryon number conservation. Symmetries and conservation laws allow mathematical modeling of fundamental interactions without requiring detailed knowledge of the underlying dynamics of a process.

Mathematically, symmetries are related to conservation laws through Noether's theorem [1], which essentially states that every symmetry in nature yields a conservation law, and vice versa. For example, linear momentum conservation is related to symmetry with respect to translations in space, energy conservation is related to symmetry with respect to translations in time, and angular momentum conservation is related to symmetry with respect to rotations.

For symmetry of a system to inversion through a coordinate origin, the conserved quantity is parity: $P(\hat{r}) \rightarrow (-\hat{r})$. In a parity-transformed system, both the coordinate vector $\vec{r}$ and the linear momentum vector $\vec{p}$ change sign, but the angular momentum $\vec{\ell}$ remains unchanged, since $\vec{\ell} = \vec{r} \times \vec{p}$ is an axial vector (pseudovector) which is invariant under parity transformation. So for nonrelativistic systems, the spin vector $\vec{S}$ remains unchanged, since $\vec{S}$ commutes with the total angular momentum $\vec{j}$, which also commutes with angular momentum $\vec{\ell}$. A process conserves parity if the interaction cross-sections and rates involving the mirror system are identical to those involving the original system. Figure 1.1 shows an example of a parity-violating system: the beta decay of a polarized nucleus.

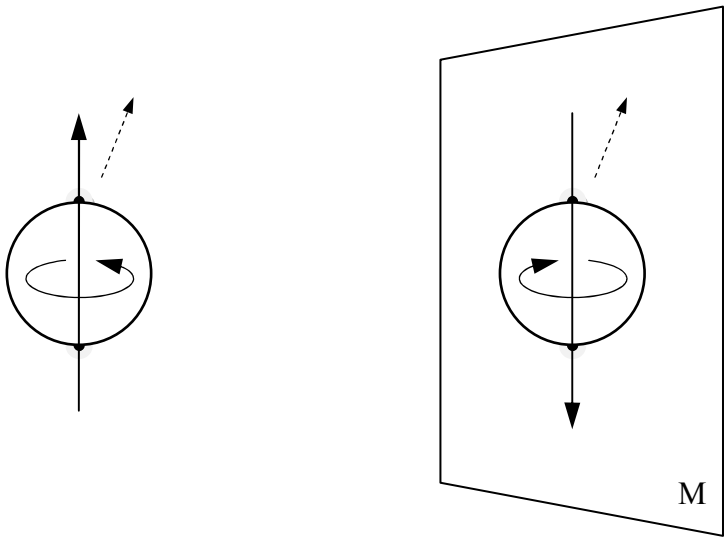

Figure 1.1: Beta decay of a polarized nucleus and its parity-transformed mirror image.

The groundbreaking work by Lee and Yang [2], and the experimental study of beta decay by Wu *et al*. [3] carried out at the National Bureau of Standards demonstrate that the weak interaction violates parity and does so maximally. In contrast, the electromagnetic and strong interactions conserve parity to the extent that they have been measured. The weak interaction is also distinguished from electromagnetic and strong interactions by flavor non-conservation; flavor is the quantum number that identifies each type of quark: up, down, charm, strange, top, and bottom. In electromagnetic and strong interactions, the total number of each type of quark is conserved, but in weak interactions, flavor is not necessarily conserved.

It is through flavor and parity violation that the weak interaction has mostly been studied. In leptonic and semileptonic systems, the weak interaction is well understood because electromagnetic and strong forces can be effectively suppressed or eliminated from theoretical calculations and experimental measurements, since interactions are occurring between individual leptons. However, the situation changes for hadronic

systems, since their composite nature introduces significant strong-interaction dynamics that are not completely understood. Nevertheless, since the strong interaction conserves flavor, the weak interaction can be studied directly in hadronic systems through channels that demonstrate flavor violation. Unfortunately, this method of investigation is not an option for weak hadronic processes that conserve flavor.

Since the strength of the weak interaction amplitude is smaller than the strong nuclear amplitude by approximately 10^6, study of the flavor-conserving hadronic weak interaction must in practice measure parity-violating observables. One example of a parity-violating observable in a hadronic system is the transverse rotation of a neutron spin vector about its momentum vector as it travels through an unpolarized medium. This small, parity-violating rotation (on the order of 10^{-5} radians), was first observed in heavy isotopes of tin and lanthanum using low energy neutrons (~10^{-3} eV) [4, 5]. However, the nuclear structure calculations in heavy elements can be difficult and inhibit the ability to extract hadronic weak interaction information from these systems. Therefore, there is great interest in studying neutron spin rotation in light nuclear systems, where the nuclear structure is theoretically more tractable. However, the relative theoretical simplicity of $A < 5$ systems is countered by an experimental disadvantage: the neutron spin-rotation signal is smaller than that in the heavier systems.

The hadronic weak interaction is worth understanding for a number of reasons. Assuming that electroweak theory is correct, a study of the nucleon-nucleon (NN) weak interaction may improve our understanding of the strongly interacting limit of quantum chromodynamics (QCD), which is clearly a problem of fundamental importance. Like the electromagnetic interaction, the weak interaction between quarks and leptons is understood at the fundamental level, and it is weak enough to probe strongly-interacting systems without affecting the dynamics. However, in hadrons the weak interaction between quarks competes directly with the strong interaction between quarks, which is larger in amplitude by a factor of 10^6 for low-energy processes. Furthermore, these

hadronic weak interactions have shown strange features that have been observed for decades without explanation.

One such oddity is the $\Delta I = 1/2$ rule in the strangeness-changing ($\Delta S \neq 0$) hadronic weak processes. Strong interaction effects appear to boost the $\Delta I = 1/2$ hadronic weak amplitudes relative to the $\Delta I = 3/2$ channel by more than an order of magnitude, despite the fact that these amplitudes are comparable in the perturbative QCD limit and from the viewpoint of chiral symmetry. In addition, there are nonleptonic hyperon decays, whose isospin dependence looks nothing like what one would expect from the symmetries of QCD. In both cases, we must conclude that there is some nontrivial aspect of QCD dynamics at work.

A question that arises is if the unexplained phenomena are due to the presence of the strange quark, or if they are a more general feature of QCD for all light quarks. Measurements of quark-quark weak interactions in systems without strange quarks are needed to investigate this question. In practice, NN weak processes are the only known possibility to do this. We then ask if the isospin dependence of the NN weak interaction is simple or if there are amplifications of one channel over the other [6]. There are already hints from experiment that the $\Delta I = 1$ NN weak interaction is suppressed for some reason.

Additionally, the NN weak interaction is the only practical way to study quark-quark neutral weak currents at low energy. The neutral weak current conserves quark flavor to high accuracy in electroweak theory due to the Glashow-Iliopoulos-Maiani (GIM) mechanism [7], in which the charged weak current couples $u \leftrightarrow d'$ or $c \leftrightarrow s'$. The quark states d' and s' are orthogonal combinations of the mass eigenstates of quarks of flavor d and s, where the quark mixing is parameterized by the Cabibbo mixing angle θ_C:

$$\begin{pmatrix} d' \\ s' \end{pmatrix} = \begin{pmatrix} \cos\theta_C & \sin\theta_C \\ -\sin\theta_C & \cos\theta_C \end{pmatrix} \begin{pmatrix} d \\ s \end{pmatrix} \tag{1.1}$$

Thus, neutral weak currents are not seen in the well-studied $\Delta S \neq 0$ hadronic weak decays. Little is known from experimental measurements about how QCD modifies neutral weak currents, except from high-energy collider experiments [8-12], where in the high-energy limit, perturbative QCD is valid, and theory and experiment agree.

In other fields, knowledge of the NN weak interaction could be used with the large body of experimental information on parity violation in nuclei to address important issues in nuclear physics. For example, measurements of parity violation in atoms have revealed effects due to the NN weak interaction through the observation of the nuclear anapole moment in ^{133}Cs [13]. The nuclear anapole moment is a parity-violating radiative correction of order αG_F (α is the fine structure constant and G_F is the Fermi coupling constant, which give the strengths of the electromagnetic and weak couplings, respectively), which is amplified in heavy nuclei. This ground-state property of nuclei can be calculated in a relatively model-independent manner like the magnetic moment of a nucleus, and measurements in other atoms are progress. However, in order to use measurements of the anapole moment to probe nuclear structure, the NN weak interaction itself must be understood.

Unfortunately, the rate of progress of understanding the NN weak interaction has been slow despite strong experimental activity. Three reviews of the subject conducted over two decades [6, 14, 15] reach essentially the same conclusion: most of the parameters that describe the couplings in NN weak interaction are unknown. The reasons for the slow advance are both theoretical and experimental. The experimental problems stem from the small size of weak amplitudes relative to strong amplitudes (typically $\sim 10^{-6}$ at low energies). Theoretical difficulties are encountered in trying to relate the underlying electroweak currents to low-energy observables in the strongly interacting regime of QCD. One expects the strong repulsion in the NN interaction to keep the nucleons too far apart for a simple direct exchange of W and Z bosons between quarks in

different nucleons to represent an accurate dynamical mechanism. Therefore, one must understand the physics of strong QCD at the one- and two-nucleon levels.

A recent approach has appeared due to Liu, Ramsey-Musolf, Holstein, and others [6, 16-18]. In this approach, the NN weak interaction is parameterized in the language of chiral effective field theory, where the Lagrangian can be expanded order by order in terms of the typical momentum transfer relevant to a parity-violating process divided by the scale of the expansion (the hadronic scale $\Lambda_{HAD} \approx 1$ GeV). Each operator possesses an unknown dimensionless constant. The purpose of experiment is to determine these constants. Once the constants are determined, other weak processes can be calculated. This approach is general in that it incorporates all the known symmetries of QCD.

An earlier approach maps QCD to an effective theory that is expressed in terms of the important degrees of freedom in low-energy QCD: mesons and nucleons. Desplanques, Donoghue and Holstein (DDH) [19] carried out this program in the QCD bag model and mapped it onto a meson exchange model, where the effects of quark-quark weak currents appear as parity-violating nucleon-meson couplings. A meson exchange model is known to work well as a low-energy description of the strong interaction [20]. Even if it is not an honest representation of the NN interaction at the quark level, it is at least a convenient way of encoding the amplitudes.

This effective theory is used to calculate electroweak effects in the NN interaction, and then determine the weak couplings from experiment. If the values of the couplings inferred from different experiments are consistent, then the results can confidently be used to improve understanding of nuclear parity-violation. For this application, the parity-violating coupling of the pion is important to understand, since it produces the longest-range effect. If the meson exchange model fails, then something interesting will have been learned: the strongly interacting limit of QCD would demand explanation.

The DDH meson exchange model characterizes the NN weak interaction with six weak nucleon-meson couplings constants: f_π, h_ρ^0, h_ρ^1, h_ρ^2, h_ω^0, and h_ω^1, where the

superscripts describe the isospin transition and the subscripts denote the meson exchanged. DDH used a variety of theoretical techniques to determine a "reasonable range" and "best value" for each of these amplitudes [19], which now serve as valuable guides for experimental investigations.

The strength of one of these coupling constants, the isovector coupling f_π, should be a direct measure of the neutral current contribution of the NN weak interaction and has been calculated in various models. The quark model-based DDH calculation [19] and a recent update [21] showed that strange quark contributions to f_π were important. Recent calculations in Skyrme models show this effect explicitly: the two-flavor calculation gives a value for f_π which is nearly an order of magnitude smaller than the result for three flavors [22]. This confirms an earlier estimate made with chiral Lagrangians [23]. Predictions for the value of f_π from DDH, the Skyrme model, and a recently corrected QCD sum rule calculation [24] all range from 1.5 to 3.0×10^{-7}.

Experimentally, the size of f_π is not known [19, 21, 25-31]. The most reliable information on the size of f_π is believed to come from measurements of the circular polarization of 1081 keV gamma rays from ^{18}F [14]. The current results have been interpreted as an upper limit: $f_\pi \leq 1.3 \times 10^{-7}$. One theoretical calculation extracts from the ^{133}Cs nuclear anapole moment measurement a value of $f_\pi = 9.5 \pm 2.1(\text{expt}) \pm 3.5(\text{theory}) \times 10^{-7}$ [32], which is significantly larger than the ^{18}F value. However, there are nuclear structure uncertainties involved and it is too soon to draw a firm conclusion [33].

A measurement in the NN system sensitive to f_π is needed to determine its value beyond a reasonable doubt. The system must be simple enough so that calculations can reliably connect experimental observables to weak nucleon-meson couplings. In practice, this means that one must perform experiments in light nuclear systems, such as *p*, *d*, ^{3}He, or ^{4}He. One such experiment is the measurement of the parity-violating neutron spin

rotation through liquid helium. This experiment is sensitive to the isovector coupling f_π and a linear combination of the isoscalar couplings.

A previous measurement of the parity-violating neutron spin rotation through liquid helium performed at NIST in 1996 measured [34]:

$$\varphi_{PV}\left(\vec{n},\ ^4\mathrm{He}\right) = (8.0 \pm 14[\mathrm{stat}] \pm 2.2[\mathrm{syst}]) \times 10^{-7}\ \mathrm{rad/m}$$

This result was unable to resolve the conflict between measurements of weak nucleon-meson coupling constants from different nuclear systems.

This thesis describes an experiment to measure the parity-violating spin-rotation signal from transversely polarized low-energy neutrons that travel through liquid helium to a precision of $3 \times 10^{-7}\ \mathrm{rad/m}$. The theoretical motivation for performing the measurement as well as the relationship between the spin-rotation observable and the low-energy NN weak interaction model are presented. The apparatus and the data acquisition methodology are described, with emphasis given to the development and performance of the liquid helium target. The current results of the spin-rotation measurement for this ongoing experiment are given with a discussion of the systematic and statistical errors.

2 The Nucleon-Nucleon Weak Interaction

A detailed study of hadronic weak interactions can only develop from detailed knowledge of the structure of hadrons and the dynamics of their constituent particles. In principle, this knowledge may be obtained from QCD. In QCD, quark-quark couplings are weak at very short distances or large q^2, where $q = |\vec{q}|$ is the momentum transfer, and strong at long distances or small q^2. This implies that perturbation theory is acceptable only in the large q^2 regime. Unfortunately, hadrons such as nucleons or pions have low-q^2 exchanges that are very important in their internal structure. Therefore, perturbation theory is not applicable, and the only known rigorous non-perturbative method to solve QCD – namely lattice gauge theory – is not yet able to calculate NN properties.

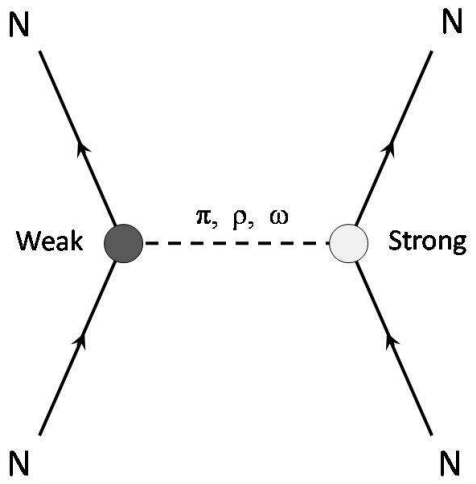

Figure 2.1: Diagram of the NN weak interaction by exchange of light pseudoscalar and vector mesons. The strong vertex is characterized by strong couplings (e.g. $g_\pi NN$), and the weak vertex is described by nucleon-meson weak couplings, which are listed in Table 2.1.

The simplest contribution to parity violation in the coupling between nucleons is a single W or Z exchange, which gives rise to an effective pseudoscalar potential between the nucleons. However, the effect of these effectively zero-range potentials is greatly suppressed because the NN strong interaction is repulsive at very short distances. The main contribution to the parity-violating interaction must therefore occur by the exchange of light pseudoscalar and vector mesons (Figure 2.1). The relative size of the parity-violating and parity-conserving nucleon-meson exchange potentials is roughly

$$\frac{V_{PV}}{V_0} \approx G_F {m_\pi}^2 \cong 2 \times 10^{-7} \tag{2.1}$$

where $m_\pi \approx 140$ MeV/c^2 is the charged pion mass.

However, this estimate ignores the complications of nucleon-meson dynamics (Figure 2.2). To proceed further with the meson exchange model, quark-level dynamics must be included.

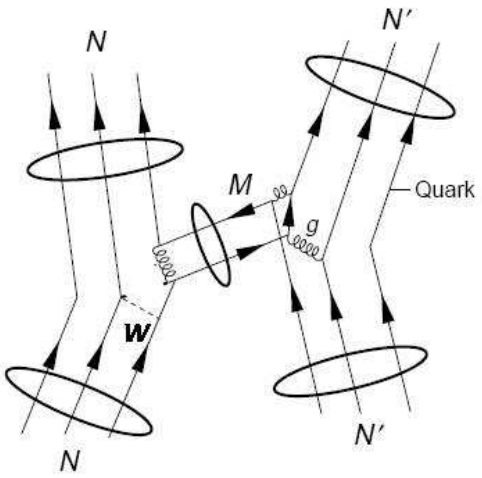

Figure 2.2: Diagram of a quark-level NN weak interaction by meson exchange.

2.1 Hadronic weak interaction Hamiltonian

For low-energy NN interactions (ignoring electromagnetic interactions), the hadronic weak interaction Hamiltonian can be constructed from the charged J_W and neutral J_Z weak current Lagrangian that involves only the light quarks (u, d, s):

$$\mathcal{L} = \frac{G_F}{\sqrt{2}}(J_W{}^{\dagger} J_W + J_Z{}^{\dagger} J_Z) \tag{2.2}$$

The charged current is determined by the GIM mechanism, where u and c quarks couple to linear combinations of d and s mass eigenstates via a unitary mixing matrix governed by the Cabibbo angle θ_C (see Equation 1.1). For light quarks, the charged weak current takes the form:

$$J_W = \bar{u}\gamma_\mu(1+\gamma_5)(\cos\theta_c\, d + \sin\theta_c\, s) \tag{2.3}$$

Under isospin rotation, the $\Delta S = 0$ portion of the charged current transforms like a vector ($|\Delta I| = 1$), while the $|\Delta S| = 1$ current transforms like an isospinor ($|\Delta I| = 1/2$). Additionally, the neutral weak current for quarks does not contain flavor-changing terms and takes the form:

$$J_Z = \bar{u}\gamma_\mu(1+\gamma_5)u - \bar{d}\gamma_\mu(1+\gamma_5)d - \bar{s}\gamma_\mu(1+\gamma_5)s - 4\sin^2\theta_W J_\mu^{EM} \tag{2.4}$$

with weak mixing (or Weinberg) angle θ_W and electromagnetic current $J_\mu{}^{EM}$. The neutral weak current has parts that transform as isoscalar ($|\Delta I| = 0$) and isovector ($|\Delta I| = 1$) under isospin rotation; the neutral current also conserves strangeness. The weak $\Delta S = 0$ current-current Lagrangian can now be written in terms of strong isospin dependence (superscripts denote isospin transition $|\Delta I|$):

$$\mathcal{L} = \frac{G_F}{\sqrt{2}}\left[\cos^2\theta_C\, J_W^0{}^{\dagger} J_W^0 + \sin^2\theta_C\, J_W^1{}^{\dagger} J_W^1 + J_Z^0{}^{\dagger} J_Z^0 + J_Z^1{}^{\dagger} J_Z^1 + J_Z^0{}^{\dagger} J_Z^1 + J_Z^1{}^{\dagger} J_Z^0\right] \tag{2.5}$$

The effective $\Delta S = 0$ hadronic weak interaction Hamiltonian is built from current-current terms that transform as follows:

$$J_W^{0\,\dagger} J_W^0 + J_W^0 J_W^{0\,\dagger} \qquad |\Delta I| = 0{,}2 \qquad (2.6)$$

$$J_W^{1\,\dagger} J_W^1 + J_W^1 J_W^{1\,\dagger} \qquad |\Delta I| = 1 \qquad (2.7)$$

$$(J_Z^0 + J_Z^1)^\dagger (J_Z^0 + J_Z^1) + (J_Z^0 + J_Z^1)(J_Z^0 + J_Z^1)^\dagger \qquad |\Delta I| = 0, 1, 2 \qquad (2.8)$$

The $|\Delta I| = 1$ component of the charged current is suppressed by a factor of $\sin^2 \theta_C \approx \frac{1}{25}$ as compared with the $|\Delta I| = 0{,}2$ component; this implies that the neutral current should dominate the $|\Delta I| = 1$ effective hadronic weak interaction Hamiltonian.

2.2 Meson-exchange model of the NN weak interaction

Because of the repulsive core of the strong interaction, the direct exchange of W and Z bosons between low-energy nucleons is suppressed. An improved representation of the NN weak interaction uses the meson exchange model that successfully describes the low-energy NN strong interaction. The NN interaction is described by the sum of meson exchange diagrams in which pseudoscalar and vector mesons (π, η, ρ, ω, σ …) couple strongly to the NN vertices. Similarly, the NN weak interaction can be modeled as an exchange of light mesons (π, ρ, ω) where the diagram has one weak interaction vertex and one strong vertex, as shown in Figure 2.1 [35].

Since the distance at which the repulsive core of the NN potential becomes dominant is $r \lesssim 0.4$ fm, mesons less massive than about 500 MeV dominate the exchange terms. The meson exchanges that contribute to the NN weak interaction include the pion $(J = 0, I = 1)$, the ρ-meson $(J = 1, I = 1)$, and the ω-meson $(J = 1, I = 0)$. Since the exchange of a neutral spinless boson between on-shell nucleons is forbidden by CP invariance (Barton's Theorem [36]), π^o , η, η', σ, and δ^o exchange are excluded to the extent that CP conservation holds.

Table 2.1: Transition properties for exchange mesons in the meson-exchange model of NN weak interaction.

Transition	ΔI	n-n	n-p	p-p	Exchanged Meson	Nucleon-Meson Weak Coupling
${}^3S_1 \leftrightarrow {}^1P_1$	0		x		ρ, ω^o	h_ρ^o, h_ω^o
${}^1S_0 \leftrightarrow {}^3P_0$	0	x	x	x	ρ, ω^o	h_ρ^o, h_ω^o
	1	x		x	ρ, ω^o	h_ρ^1, h_ω^1
	2	x	x	x	ρ	h_ρ^2
${}^3S_1 \leftrightarrow {}^3P_1$	1		x		$\pi^\pm$, ρ, ω^o	$f_\pi, h_\rho^1, h_\omega^1$

Essentially all of the weak interaction physics is contained within the weak vertex and is expressed in the values of the parity-violating nucleon-meson weak couplings. The NNM weak matrix elements $\langle M\,N|\mathcal{H}_{wk}|N\rangle$ for both the charged and neutral current contributions were calculated by DDH in 1980 [19].

It is important to note that since the π-meson exchange is purely isovector and the contribution from the charged current is proportional to $\sin^2\theta_c$, the charged current is strongly suppressed. Therefore, the neutral current contribution dominates the π-meson amplitude, and its coupling strength should be a direct measure of the neutral current contribution to the NN weak interaction.

Thus, the leading mesons exchanges are the $\pi^\pm$ with $\Delta I = 1$ transitions only, the ρ with $\Delta I = 0,1,2$ transitions, and the ω with $\Delta I = 0,1$ transitions. Table 2.1 (adapted from [14]) lists the six non-negligible nucleon-meson weak couplings and their associated transition properties.

Table 2.2: Calculated strengths for the nucleon-meson weak couplings. Amplitudes are given in sum-rule units, $g_\pi = 3.8 \times 10^{-8}$.

Nucleon-Meson Weak Coupling	DDH Reasonable Range	DDH "Best Value"
f_π	$0 \rightarrow 30$	12
h_ρ^o	$30 \rightarrow -81$	–30
h_ρ^1	$-1 \rightarrow 0$	–0.5
h_ρ^2	$-20 \rightarrow -29$	–25
h_ω^o	$15 \rightarrow -27$	–5
h_ω^1	$-5 \rightarrow -2$	–3

A number of uncertainties are associated with the DDH calculations, including those arising from uncertainties in the current-masses of the *u* and *d* quarks, the use of a relativistic vs. nonrelativistic quark model, and the effects of SU(6) symmetry breaking on sum-rule contributions and emission amplitudes. These uncertainties led DDH to present the nucleon-meson weak coupling predictions as a broad range of "acceptable values." Additionally, a "best value" is presented that represents the theorists' "educated guess" of the true values and are presented in Table 2.2.

2.3 Effective field theory and chiral perturbation approaches

Recently, a systematic analysis of the NN weak interaction using an effective field theory (EFT) approach and chiral perturbation theory has appeared [6, 16-18]. This new approach has the advantage that it is model-independent. It is by construction the most general formulation consistent with the symmetries of QCD, and can be used as a basis for calculation in low-energy processes using the ratio of the typical momentum transfer

relevant for a parity-violating hadronic process to the hadronic scale $\Lambda_{HAD} \approx 1$ GeV as an expansion parameter.

Six constants appear in this "hybrid" EFT approach for low-energy NN weak processes (< 40 MeV) [16], which take the wavefunctions from strong interaction phenomenology and the NN weak interaction operator structure from EFT. Five of these constants are EFT versions of the five independent parity-odd S-P NN elastic scattering amplitudes first emphasized by Danilov [37]: $m_N\lambda_s{}^{pp}$, $m_N\lambda_s{}^{np}$, and $m_N\lambda_s{}^{nn}$ for the three independent ${}^1S_0 \rightarrow {}^3P_0$ transitions (*pp*, *np*, *nn*, $\Delta I = 0,1,2$); $m_N\lambda_t$ for the ${}^3S_1 \rightarrow {}^1P_1$ transition (*np*, $\Delta I = 0$); and $m_N\rho_t$ for the ${}^3S_1 \rightarrow {}^3P_1$ transition (*np*, $\Delta I = 1$). A sixth parameter C_6 describes long-range weak pion exchange and is related to the isovector nucleon-meson weak coupling f_π.

In parallel with this EFT development, preparations have been made to calculate the NN weak couplings using lattice gauge theory in the partially-quenched approximation [38]. Taken together, these theoretical efforts set the stage for eventual quantitative predictions of the NN weak interaction directly from the Standard Model and QCD.

Listed in Table 2.3 (adapted from [16]) are observables of parity-violating NN few body systems in terms of the EFT approach for experiments that have been performed or are practical. These observables need recalculating in the EFT with pions to determine their dependence on the long-range pion coupling parameter C_6, so question marks have been inserted into the corresponding entries. This makes it difficult to evaluate the scientific impact of a particular measurement within the EFT approach, and at the moment, only one constant $m_N\lambda_s{}^{pp} \sim 2 \times 10^{-7}$ has been experimentally determined. Furthermore, the parity-violating neutron spin rotation in ($\vec{n}$, ^{4}He) has yet to be calculated in the new hybrid EFT framework, so the question of whether or not the internal momenta of the nucleons in ^{4}He are too large for the *S*-*P* dominance assumed in the 6-parameter EFT analysis has yet to be addressed.

	C_6	$m_N\lambda_s^{pp}$	$m_N\lambda_s^{np}$	$m_N\lambda_s^{nn}$	$m_N\lambda_t$	$m_N\rho_t$	measurement
$A_\gamma(np \to d\gamma)$ (10^{-7}) [39-41]	-0.27					-0.09	-0.6 ± 2.1
$\varphi_{PV}(n,p)$ (10^{-7}) [42, 43]	0.29		2.50		-0.57	1.41	
$A_\gamma(nd \to t\gamma)$ (10^{-6}) [44]	?		0.51	0.59	1.18	1.42	4.2 ± 3.8
$\varphi_{PV}(n,\ ^4\mathrm{He})$ (10^{-7}) [45]	?		0.6	1.2	1.34	-2.68	8 ± 14
$\Delta\sigma/\sigma\,(p,p)$ (10^{-7})		-0.45					-0.93 ± 0.21
$\Delta\sigma/\sigma\,(p,\ ^4\mathrm{He})$ (10^{-7})	?	-0.48	-0.24		-0.54	-1.07	-3.3 ± 0.9
$P_\gamma(np \to d\gamma)$ (10^{-7})			-0.16		0.67		1.8 ± 1.8

Table 2.3: Contributions from terms in the EFT approach to parity-violating NN observables in few-body systems that have already been measured or are experimentally practical. References for the neutron calculations are given in the row headings.

2.4 Experimental Studies of the NN weak interaction

The majority of NN weak interaction experiments involve the detection of pseudoscalar observables that are odd under spatial inversion. Observables related to $\vec{\sigma} \cdot \vec{p}$ are parity violating, since momentum changes sign under parity, but spin does not. One example is the circular polarization of gamma rays emitted by an unpolarized, parity-mixed nuclear state $P_\gamma = \langle \vec{\sigma}_\gamma \cdot \hat{p}_\gamma \rangle$. Unfortunately, circular polarization experiments are restricted in precision by the low efficiency of the circular polarization analyzer for few MeV gammas (typically 4%). A related parity-violating observable is the asymmetry of photons emitted with respect to the polarization direction of the parent nuclei A_γ (e.g. from deuterium polarized in the $\vec{n} + p$ reaction). This observable is related to $\langle \vec{J} \cdot \vec{p}_\gamma \rangle$, where $\vec{J}$ is the nuclear polarization. If the polarization of the capture state can be made high, a practical experiment is possible.

Another common parity-violating observable is the longitudinal analyzing power A_L of reactions initiated by nucleons that are spin-polarized parallel or anti-parallel their momentum vectors. The analyzing power is proportional to the asymmetry of cross sections for incident nucleons in forward and backward helicity states. This observable is proportional to both a cross-section difference and (by the optical theorem) the helicity dependence of the imaginary part of the forward scattering amplitude, it is typically large either on resonance or at higher energies. For low-energy NN scattering, it can be shown that the magnitude of A_L vanishes as incident nucleon energy goes to zero [46].

Whereas the longitudinal analyzing power A_L depends on the imaginary part of the forward scattering amplitude, the parity-violating neutron spin rotation φ_{PV} depends on the real part of the forward scattering amplitude. This effect is analogous to the optical rotation of polarized photons traveling through a chiral medium, where the "handedness" of the medium for a propagating neutron is the weak interaction. Since the parity-violating spin-rotation angle is proportional to the real part of the forward scattering amplitude, which is proportional to the neutron wavenumber *k*, the parity-violating spin

rotation per unit length does not vanish as $E \to 0$ (see Section 3.2). Parity-violating neutron spin-rotation measurements with cold neutrons have been performed in isotopes of tin [47, 48], lead [4] and lanthanum [5], and searched for in cesium, rubidium, and bromine [49].

In the low-energy NN system, the size of parity-violating observables is expected to be extremely small: of order $4\pi G_F m_\pi^2 / g_{\pi NN}^2 \approx 10^{-7}$, as given by the ratio of weak to strong amplitudes. Measurements of such small signals require experiments with sufficient sensitivity to extract useful information on nucleon-meson weak couplings as well as rigorous constraints on the experimental setup that are technically challenging.

2.4.1 Intermediate A nuclei

In nuclear systems with $A > 5$, parity-mixed doublet states are studied by detecting pseudoscalar observables, such as A_L in ^{14}N, P_γ in ^{18}F, and A_γ in ^{19}F. The resulting signal from the parity mixing of two well-known states of identical spins with small energy separation and opposite parity is enhanced by the small difference in energies between the two states. Further enhancement occurs for doublets with very different decay amplitudes, which often happens since the parent states have opposite parity and therefore the electromagnetic part of the transition matrix element is different for the two states. These enhancements can lead to signals of order 10^{-4} to 10^{-5}, which is a distinct experimental advantage.

Measurements of the circular polarization of the photon decay of parity-mixed levels in ^{18}F are consistent [27-29, 50, 51]:

$$\left|P_\gamma(1081)\right| = \begin{cases} (-7 \pm 20) \times 10^{-4} & Caltech\ /\ Seattle \\ (3 \pm 6) \times 10^{-4} & University\ of\ Florence \\ (-10 \pm 18) \times 10^{-4} & Mainz \\ (2 \pm 6) \times 10^{-4} & Queen's\ University \\ (-4 \pm 30) \times 10^{-4} & University\ of\ Florence \end{cases}$$

Measurements of the circular polarization of the photon decay of parity-mixed levels in ^{21}Ne are consistent [52, 53]:

$$P_\gamma = \begin{cases} (24 \pm 24) \times 10^{-4} & Seattle\ Chalk/River \\ (3 \pm 16) \times 10^{-4} & Chalk\ River/Seattle \end{cases}$$

Measurements of the asymmetry in the decay of the first excited state of ^{19}F are consistent [31, 54-56]:

$$A_\gamma = \begin{cases} (-8.5 \pm 2.6) \times 10^{-5} & Seattle \\ (-6.8 \pm 1.8) \times 10^{-5} & Mainz \end{cases}$$

The measured effects in ^{18}F, ^{21}Ne and ^{19}F are two to three orders of magnitude larger than one would expect, because these systems have an accidental near-degeneracy of nearby levels with identical spin but opposite parity, thus enhancing the signal.

The parity-violating NN weak interaction has also been studied by measuring the rates of parity-violating processes. Measurements of parity-forbidden alpha decays have been done in ^{16}O [57] and ^{20}Ne [58]. However, uncertainties associated with the contribution of more than one interfering state of the same spin and opposite parity complicate the interpretation of the results, and these results have yet to be used in theoretical analyses of constraints on the NN weak interaction.

2.4.2 Heavy nuclei

In medium and heavy nuclei, the parity violation in low-energy neutron scattering is often greatly enhanced. The helicity dependence of the neutron forward scattering amplitude with complex nuclei at weak *p*-wave resonances can be enhanced by factors as large as 10^6. This enhancement comes from a combination of the large density of compound nuclear resonances and by the very large ratio of the *s*-wave to *p*-wave neutron scattering amplitudes.

While parity violation experiments in few body systems and light nuclei require detailed wave functions of the nuclear states for analysis, a different analysis approach is required for medium and heavy nuclei. Compound nuclei display stochastic properties that allow for statistical analysis methods, which do not require detailed nuclear structure to obtain information on the parity-violating NN weak interaction [59, 60]. However, this analysis requires a large number of observations of parity-odd observables for input to justify a statistical analysis.

In addition to nuclear processes, measurements of atomic parity-violating observables probe the hadronic weak interaction. The anapole moment arises from the electron-nucleus interaction in which the exchange photon is absorbed by parity-violating components of the nuclear wave function. Substantial improvements to atomic parity violation measurements in cesium have recently lead to the first definitive measurement of the anapole moment [13], and other measurements are in progress for other atoms.

2.4.3 Few body nuclei

Only a few measurements of parity violation in few body nuclei have been performed with high enough precision to see a nonzero effect. For experiments that probe the *pp* system, only the ${}^1S_0 \leftrightarrow {}^3P_0$ transition is involved. In addition, since Barton's theorem eliminates weak π^o exchange, *pp* scattering is not sensitive to weak pion exchange at all. These experiments are then sensitive to the nucleon-meson weak couplings $h_\rho^o, h_\rho^1, h_\rho^2, h_\omega^o, h_\omega^1$, and the EFT coefficients $m_N {\lambda_s}^{pp}$, $m_N {\lambda_s}^{np}$, and $m_N {\lambda_s}^{nn}$. Measurements of the scattering asymmetry of longitudinally polarized protons from hydrogen [61, 62] at two different energies are consistent:

$$A_z(\vec{p}_{45\text{ MeV}}, p) = -(1.57 \pm 0.23) \times 10^{-7}$$
$$A_z(\vec{p}_{13.6\text{MeV}}, p) = -(0.93 \pm 0.20 \pm 0.05) \times 10^{-7}$$

For experiments involving *np* and *pp* interactions, all transitions are allowed. Therefore, measurements in these systems provide information on linear combinations of

all nucleon-meson weak couplings and all EFT coefficients. The measurement of the scattering asymmetry of longitudinally polarized protons from helium have resolved a nonzero effect [26, 63]:

$$A_z(\vec{p}_{46\mathrm{MeV}},\ ^4\mathrm{He}) = -(3.34 \pm 0.93) \times 10^{-7}$$

2.5 Constraints of nucleon-meson couplings

At the present level of experimental accuracy, the isotensor coupling contribution is significant in only the *pp* system, and even there it is small compared to the isoscalar contribution. Thus, it is reasonable to present the results with only the dominant isovector contribution from the f_π coupling and an effective isoscalar coupling (h_ρ^0 + 0.6 h_ω^0). A summary of results from the previously discussed experiments is given in Figure 2.3. The reasonable range values are indicated, and the result of a least squares fit to the data (excluding the ^{133}Cs and revised ^{21}Ne data) for both the isoscalar and isovector couplings is shown.

Theoretical uncertainties in extracting the nucleon-meson weak couplings from systems more complicated than the bare NN system may be significant, but are not included in the error bands presented. For example, in the study of parity doublet decays in ^{21}Ne for which a beta-decay calibration of the matrix elements is not possible, substantial changes to the results can be made with reasonable changes in the nuclear structure calculations [64]. A revised analysis for ^{21}Ne is presented, again showing only the experimental errors.

Also presented is the range of the couplings derived from the analysis by Flambaum and Murray [32] of the cesium anapole moment measurement. Their calculations are consistent with the ^{18}F results only for large, negative values for the isoscalar couplings. The error band includes only the experimental error. Using DDH best values for all other couplings, they obtained $f_\pi = \big(9.5 \pm 2.1(\mathrm{exp}) \pm 3.5(\mathrm{theo})\big) \times 10^{-7}$. With the inclusion of the theoretical error, this result becomes consistent with the DDH prediction [32]

As seen in Figure 2.3, there is currently no consistent set of coupling values that fit the experimental data. The ^{18}F measurement provides the most reliable constraint on f_π, restricting it to the small range of $|f_\pi| \leq 1.3 \times 10^{-7}$. Both the DDH "best values" and the "best fit" are outside of this range. In addition, theoretical calculations of the couplings based on different models and assumptions do not agree.

There is no clear determination of the nucleon-meson weak couplings. Improved experiments in the bare NN systems would greatly improve this situation by introducing results with a minimum of theoretical uncertainties. The measurement of the parity-violating neutron spin rotation in light nuclei would provide such an opportunity.

Spin rotation experiments in heavy nuclei [4, 5] have shown the ability of neutron polarimeters to measure small spin rotation observables. A sensitive measurement of the parity-violating neutron spin rotation in a liquid parahydrogen target $\varphi_{PV}(\vec{n}, p)$ would provide a direct determination of f_π. However, the experimental drawbacks of working with a potentially explosive target, maintaining a 22K liquid target reservoir, and reducing possibly large systematic uncertainties due to scattering make this experiment technically challenging.

The parity-violating spin rotation in a liquid helium target $\varphi_{PV}(\vec{n}, {}^4He)$ is experimentally more feasible. This system is sensitive to both isovector and isoscalar couplings and is the isospin analog of the $\vec{p} + \alpha$ system studied by Lang *et al*. [26, 63]. The experimental difficulties are greatly reduced for a helium target system since helium gas is not explosive and does not impose additional safety hazards, a 4K cryogenic reservoir is easier to maintain, and scattering effects are significantly less. In addition, the design, construction and operational experience gained during an experiment with a liquid helium target will be directly applicable to future experiments with a liquid hydrogen target and perhaps a liquid deuterium target.

Although interpreting the results in the $\vec{n} + {}^4He$ system requires some nuclear structure calculations, the neutron spin-rotation measurement in liquid helium is of considerable theoretical interest. This $A = 5$ system can be calculated with less uncertainty than heavier nuclear systems. Currently, the controversial ^{21}Ne experiment provides the only measurement for the neutron-nucleus part of the weak interaction. A definitive neutron spin-rotation measurement in the $\vec{n} + {}^4He$ system would provide direct information to determine the strength of the parity-violating neutron-nucleus force [21, 65]. In addition, this measurement would provide the first opportunity to directly compare two isospin mirror systems: $\vec{n} + {}^4He$ and $\vec{p} + \alpha$. Combining the results from the $A_L(\vec{p}, \alpha)$ and $\varphi_{PV}(\vec{n}, {}^4He)$ experiments will provide a new way to constrain the isovector f_π and isoscalars h_ρ^0 and h_ω^0.

Within the isoscalar/isovector subspace of nucleon-meson weak couplings, the parity-violating neutron spin rotation in $\vec{n} + {}^4He$ constrains a linear combination of couplings that is approximately orthogonal to previously measured parity violation in the isospin-conjugate $\vec{p} + \alpha$ system [26] and in ^{133}Cs [13]. For ^{4}He, the calculated parity-violating neutron spin rotation is $\varphi_{PV} = (-0.1 \pm 1.5) \times 10^{-6}$ rad/m using the DDH "best values" [45]. A measurement at 3×10^{-7} rad/m accuracy would make a narrow cut in the expected range of parameter space of nucleon-meson weak couplings.

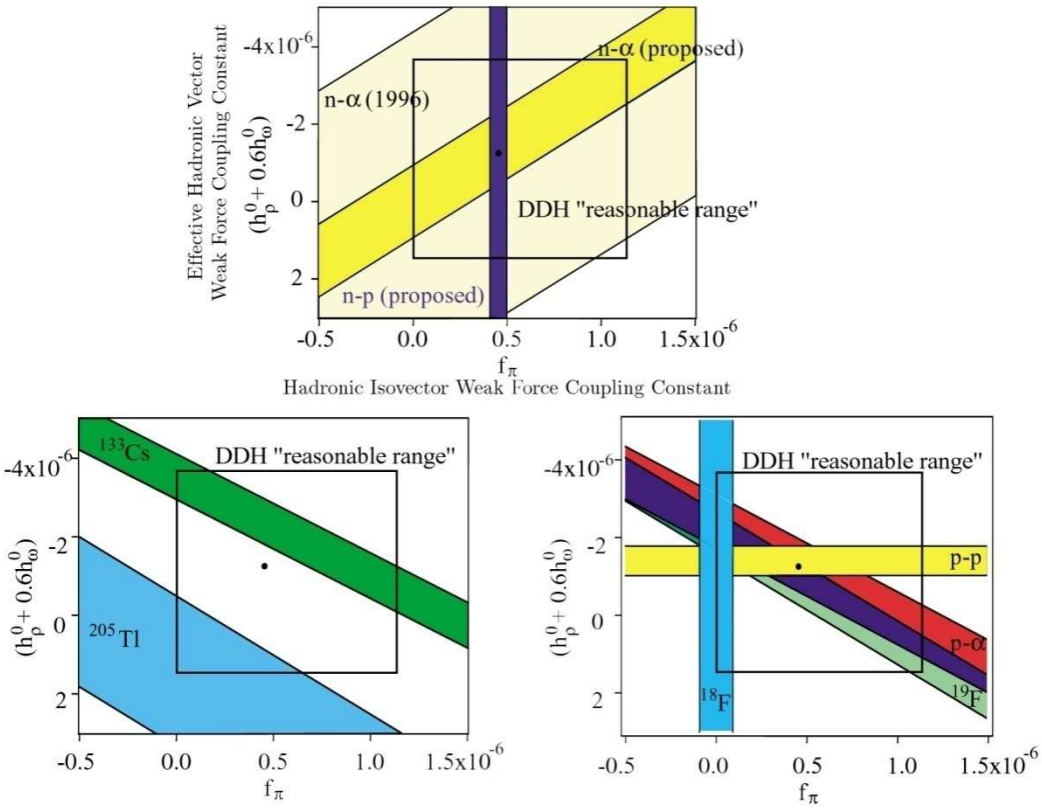

Figure 2.3: Plot of experimental constraints on the isovector and isoscalar nucleon-meson weak coupling constants in the DDH model. Note that the constraint from the $\vec{n} + {}^4He$ spin rotation is orthogonal to measurements of both the ^{133}Cs anapole moment and the $\vec{p} + \alpha$ transmission asymmetry.

3 Neutron Optics and Spin Rotation

A transverse rotation of the neutron spin vector about its momentum manifestly violates parity [66] and can be viewed from a neutron optical viewpoint as due to a helicity-dependent neutron refractive index. In analogy to light, the scattering of low-energy neutrons can be treated in a manner similar to light wave scattering. Below thermal energies ($E \simeq 25$ meV), neutrons have a de Broglie wavelength $\lambda \geq 1$ Å, which is larger than the interatomic spacings. In nonrelativistic scattering theory, a low-energy neutron wavefunction outside of a scattering potential is the sum of an incident plane wave plus an outgoing scattered wave,

$$\psi = e^{i\vec{k}\cdot\vec{r}} + \frac{e^{ikr}}{r} f(\theta) \tag{3.1}$$

with wavenumber $k = 2\pi/\lambda$, de Broglie wavelength $\lambda = \hbar^2/2mE$ for a free particle of energy E, and scattering amplitude $f(\theta)$. For a neutron inside a square well potential of depth V_o, the wavenumber is given by

$$k^2 = {k_i}^2 = \frac{2m}{\hbar^2}[E - V] \tag{3.2}$$

For an effective square well potential for the strong interaction of depth $V \approx 40$ MeV and radius $R = R_o A^{1/3}$, where $R_o = 1.2$ fm and A is the nuclear mass ($R \sim 2$ fm for helium) [67], $kr \ll 1$ and therefore the scattering from this effective potential is mostly *s*-wave and isotropic, and thus independent of incident angle:

$$f(\theta) = f(0) = -a \tag{3.3}$$

where a is the free scattering length.

3.1 Refraction of a neutron wave

Inside a medium, the neutron wavefunction ψ_n is described by the superposition of an incident wave and coherently scattered waves, and it must satisfy the one-body Schrödinger equation:

$$(\nabla^2 + k^2)\langle\psi_n\rangle = 0 \tag{3.4}$$

An effective complex refractive index n for the neutron wavefunction is given by the ratio of the neutron wavenumbers inside and outside of the effective potential:

$$n^2 = \frac{{k_o}^2}{{k_i}^2} = 1 - \frac{V}{E} \tag{3.5}$$

Therefore, the Schrödinger equation for the neutron wavefunction inside the effective potential becomes

$$\left(\nabla^2 + {k_o}^2 n^2\right)\langle\psi_n\rangle = 0 \tag{3.6}$$

The non-scattered (plane wave) component of the neutron wavefunction is

$$\langle\psi_n\rangle \simeq e^{i\vec{k}\cdot\vec{r}} \cong e^{in\vec{k}_o\cdot\vec{z}} = e^{-\mathrm{Im}(n)\vec{k}_o\cdot\vec{z}} e^{i\,\mathrm{Re}(n)\vec{k}_o\cdot\vec{z}} \tag{3.7}$$

As the neutron passes through a medium, the real component of the refractive index contributes an extra phase to the wave: $\phi = \mathrm{Re}(n)k_o\hat{z}$ where $\vec{k}_o = k_o\hat{z}$.

The discontinuous potential of atomic media can be approximated by a uniform potential [68]:

$$V \cong \bar{V} = \left(\frac{2\pi\rho\hbar^2}{m}\right)a \tag{3.8}$$

where ρ is the atomic number density, and a is the scattering length from Equation 3.3. For non-absorbing media, the refractive index is

$$n = \sqrt{1 - \frac{4\pi\rho a}{k^2}} \simeq 1 - \frac{2\pi\rho a}{k^2} = 1 + \frac{2\pi\rho}{k^2} f(0) \tag{3.9}$$

For 5 Å neutrons propagating through liquid helium with $\rho = 0.19 \times 10^{23}$ cm^{-3} and scattering length $a = 3$ fm, the refractive index is $1 - \mathrm{Re}(n) = 2 \times 10^{-6}$.

3.2 Spin rotation observable

For low-energy neutrons, the general form for the coherent forward scattering amplitude that obeys isospin symmetry is

$$f(0) = A + B\vec{\sigma}_n \cdot \vec{S}_N + C\vec{\sigma}_n \cdot \vec{k}_n + D\vec{S}_N \cdot \vec{k}_n + E\vec{\sigma}_n \cdot \left(\vec{k}_n \times \vec{S}_N\right) \tag{3.10}$$

with incident neutron spin $\vec{\sigma}_n$ and wavevector $\vec{k}_n$, and target nuclei spin $\vec{S}_N$.

For an unpolarized target nuclei $\langle \vec{S}_N \rangle = 0$, the coherent forward scattering amplitude becomes

$$f(0) = A + C\vec{\sigma}_n \cdot \vec{k}_n \tag{3.11}$$

In terms of parity-conserving and parity-violating components,

$$f(0) = f_{PC} + f_{PV}\left(\vec{\sigma}_n \cdot \vec{k}_n\right) \tag{3.12}$$

The parity-violating term is proportional to the weak interaction matrix element [45]

$$f_{PV} = -\frac{m}{2\pi} \mathrm{Re}\left\langle {}^4\mathrm{He}, \psi_i \middle| \mathcal{H}_{wk} \middle| {}^4\mathrm{He}, \psi_o \right\rangle \tag{3.13}$$

Because the weak interaction violates parity, the forward scattering amplitudes are different for the two helicity states, and so the refractive indices are different for the two helicity states. As a neutron passes through a medium, the two helicity states accumulate

different phases. In terms of parity-conserving and parity-violating terms, the accumulated phase is

$$\phi = kz\left[1 + \frac{2\pi\rho}{k^2}\left(f_{PC} + f_{PV}\left(\vec{\sigma}\cdot\vec{k}\right)\right)\right] \tag{3.14}$$

$$\phi_{\pm} = \phi_{PC} \pm \phi_{PV} \tag{3.15}$$

where the parity-conserving and parity-violating terms are given by

$$\phi_{PC} = kz\left(1 + \frac{2\pi\rho}{k^2} f_{PC}\right) \tag{3.16}$$

$$\phi_{PV} = 2\pi\rho z f_{PV} \tag{3.17}$$

Since the parity-violating part of the forward scattering amplitude is proportional to *k*, the accumulated phase per unit length is constant in the low-energy neutron limit [45].

A transversely polarized neutron is a linear combination of helicity states. For a neutron that is vertically polarized in the "up" state,

$$|\uparrow\rangle_i = \frac{1}{\sqrt{2}}\left(|+\rangle + |-\rangle\right) \tag{3.18}$$

As the neutron passes through a medium, the accumulated phase difference changes the polarization state:

$$|\uparrow\rangle_o = \frac{1}{\sqrt{2}}\left(e^{i\phi_+}|+\rangle + e^{i\phi_-}|-\rangle\right) \tag{3.19}$$

In terms of parity-conserving and parity-violating components of the phase, the polarization state is

$$|\uparrow\rangle_o = \frac{1}{\sqrt{2}}\left(e^{\mathrm{i}(\phi_{\mathrm{PC}}+\phi_{\mathrm{PV}})}|+\rangle + e^{\mathrm{i}(\phi_{\mathrm{PC}}-\phi_{\mathrm{PV}})}|-\rangle\right) \tag{3.20}$$

The parity-conserving phase component ϕ_{PC} gives an overall phase factor that depends on the parity-conserving scattering amplitude. The parity-violating phase component ϕ_{PV} generates a rotation about the neutron momentum vector. Therefore, the parity-violating spin-rotation angle is due to the accumulated phase difference between helicity states:

$$\varphi_{PV} = \phi_+ - \phi_- = 2\phi_{PV} = 4\pi\rho z f_{PV} \tag{3.21}$$

It should be noted that this parity-violating spin rotation is due to the weak interaction part of the real component of the forward scattering amplitude. In contrast, the imaginary component of the forward scattering amplitude due to the weak interaction causes a difference in scattering cross sections due to helicity differences. This causes a non-zero longitudinal analyzing power A_L and longitudinal transmission asymmetry. However, since these effects are proportional to momentum, they are typically small for low-energy neutrons away from resonances $\left(\frac{\delta\sigma}{\sigma} \approx 10^{-10}\right)$ and can be neglected.

3.3 Theoretical predictions for spin rotation in liquid helium

Avishai [69] estimated the size of the parity-violating neutron spin-rotation observable in liquid helium, which is based on a non-relativistic, parity-violating Hamiltonian and a simplified dependence of the forward scattering amplitude on the strength of the weak interaction coupling. Avishai calculated the rotation in liquid helium as

$$\varphi_{PV}\left(\vec{n},\ ^4\mathrm{He}\right) \approx 7.3 \times 10^{-7}\ \mathrm{rad/m} \tag{3.22}$$

Dmitriev [45] expressed the spin-rotation angle of neutrons propagating through liquid helium in terms of the nucleon-meson weak couplings:

$$\varphi_{PV}\left(\vec{n},\ ^4\mathrm{He}\right) = -\begin{pmatrix} 0.97 f_\pi + 0.22 h_\omega^0 - 0.22 h_\omega^1 \\ +0.32 h_\rho^0 - 0.11 h_\rho^1 - 0.02 h'^1_\rho \end{pmatrix} \mathrm{rad/m} \tag{3.23}$$

For "reasonable parameters" of the nucleon-meson weak couplings, Dmitriev calculated the neutron spin-rotation angle in helium: $\varphi_{PV}(\vec{n},\ ^4\mathrm{He}) = -(0.1 \pm 1.5) \times 10^{-6}\mathrm{rad/m}$. Using the best fit data from the existing nucleon parity violation data into Equation 3.23, we predict a spin-rotation angle

$$\varphi_{PV}(\vec{n},\ ^4\mathrm{He}) = -0.7 \times 10^{-7}\ \mathrm{rad/m} \tag{3.24}$$

The contribution from neutron–electron weak interaction is calculated to be $6 \times 10^{-8}\ \mathrm{rad/m}$. It is suppressed relative to the quark-quark weak interaction because the quark-electron weak coupling of interest is proportional to $1 - 4\sin^2\theta_W \sim 0.1$ (see Equation 2.4).

4 Experiment Overview with Design Constraints

Measuring a spin-rotation angle of order 10^{-7} rad/m requires an experimental sensitivity of 5×10^{-8} rad/m. This would constitute the smallest neutron spin-rotation angle ever measured. The challenge of the neutron spin-rotation experiment is designing the apparatus to distinguish the small parity-violating rotations from those rotations that arise from residual magnetic fields.

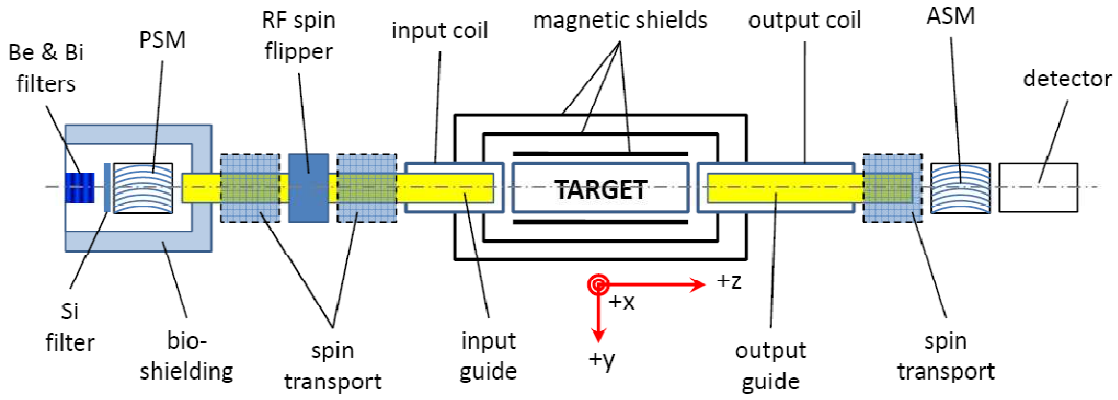

Figure 4.1: Diagram of the neutron polarimeter on the NG6 beam at the NCNR (top view). The neutron beam enters from the left and is transversely polarized by a supermirror. Neutrons then pass through the target and into a supermirror analyzer. A neutron detector measures the intensity of the transmitted beam.

In order to measure the small parity-violating spin rotation, a neutron polarimeter is used to measure the transverse horizontal ($\hat{y}$) polarization component of a neutron beam that is initially polarized in the vertical spin "up" direction ($+\hat{x}$). As shown in Figure 4.1, this polarimeter consists of a neutron supermirror polarizer, an adiabatic RF spin-flipper, a nonmagnetic neutron guide, spin transport, a magnetically-shielded zero-field target

region, an adiabatic spin rotator, a neutron supermirror polarization analyzer, and a current-mode ion chamber.

The measurement technique focuses on the orientation of the neutron polarization direction, which emerges along $+\hat{x}$-direction from the polarizer. In the absence of spin rotation, this orientation remains unchanged during passage through the spin transport and into the target region, but upon exiting the target region is rotated adiabatically into the polarization analyzer by $\pm\pi/2$ radians (see Figure 4.2) using the field in the output coil, which is constructed to possess a $\pm\pi/2$ twist. The beam polarization is now along the $\pm\hat{y}$- direction, which is perpendicular to the analyzing polarizer axis (along the $+\hat{x}$-direction). For both of these cases, the transmitted intensity through the analyzer is the same, and the count rate difference in the beam monitor is zero.

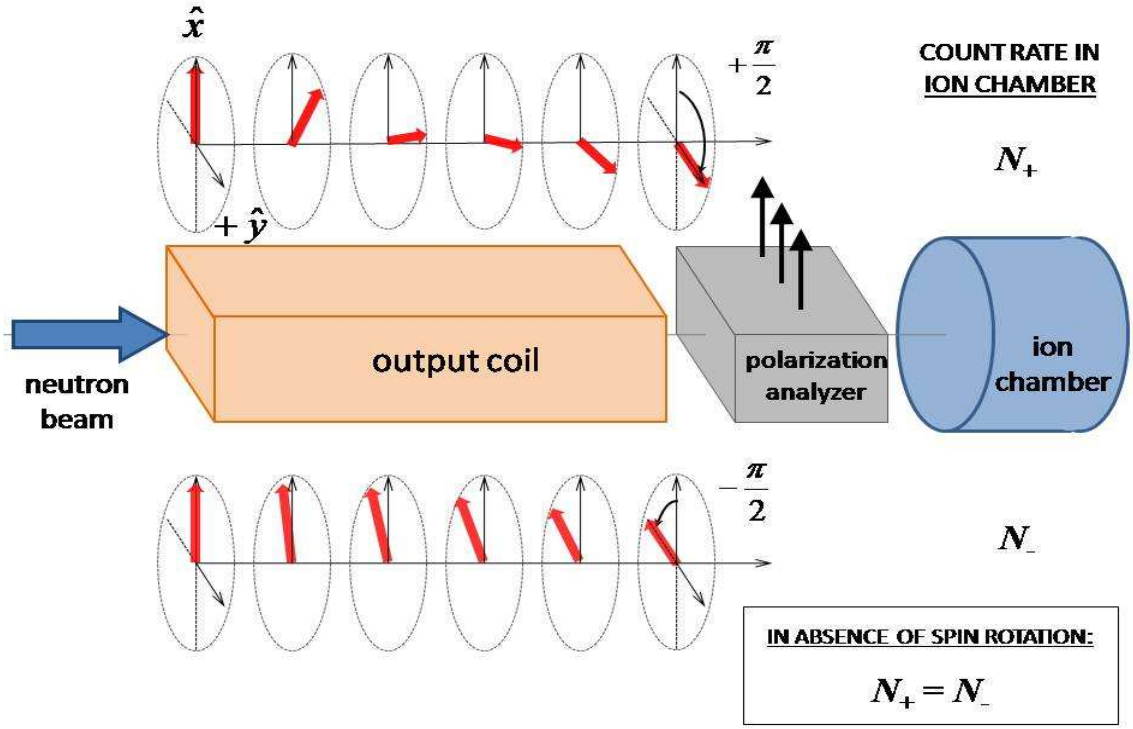

Figure 4.2: Diagram of the adiabatic rotation of neutron polarization by the output coil for the case of no spin rotation.

However, if the neutron polarization transversely rotates during its passage through the target region, there will be a component of the neutron polarization upon reaching the analyzer that is along the $\hat{x}$–direction, and this component flips between the $+\hat{x}$ and $-\hat{x}$ directions as the sense of the twist in the magnetic field of the adiabatic transport system is flipped between the $(+y \rightarrow +x)$ and the $(+y \rightarrow -x)$ states (see Figure 4.3). The transmission of neutrons that are polarized parallel and antiparallel to the axis of the analyzer is different, and so there is an asymmetry in the count rates given by

$$\frac{N_+ - N_-}{N_+ + N_-} = PA \sin \varphi \tag{4.1}$$

where P is the neutron polarization from the polarizer, A is the analyzing power of the polarization analyzer, and φ is the neutron spin-rotation angle. The product PA can be easily measured by applying an external magnetic field to set φ to a known angle. Furthermore, by flipping between analyzer states at a known frequency, the noise in the measurement of the angle is confined to a narrow frequency range about this frequency, and is therefore greatly suppressed.

However, longitudinal magnetic fields can also generate spin rotations. Magnetic shielding reduces the longitudinal field in the target region to less than 100 μG, but even this small field will generate a 2.5 mrad spin rotation for a 5 Å neutron. In contrast, the parity-violating rotation for a 40 cm liquid helium target is expected to be 0.3 μrad, which is ~8000 times smaller than the background rotation. Since the handedness of the parity-violating spin rotation through the target does not change if the neutron polarization is flipped, an asymmetry measurement between opposite neutron polarization states will not work to extract the small parity-violating signal from the larger parity-conserving background.

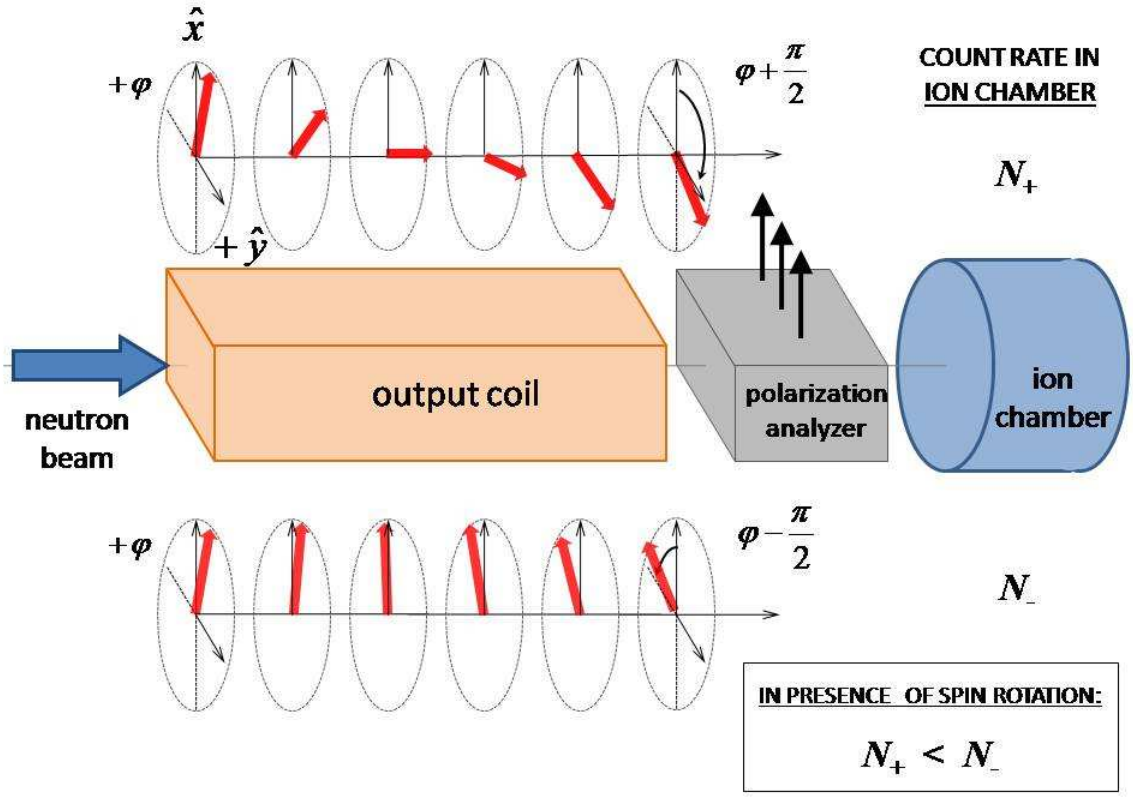

Figure 4.3: Diagram of the adiabatic rotation of neutrons by the output coil that have undergone spin rotation.

In order to separate the parity-violating component of the signal, two target positions are used, one upstream and one downstream of a central solenoid called the "pi-coil". The spin rotation due to residual magnetic fields will be the same for targets placed in either position if the target is nonmagnetic and the trajectories and energies of those neutrons that enter the analyzer and beam detector are unchanged when the target position changes. Diamagnetic effects in the target coupled with longitudinal field gradients and neutron scattering can spoil this equality.

The pi-coil generates an internal field that rotates the neutron polarization direction by π radians about the $+\hat{x}$–axis for neutrons of the correct energy, and thus reverses the component of the neutron spin for rotations that occur in the upstream target region. With the pi-coil on, the parity-violating contribution to the neutron spin rotation for the two target positions changes sign, and so the difference in the total spin rotation between target states is $2\varphi_{PV}$. However, care must be taken that turning on the pi-coil does not introduce a new contribution to the residual magnetic field.

Segmentation of the ion chamber along the beam axis allows the spin-rotation angle to be measured as a function of neutron energy. In the low-energy limit, the parity-violating neutron spin rotation is independent of neutron energy [45], while the amount of spin rotation due to magnetic fields is proportional to the time spent in the field, and hence neutron energy. The neutron absorption cross section in ^{3}He has a $1/v$ dependence, so higher energy neutrons penetrate farther into the ion chamber on average. Therefore, currents collected at different segments along the beam sample different neutron velocity classes. The asymmetry for a parity-violating spin-rotation signal must be the same on all segments.

Both upstream and downstream targets are segmented into separate left and right halves along the beam axis, so that measurements of both target states can be simultaneously collected in order to suppress the effects due to magnetic field drifts. Furthermore, the ion chamber electrodes are segmented into left and right in order to take two-target data simultaneously and reduce noise due to reactor flux fluctuations (see Figure 4.4).

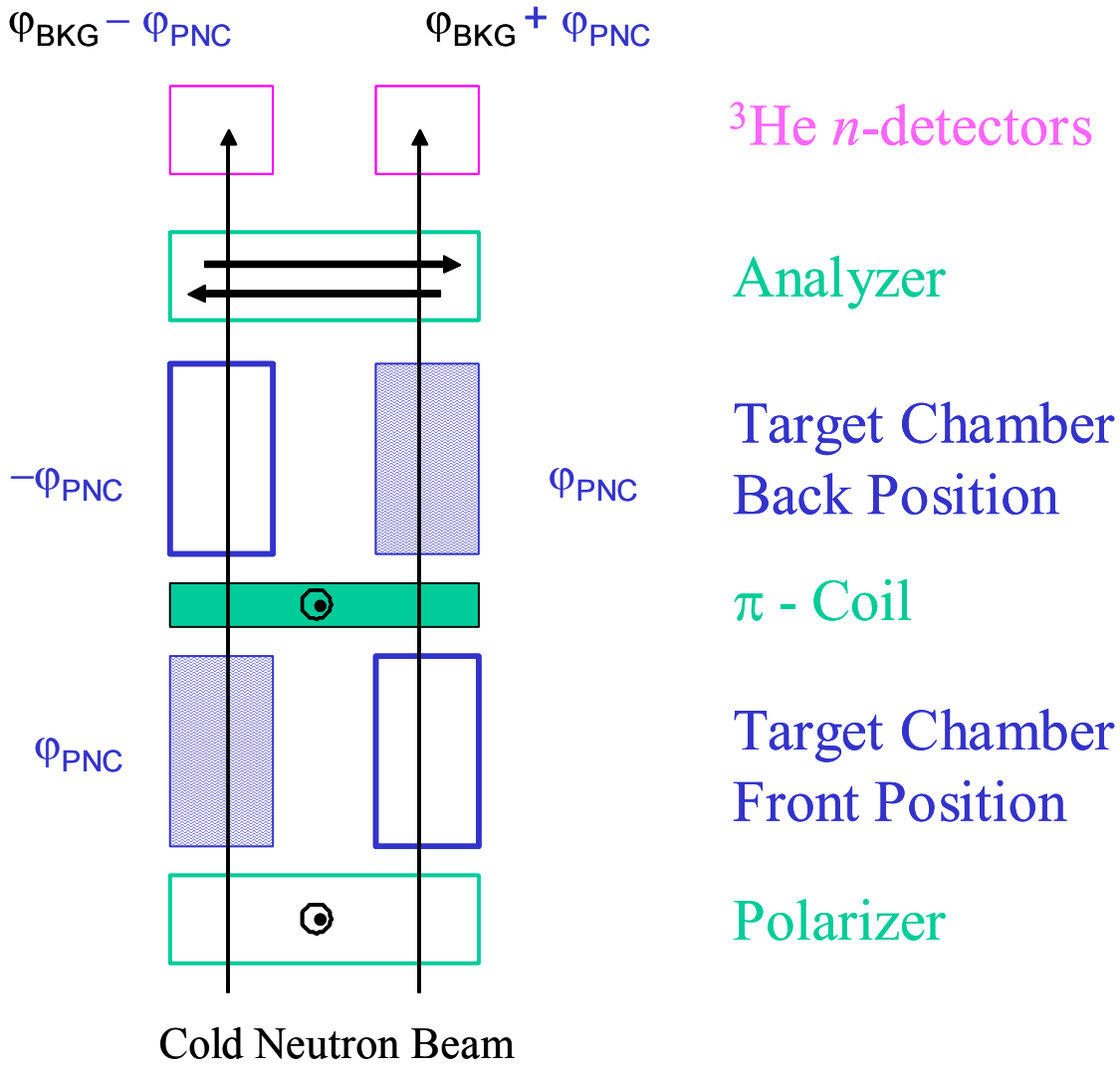

Figure 4.4: Diagram of parity-conserving (PC) and parity-violating (PV) rotations in the neutron polarimeter for a target state (top view). The PC rotations from the upstream and downstream targets are approximately cancelled by the pi-coil, while PV rotations are unaffected. Comparison of left and right sides effectively doubles the size of the PV signal against a residual PC background.

4.1 Constraints on residual magnetic fields in the target region

The parity-conserving rotations due to residual background fields in the target region can be effectively canceled out with the count rate asymmetry measurement, although smaller background rotations allow more precise asymmetry measurements to be made. Variations in the residual fields over time should occur on timescales longer than the length of a target state. However, the magnitudes of most systematic errors scale with the size of the residual field in the target region. As will be shown in the following section, a 100 μG or less residual field should suppress most systematic effects to a small enough size that they can safely be ignored with respect to the sensitivity of measuring $\varphi_{PV}(\vec{n},\ ^4\mathrm{He})$. Furthermore, non-uniformities in the residual field in the target region could generate different sizes of systematic effects that would change when the target state is changed. However, a 10% uniformity of a 100 μG residual field in the target region can suppress the size of most systematic effects by a further order of magnitude.

4.2 Discussion of statistical and systematic errors

Various experimental effects can introduce error into the spin-rotation measurement. These sources of error can be organized into three classes: (a) "multiplicative" effects that affect the scale of a true nonzero parity-violating signal, (b) effects that increase the noise in the measurement significantly beyond the statistical limit given by $\sqrt{N}$, and (c) systematic effects that produce a nonzero signal in the experiment, which is not due to parity-violating spin rotation. The required measurements needed to address the first two classes of effects are relatively straightforward, whereas the discussion of possible systematic effects is more extensive.

Given the expected size of the parity-violating spin-rotation angles in light nuclei and the brightness of present-day neutron sources, it is difficult to measure the parity violation observables in light nuclei to better than 10% statistical accuracy. Therefore,

the accuracy to which we need to know the product of neutron polarization and analyzing power of the neutron polarization analyzer *PA* is at the 10% level, which is not difficult.

The two largest sources of measurement noise above $\sqrt{N}$ statistics are expected to be from fluctuations in neutron intensity due to reactor noise, and extra noise in the ion chamber due to the current-mode measurement technique. The frequency band relevant for the spin-rotation experiment is around 1 Hz, which is the frequency with which the neutron spin-rotation angle is measured by alternating the projection of neutron polarization into the polarization analyzer by the adiabatic neutron spin transport. No precise measurements of reactor noise have been performed for the NG6 cold neutron beam in this frequency range. However, a time series analysis of neutron flux monitor data from the NIST neutron lifetime experiment that was sampled at 60 second intervals, combined with an assumed $1/f$ dependence to the source noise, implies that the spectral density of the noise in a 1Hz frequency band could be five to ten times larger than the $\sqrt{N}$ noise from the integrated number of neutrons in the same band [70]. In order to limit the effect of reactor fluctuation noise to $< 10\%$ of neutron counting statistics, the left and right sub-beams must possess the same noise to 1% accuracy. This constrains the accuracy that this noise is truly common-mode. Since both sub-beams accept cold neutrons from the same guide, and there are no known left-right asymmetries in this beam, this source of noise is expected to be common-mode to high accuracy.

The extra noise added by the operation of the ion chamber in current mode can be calculated. Since neutron capture in the ^{3}He of the ion chamber makes about 2×10^4 ions per neutron, the extra noise in the current signal is slightly less than 1% of neutron counting statistics. In addition, the ion chamber is designed to absorb 95% of incident neutron flux. Fluctuations in the fraction of the neutron beam absorbed by the ion chamber therefore add about 2.5% extra noise above neutron counting statistics. Therefore, neutron beam spectrum fluctuations that could also affect the fraction of neutrons absorbed in the ion chamber from the $1/v$ absorption cross section need to be sufficiently small and uniform across the two sub-beams.

By far the most serious systematic effects in parity-violating spin-rotation experiments are associated, directly or indirectly, with residual longitudinal magnetic fields. However, it is possible in principle to bound the size of such effects by increasing the longitudinal field to amplify the scattering systematics to a level where they can be measured. Over a 1 m target region, a 100 μG longitudinal field generates a spin rotation of about 2.5 mrad for a 5 Å neutron (and estimates of systematics in later sections will assume this residual field in the target region). In this case, if there is a systematic fractional difference in the magnetic field-induced rotations between the two target positions of 10^{-4}, then this effect is of the same size as our signal. Assuming that our goal is to suppress all systematic effects to a size that is 1/10 of the expected size of the parity-violating signal, we must ensure that the amount of magnetic spin rotation is the same upon moving the target to $\sim 1 \times 10^{-5}$ accuracy.

The size of some systematic effects can be calculated analytically or simulated by Monte Carlo, and we will discuss these first. Others depend in a complicated way on non-uniformities in the phase space properties of the neutron beam that couple to other asymmetries in the apparatus to generate a systematic effect. We will discuss these later and estimate the order of magnitude of accuracy that various phase space properties of the beam must be measured. We will also specialize to the particular case of a 40 cm liquid helium target for purposes of illustration, although very similar considerations also apply to other possible targets.

4.2.1 Diamagnetism of liquid helium

The presence of liquid helium modifies the vacuum residual magnetic field due to its magnetic susceptibility, $\chi_{\text{mol}} = -1.8914 \times 10^{-6}$ (cgs units) [71], which causes the residual magnetic field to change when the liquid is moved. For liquid helium at 4.2K, the change in the residual field is $\Delta B/B = 5.9 \times 10^{-8}$. The change of the residual background rotation due to the diamagnetism of liquid helium is of order 10^{-10} rad, which is a factor of 1000 smaller than the measurement goal. In addition, if the residual fields

in both target states are identical, then the effect cancels, so 10% uniformity can suppress this effect by another order of magnitude.

4.2.2 Optical potential of liquid helium

The presence of liquid helium slows down the neutron beam, which causes the neutrons to spend a longer time in the residual field. The neutron optical potential of liquid helium is ~10 neV. The kinetic energy of the beam is ~3 meV at 5 Å. The fractional change in neutron velocity with and without helium is $\sim 2 \times 10^{-6}$. In a 100 μG field, this causes a systematic effect of 1×10^{-9} rad at 5 Å for a 40 cm liquid helium target. A uniformity of residual fields at the 10% level suppresses this effect by another order of magnitude.

4.2.3 Shift in neutron energy spectrum

The neutron scattering cross-section over the spectrum of the cold neutron beam from the reactor is energy-dependent. This implies that the average neutron velocity shifts slightly after passing through the helium target. The magnitude of this shift scales with target length. Therefore, for targets of different length, the neutron velocity difference when coupled with a difference in the residual fields in the two target regions, gives a systematic effect. From the known energy dependence of the $\vec{n} + {}^4\mathrm{He}$ total cross section over the cold neutron beam spectrum and the target length, the estimate for the neutron velocity shift in liquid helium is $\Delta v/v \approx 0.04$. For a target length difference of 0.1 mm, which is the machined precision of the internal lengths for all four target chambers at room temperature at NIST, a 100 μG residual field generates an estimated 2×10^{-9} radian effect. Again, a 10% equality of the residual magnetic field suppresses this effect by a further order of magnitude.

4.2.4 Small angle scattering

In addition to the neutrons that pass straight through the liquid helium, some neutrons scatter, elastically or inelastically, through small angles within the phase-space acceptance of the polarimeter. The fraction of these scattered neutrons that reach the analyzer and then the detector can change when the target is moved, because the targets are different distances from the detector, and therefore the solid angle subtended by the detector and polarization analyzer is different. In addition, there are neutrons that multiple scatter in the target that could potentially get into the detector. Coupled with the extra spin rotation in the residual field, all of these effects can change the time that the neutron spends in the field in a target-dependent manner and lead to a systematic effect. This effect in general must be calculated using a Monte Carlo simulation that includes the properties of the target and the polarized neutron phase-space acceptance of the apparatus.

It is worthwhile making some general comments on neutron scattering in liquid helium. Calculations and measurements of the angular distribution of the scattering in liquid helium show that it has a significant dependence on neutron energy and helium temperature. At 2.5 meV, the total cross section of liquid helium has been measured [72] to change by 25% between 3K and 4K and the average cosine of the scattering angle is -0.2, corresponding to scattering into the backward hemisphere on average. The resulting neutrons have average energies below 1 meV, but at these energies the scattering is forward peaked, so multiple scattering events in which neutrons scatter twice in the helium and emerge in the forward direction are rare. It should be noted that this is not true of solid targets, which possess Bragg scattering and a nontrivial probability for multiple scattering back into the forward direction.

The neutron energy dependence of these effects is a result of destructive interference in the scattering from neighboring helium atoms, and the helium temperature dependence comes from the change in the number and spectrum of phonons in the liquid. In the small

momentum transfer limit where hydrodynamics can be used to calculate the spectrum of density fluctuations, there is a universal limiting form for the small angle scattering intensity that is given by thermodynamics [73]:

$$\lim_{q\to 0} S(q) \to \rho\kappa T \tag{4.2}$$

where $S(q)$ is the static structure factor, which gives the probability of scattering for a given momentum transfer, ρ is the fluid density, κ is the fluid compressibility and T is the temperature. In addition, recent measurements of small angle scattering intensity in normal and superfluid helium have also been performed [74, 75].

These scattering effects were simulated [76] using a model that gives the measured cross sections, including the small angle scattering data. Results showed that the contributions of each of these effects taken separately would be of order 10^{-8}, which is an order of magnitude smaller than the expected parity-violating signal. To understand that this result is not unreasonable, consider a crude estimate of the small angle scattering systematic. The solid angle accepted by polarization analyzer and detector from a target 120 cm away is $18\ \mathrm{cm}^2/[4\pi(120\ \mathrm{cm})^2] \approx 10^{-4}\mathrm{sr}$. The fractional difference in small angle scattered neutrons that enter the detector from the two targets is approximately 1×10^{-3}. This produces a fractional change in the time spent in the residual field by small angle scattered neutrons from upstream and downstream targets, which leads to a difference in spin rotation of 3×10^{-9} radians.

4.2.5 Change in neutron paths due to refraction or gravity.

For unscattered neutrons passing normal to all surfaces that can cause neutron refraction, there is no change in path due to the introduction of the liquid helium. However, for unscattered neutrons passing at an angle with respect to the normal, their trajectories will be bent slightly at each interface due to refraction. The presence or absence of the liquid helium will change the refraction angle slightly. The net effect of

this change is to cause this subclass of neutron trajectories to translate sideways slightly for target full and empty.

This is actually a subset of a large number of related effects that can change the beam path in a target-dependent manner and lead to intensity changes in the detector. For example, the density gradient in the liquid due to gravity gives a gradient in the neutron index of refraction in the helium that in principle can move the beam. In addition, the neutrons follow a curved path in the target region due to gravity, and one must worry if this causes a problem.

This beam motion can cause systematic effects in a number of ways. These include, but are not limited to: (a) intensity changes due to a different fraction of neutrons getting past the edge of the last collimator, (b) changes in the analyzing power of the analyzer due to the change in angular distribution of the neutron beam, (c) changes in the average residual magnetic field of 100 μG due to local gradients in the field.

Target-dependent shifts in the phase space of the beam from refraction effects are minimized by making the boundaries of all surfaces normal to the mean beam momentum. Since all neutron optical boundaries seen by the forward-going beam are normal to the neutron momenta, first-order effects from neutron refraction-induced changes in the neutron paths are suppressed. However, such effects still exist due to the finite beam divergence. Typical transverse neutron beam motion and angle shifts with the introduction of the liquid are of order 100 Å and 1 μrad, respectively, and it is a difference in these numbers for the two targets that is needed to generate a systematic.

4.2.6 Change in neutron paths due to spin-orbit interaction.

When a polarized neutron scatters from an atom, its magnetic moment interacts with the electric field of the atom. In the rest frame of the neutron, the electric field of the atom boosts to a magnetic field of size $\vec{B} = \vec{v} \times \vec{E}$. The magnetic moment of the neutron interacts with this field. The sign of the interaction $\vec{\mu} \cdot \vec{B}$ depends on which side of the

atom the neutron is incident. Thus, a potential gradient accelerates the neutron to one side and decelerates to the other side. Therefore, the trajectory of a polarized neutron moving through helium bends in a direction normal to its spin and momentum.

The sign of this effect is opposite for the positively charged nucleus and the negatively charged electron cloud; in the limit of spatially identical charge distributions, the net effect is zero. However, since the charge distribution is different, the cancellation is not exact. So there is a net motion of the neutron beam in the presence of the helium that is absent without the helium. This spatial beam motion can couple with other effects to create a systematic effect.

4.2.7 Change in gamma background detected in ion chamber

The ion chamber is mainly sensitive to neutrons, but gamma rays also create a small signal in the detector. When the liquid is moved, the gammas from neutron capture in the shielding around the targets, etc. are located at different distances to the ion chamber. This can cause a change in the intensity of the ion chamber signal that gives a systematic effect.

There is a related possible set of effects associated with changes in beam divergence. The analyzing power of the analyzer is a function of neutron energy and of the trajectory of the entering neutron direction. If the trajectories change slightly with target position, then the number of neutrons that capture in the analyzer and therefore the gamma radiation from the analyzer changes. In addition, the ion chamber is very close to the analyzer. This can create a systematic effect.

4.2.8 Change in neutron beam phase-space from reflections in target

An important effect at the edges of phase space acceptance comes from neutron reflection from the walls of the target. Since the critical angle for reflection is different for an aluminum-liquid helium interface and an aluminum-helium gas interface, any part

of the signal coming from reflections from the walls of the target chamber changes significantly in a target-dependent way. This possible systematic effect can be eliminated by introducing collimation into the target chamber to exclude wall-reflected neutrons from the phase space acceptance of the analyzer. Since the critical angle increases in proportion to the neutron wavelength, this also means that one should either measure or exclude long wavelength neutrons from the acceptance. This can be done by using a neutron wavelength cutoff filter.

4.2.9 Non-uniformity in the analyzing power of the polarization analyzer.

The intensity of neutrons transmitted through the neutron polarization analyzer is determined by it analyzing power, which is a function of neutron energy and beam divergence over the neutron energy spectrum and phase space distribution. There are non-uniformities in the analyzing power of the polarization analyzer within its phase space acceptance due to its reflection-based design and use of several stacked mirrors to cover the full size of the beam. Non-uniformity of the supermirror analyzing power coupled with a target-dependent change in the neutron beam phase-space can lead to a systematic effect. Monte Carlo simulations calculate that the difference in the fraction of non-forward scattered neutrons entering the analyzer is $\sim 1 \times 10^{-6}$. Phase-space changes occurring in a region where the analyzing power of the polarimeter varies rapidly can generate a systematic error. If 0.01% of the neutrons are on such an edge in analyzing power phase-space, these effects can generate a 1×10^{-9} effect. This estimate assumes a degree of uniformity of the analyzing power of the polarization analyzer as a function of the neutron beam phase-space. Measurements at NIST show that transverse non-uniformities of about 5% per mm and 1% per μrad exist in the analyzing power of the polarization analyzer due to the blades. When coupled with the effects listed above, the non-uniformities of the analyzing power are too small to generate a systematic effect.

4.2.10 Non-uniformities in the polarization product

Now let us consider non-uniformities in the polarization product *PA* of the beam polarization and the analyzing power of the polarization analyzer. The region of most rapid variation of this polarization product happens at the edges of the phase space acceptance of the supermirrors. Therefore, we want to design the neutron optics so that none of the transmitted neutrons are close to this phase space edge. In this experiment, this is done using geometry to force the maximum divergence angle of the transmitted neutrons to lie within the phase space acceptance of the analyzer and by using the choice of material for the neutron output guide, which is chosen to possess a smaller critical angle of reflection than the blades of the supermirror analyzer. These two choices ensure that the unscattered neutrons are not close to the edge of the phase space acceptance of the analyzer.

The fluctuations in the size of the polarization produced by the beam are negligible for the supermirror polarizer, which is a static device whose output polarization depends on its geometry, magnetic properties, and stability of the entering neutron phase space.

The efficiency of the polarimeter is given by its polarization product *PA*, which is defined as

$$PA = \frac{N_{\uparrow} - N_{\downarrow}}{N_{\uparrow} + \varepsilon N_{\downarrow}} \tag{4.3}$$

where $N_{\uparrow}$ and $N_{\downarrow}$ are neutron count rates through the polarimeter with the RF spin-flipper turned off and on (respectively), and ε is the spin flip efficiency of the RF spin-flipper, which is estimated as 0.95 ±0.05 [77].

For the transmitted beam one can imagine that non-uniformities in the incident beam phase space could couple with scattering in the target and the polarization analyzer non-uniformities to generate a systematic effect. Clearly, such an effect cannot be analyzed in

general and simply must be measured experimentally. In this work, we measure that subset of such effects which comes from the polarimeter and the beam optics.

4.2.11 Pi-coil leakage fields

The pi-coil possesses external leakage fields and internal longitudinal fields that are difficult to characterize accurately. Although these residual fields should reverse in sign by reversing the pi-coil current (the main vertical field component will still precess the neutron polarization), the 1996 NIST experiment saw indirect evidence for a lack of cancellation of these fields that was not understood [34]. During calibration runs, the pi-coil was rotated about its vertical axis by π radians to check for systematic effects due to internal fields, and the current was reversed to check for systematic effects due to leakage fields. Based on measurements during data runs by the fluxgate magnetometer sensors located closest to the pi-coil, the leakage fields reversed with current to high accuracy.

5 Neutron Beam and Polarimeter Apparatus

The NIST Center for Neutron Research (NCNR) in Gaithersburg, Maryland centers around a 20 MW research reactor (see Figure 5.1). D_2O moderates the fission neutrons produced in the reactor down to thermal energies. Adjacent to the reactor core is the cold source, which moderates thermal neutrons down to meV energies through scattering and consists of five liters of liquid parahydrogen held at 20K inside an ellipsoidal shell [78].

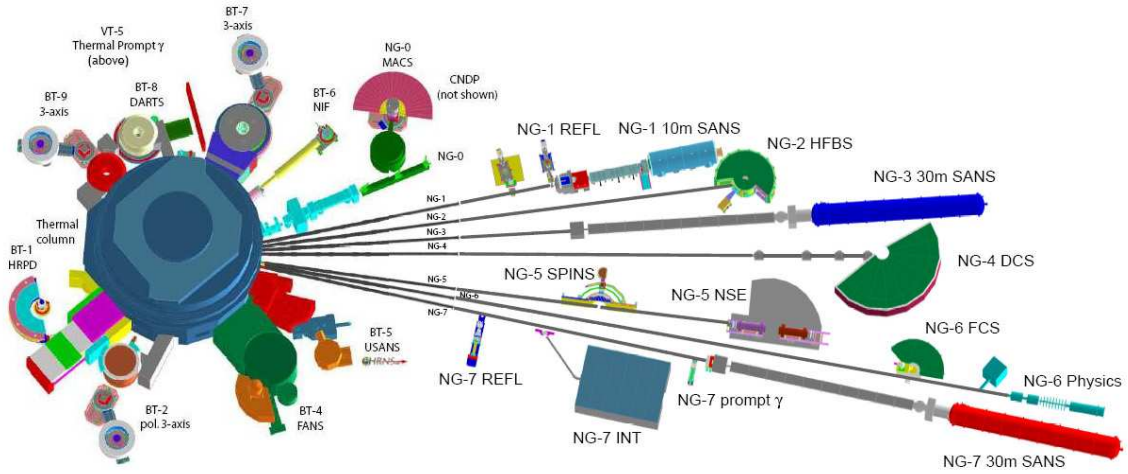

Figure 5.1: Diagram of the guide hall beam lines at the NCNR. The neutron spin-rotation experiment is located on the NG-6 end station.

5.1 Neutron beam

After neutrons exit the cold-source, they enter evacuated, rectangular guide tubes with cross-sectional area of 15 cm vertical and 6 cm horizontal. These guides are coated with ^{58}Ni, which has a critical angle of 2.1 mrad /Å, and they reflectively transport the neutrons tens of meters with minimal losses to the experimental areas. The neutron spin-

rotation experiment is located 68 m away at the end station of the NG-6 polychromatic beam line.

The NG-6 beam is split into upper and lower halves for independent use by the end station and two monochromatic beams, respectively. The upstream monochromator (NG-6M) consists of a piece of pyrolytic graphite that Bragg reflects a 4.96 Å beam by ~104° with respect to the primary beam. The downstream monochromator (NG-6U) uses potassium intercalated graphite crystal to direct a 8.9 Å beam by 60° from the main beam. The polychromatic upper half of the beam passes through a thin magnesium window and travels through 79 cm of air to a ^{6}LiF glass collimator that defines a 6 cm diameter beam. Neutrons pass a remote-controlled beam shutter at the NG-6 end station.

5.2 Neutron transport

Once neutrons pass the beam shutter, they enter the neutron spin-rotation apparatus (see Figure 5.2). The beam passes through 10 cm of polycrystalline beryllium, which scatters out neutrons with wavelengths smaller than twice its interatomic spacing ($\lambda = 3.96$ Å), and 10 cm of monocrystalline bismuth, which stops gamma rays and transmits neutrons. These filters are held at 77K in order to reduce beam losses due to phonon scattering, which results in a factor of two transmission increase over room temperature filters [79]. The beam then passes through a 50 mm tall by 60 mm wide ^{6}LiF glass collimator that defines the beam cross section area.

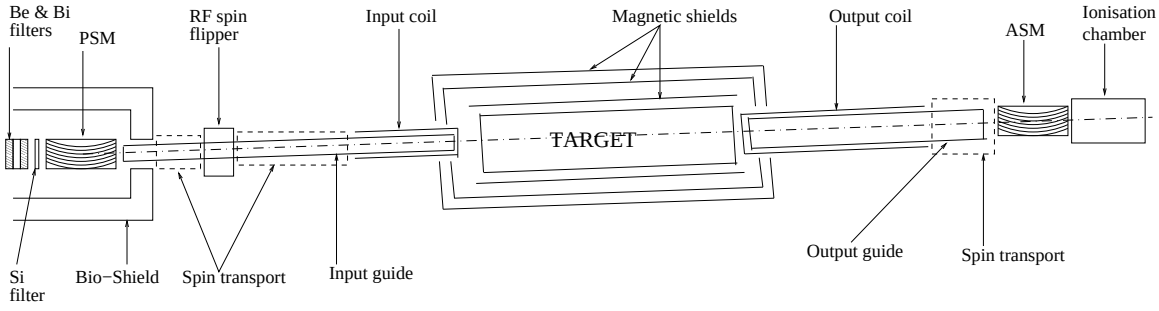

Figure 5.2: Diagram of the neutron beam path through the spin-rotation apparatus.

The beam then enters a neutron supermirror polarizer, which is based on a multilayer Soller "beam-bender" supermirror design [80, 81] that polarizes neutrons through spin-dependent scattering from magnetized mirrors (see Figure 5.3). A set of 45 Pyrex glass plates are coated with alternating layers of ferromagnetic material (cobalt) and neutron absorbing material (titanium and gadolinium) and stacked together with 1 mm spacing between each. The plates are curved into a 10 m radius so that incident neutrons must reflect from at least one supermirror layer during passage through the polarizer.

The supermirror stack is housed within a 300 G permanent magnetic box, which provides a saturating magnetic field for the magnetic multilayers. Neutrons with magnetic moments parallel to the magnetic field are reflected, while all other neutrons are transmitted through the multilayer and absorbed in the gadolinium. Typical beam polarization by the supermirror polarizer is 98% with beam transmission of 25% [81]. The cross section area of the transmitted beam upon exiting the polarizer is 45 mm tall by 55 mm wide. Due to reflections from the supermirrors, the transmitted beam deflects by 14 mrad with respect to the incident beam direction on the polarizer.

Upon exiting the supermirror polarizer, the polarized beam enters the input neutron guide, which consists of two sections that are each 100 cm long with inner dimensions of 44 mm wide by 45 mm high. The guides are made from machined borosilicate float glass (4% boron by weight) that are mechanically bonded together with UV-cured LocTite 349 acrylic adhesive. Aluminum foil (Reynolds) windows are glued onto the ends of each guide. Small hoses connected to the ends of each guide section allow helium gas to flow through the guide volume and displace any air. This also reduces beam intensity losses in the guide due to neutron scattering from air. After travelling through the guide, neutrons pass into the zero magnetic field target region.

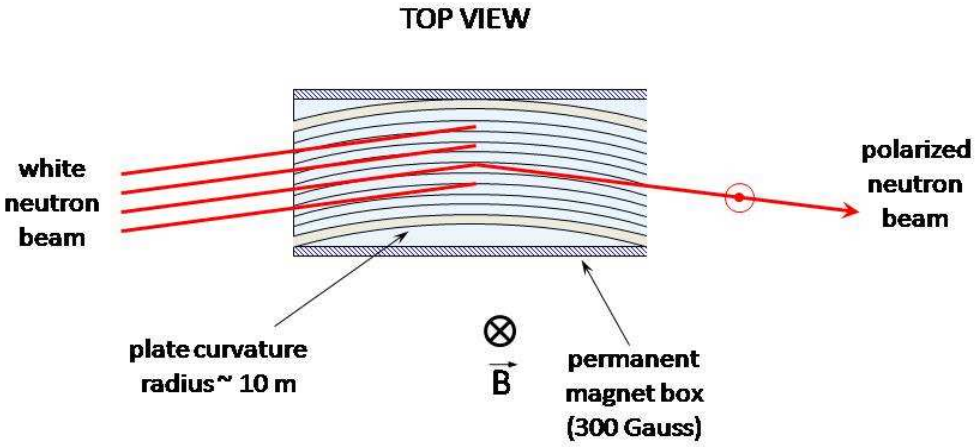

Figure 5.3: Diagram of the supermirror polarizer (top view). Neutrons with magnetic moments parallel to the saturating field are reflected from curved glass plates coated with a ferromagnetic material and pass through the polarizer; neutrons with antiparallel moments are transmitted through the glass plates and are absorbed within the polarizer.

Once the neutrons have passed through the target region, they enter an output guide of similar construction as the input guide. However, the output guide has a thin septum to partition the left and right sides of the beam after it leaves the target region (see Figure 5.4).

Neutrons then pass into the neutron polarization analyzer, which is similar in design to the supermirror polarizer, except it has 55 curved plates instead of 45, and only the central plates are coated with ferromagnetic material on both sides. Additionally, the neutron polarization analyzer accepts a larger beam cross section area: 45 mm tall by 60 mm wide. Neutrons then pass into the ion chamber, where beam count rates are measured.

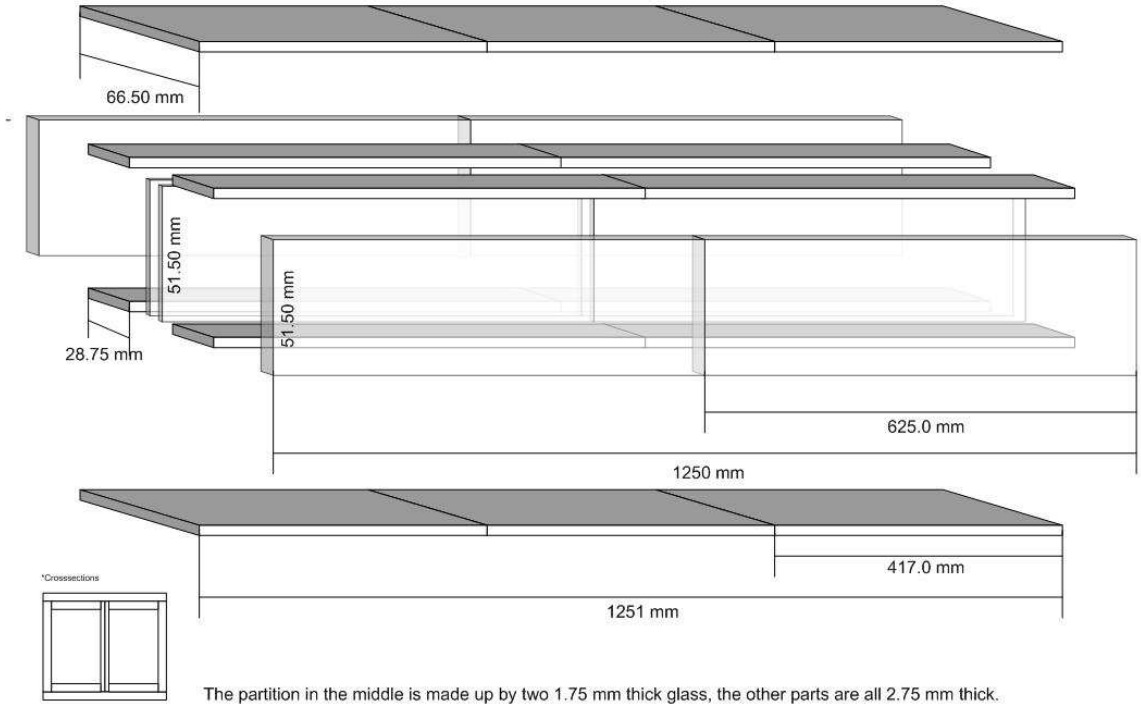

Figure 5.4: Diagram of the output guide construction. Multiple pieces of borosilicate float glass are assembled using UV-cured acrylic adhesive for mechanical strength and sealed on the outer seams with RTV to eliminate gross air leaks. Aluminum foil windows cover each end. Small access ports above each end (not shown) allow helium gas to flow through the guide and displace air within the volume.

5.3 Spin transport

The spin transport is designed to guide polarized neutrons from the supermirror polarizer into the target region without depolarizing them and without producing large stray magnetic fields. Neutrons pass non-adiabatically into a zero magnetic field region that surrounds the target. The zero-field target region is maintained by passive and active magnetic shielding. After passage through the target, neutron spin non-adiabatically passes into a guide coil that transversely rotates the neutron spin by $\pm\pi/2$ radians. This

rotation allows the polarimeter to have the neutron polarization analyzer mounted vertically instead of horizontally. By alternating the direction of the $\pi/2$ rotation of the neutron spin, the orientation of the neutron polarization analyzer can effectively be reversed, which allows the transverse component of the neutron spin to be analyzed by the neutron polarization analyzer. The small transverse component of the neutron spin contains the spin-rotation information. The intensity difference of transmitted beam through the neutron polarization analyzer that enters the neutron detector for the two polarization analyzer states is proportional to the neutron spin-rotation angle.

5.3.1 Adiabatic RF spin-flipper

Mounted around the input guide between the supermirror polarizer and the input coil is an adiabatic RF spin-flipper based on the design by Bazhenov [82] and Grigoriev [83]. The spin-flipper consists of two orthogonal magnetic fields: an oscillating RF field and a static gradient field. As neutrons pass through the device, the gradient field causes the neutron spin to adiabatically follow the RF field through a rotation of π radians with high calculable probability. One key advantage of this design is that the near unity spin-flipping efficiency is relatively independent of neutron energy.

The RF spin-flipper design constraints bound its length to 28 cm and require the solenoid that generates the oscillating RF field must fit around the input guide tube. In addition, the static gradient field requires mechanical adjustability in order to shape the desired field. Since powering on or off the solenoid generates undesired back-EMF that can destroy the spin-flipper electronics, power to the solenoid is not simply turned off, but instead switched to an identical offline "dummy" solenoid of similar complex impedance.

A diagram of the spin-flipper is shown Figure 5.5. A pair of steel plates is loaded with arrays of small ceramic magnets and is positioned above and below the input guide at some angle α. The arrays are configured so that the resulting magnetic field is oriented vertically "up" ($+\hat{x}$-direction). The solenoid is constructed by wrapping wire around a

12.3 cm diameter glass cylinder and coating it with a layer of epoxy. The solenoid is mounted around the input guide and between the gradient field plates.

The spin-flip efficiency is determined by measuring the ratio of the count rates through the polarimeter for unflipped and flipped states of the RF spin-flipper. The efficiency is a function of applied RF power and is practically limited by circuit overheating.

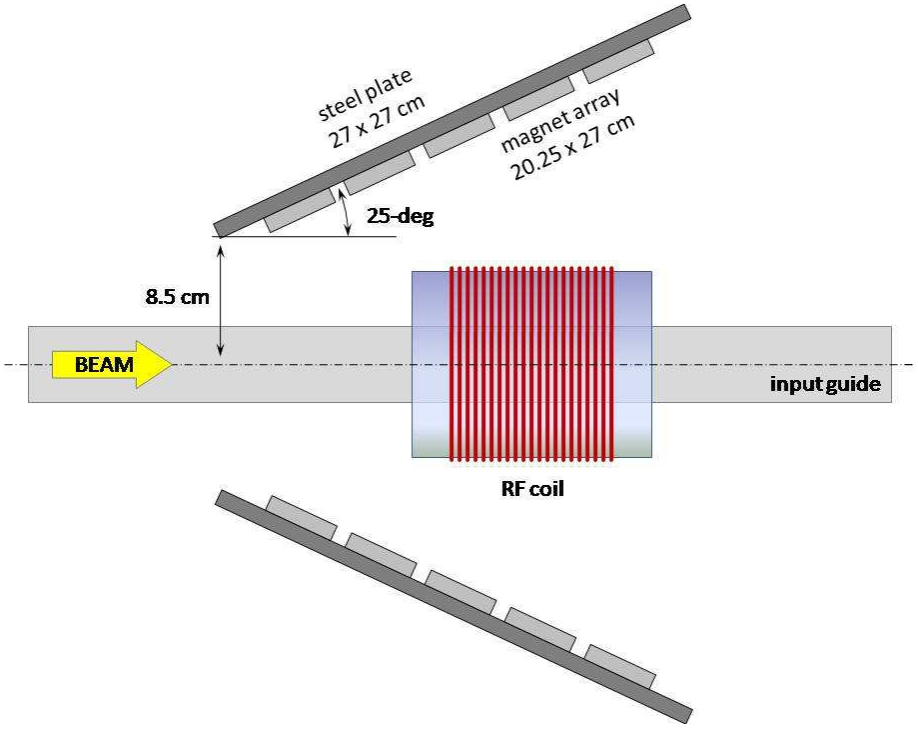

Figure 5.5: Diagram of the RF spin-flipper (side view). The solenoid is suspended around the input guide and secured in place with an aluminum frame (not shown). The magnetic gradient plates are mounted above and below the solenoid and are secured to the aluminum frame with mounting brackets that allow angular and position adjustability.

5.3.2 Input coil

The input coil is designed to generate a constant, flat vertical magnetic field that terminates non-adiabatically across a current sheet at its downstream end (Figure 5.6). The strength of this field is set to match the field produced by the supermirror polarizer 300 G permanent magnet housing located 2 m upstream, which is about 5 G at the entrance of the input coil. This preserves the neutron polarization as neutrons pass into the target region.

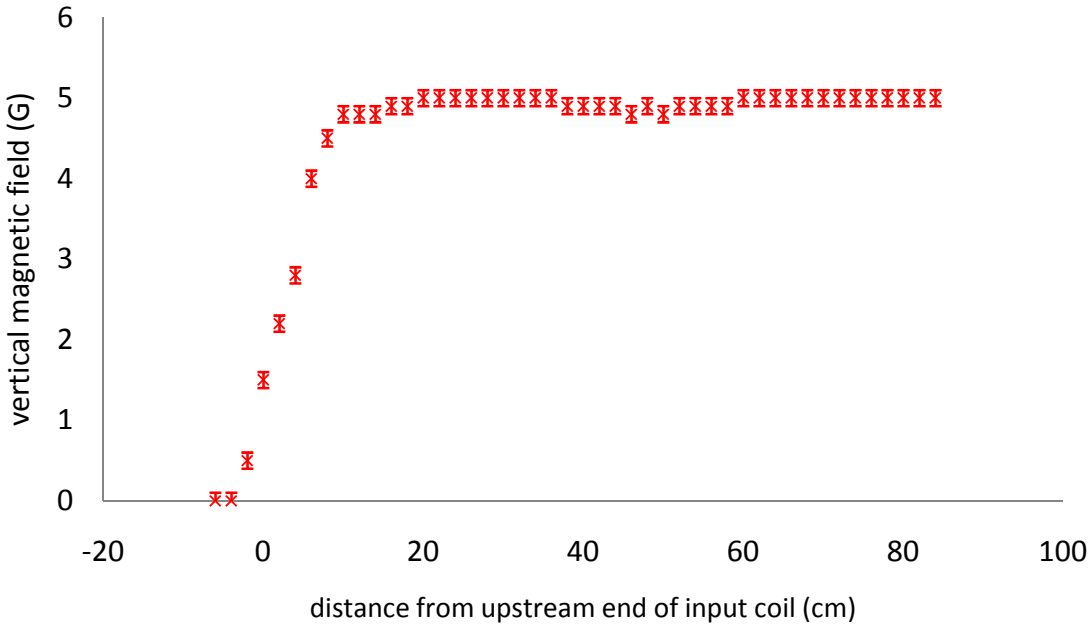

Figure 5.6: Plot of the measured vertical magnetic field within input coil.

The input coil consists of an 81.3 cm long hollow main core built from nonmagnetic G10 sheet. This main core is dimensioned so that the input guide easily slides into it. Flux return cores are positioned adjacent to the main core on the left and right sides. Copper wire is wrapped tightly around each core and glued in place to minimize winding

imperfections and to protect wires during handling (see Figure 5.7, adapted from [34]). Power is supplied by an HP 6294A DC power supply.

The width of each return core is ¼ of the main core, requiring two sets of windings on each to return the magnetic flux of the main core. To assist the flux return and improve magnetic field homogeneity within the beam path region of the main core, μ-metal sheets were placed across the main and return cores on the top and bottom of the input coil. These μ-metal pieces can be degaussed while the coil is mounted on the beam line.

Across the downstream end of the main core, the sections of copper windings in the beam path are replaced with 1 mm diameter aluminum wire to form a current sheet. The windings on the upstream end of the main core form a gap to allow insertion of the guide into the input coil.

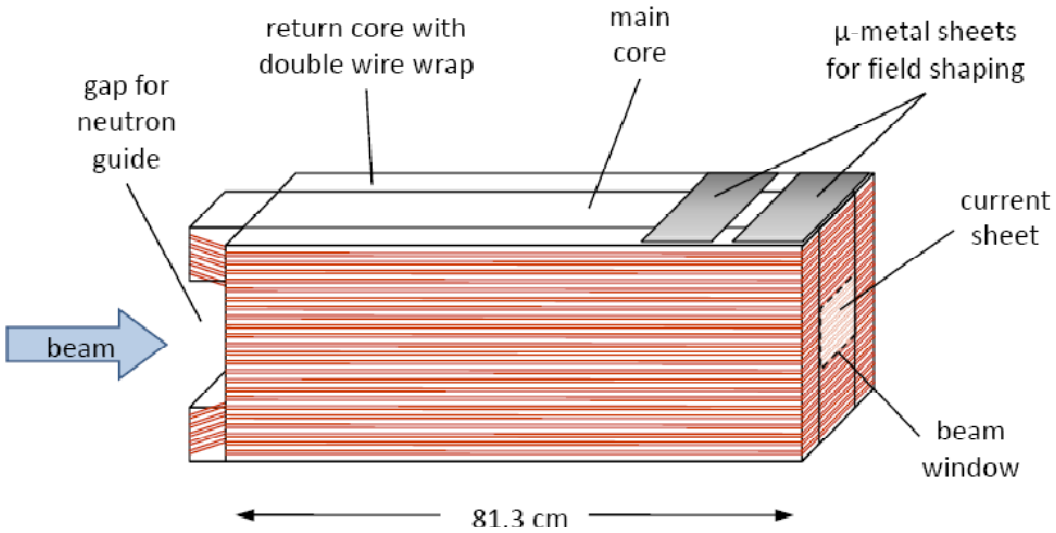

Figure 5.7: Diagram of the input coil (side view). The pair of return cores sandwich the main core on left and right sides. The main core is hollow and accepts the input guide from the upstream end of the coil, while the downstream end of the coil terminates in a current sheet.

5.3.3 Magnetic shielding

Most systematic effects couple to residual magnetic fields in the target region. In order to achieve the desired measurement sensitivity, magnetic fields in the target region need to be less than 100 μG (compare this with the Earth's magnetic field of 500 mG). Changes in the residual magnetic fields must be small and occur over time scales that are long compared to the measurement time for a target state. These conditions set the magnetic shielding constraints.

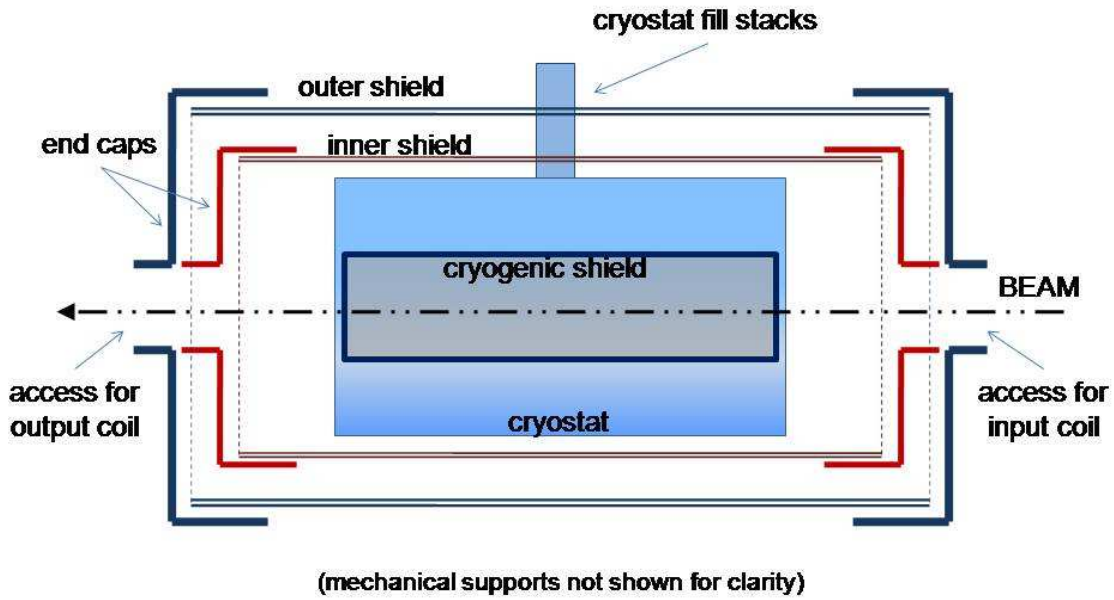

Figure 5.8: Diagram of the magnetic shielding configuration (side cross-section view). The cryostat is surrounded by the outer magnetic shields, and the cryogenic magnetic shield is positioned within the cryostat cold bore. The outer shields have openings for the input coil, the output coil, the cryostat fill stacks, and mechanical supports for the cryostat and the inner layer of magnetic shielding.

The magnetic shielding consists of outer and inner cylindrical, nested μ-metal magnetic shields with end caps, and a cryogenic cylindrical μ-metal shield (no end caps) that is mounted in the cold bore of the cryostat (see Figure 5.8). Additionally, a set of compensation coils are mounted around the outside of the entire apparatus, and trim coils are mounted on the outside of the target vac-canister, which itself is located interior of the cryogenic shield.

The sizes of the shields were constrained by practical physical limitations and cost considerations. The outer shield is 240 cm long by 97 cm diameter and built from 62 mil thick Co-netic AA μ-metal. The inner shield is 180 cm long by 78 cm diameter and built

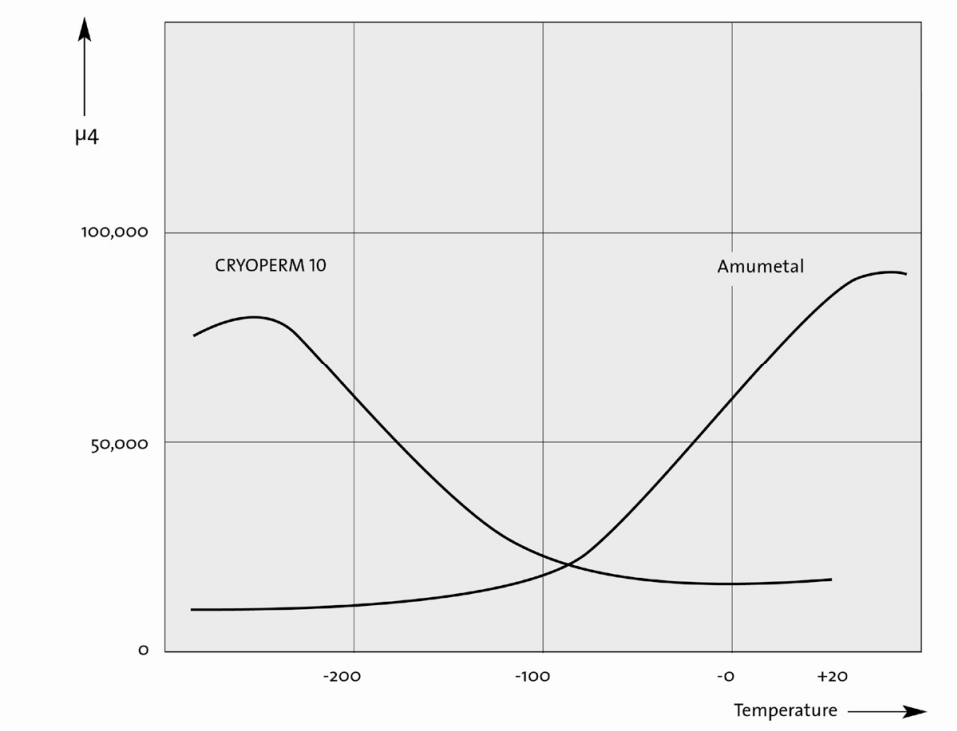

Figure 5.9: Plot of the temperature dependence of Cryoperm permeability, as provided by the manufacturer, Amuneal Corp.

from 50 mil thick Co-netic AA μ-metal. Both the outer and inner shields completely enclose the cryostat, except for access holes that allow the cryostat fill stacks and support posts to penetrate the shields. Additional 30 cm by 15 cm slots are cut into each end cap along the beam axis to allow the input and output coils to extend past the shields.

The cryogenic magnetic shield is a 100 cm long by 30.5 cm diameter cylinder fashioned from 1.5 mm thick Amuneal Cryoperm-10 μ-metal. This material was chosen since the permeability of most commercially available nickel-steel magnetic shielding decreases with temperature, while the permeability of Cryoperm at 4K is comparable to that of normal μ-metal at room temperature (Figure 5.9).

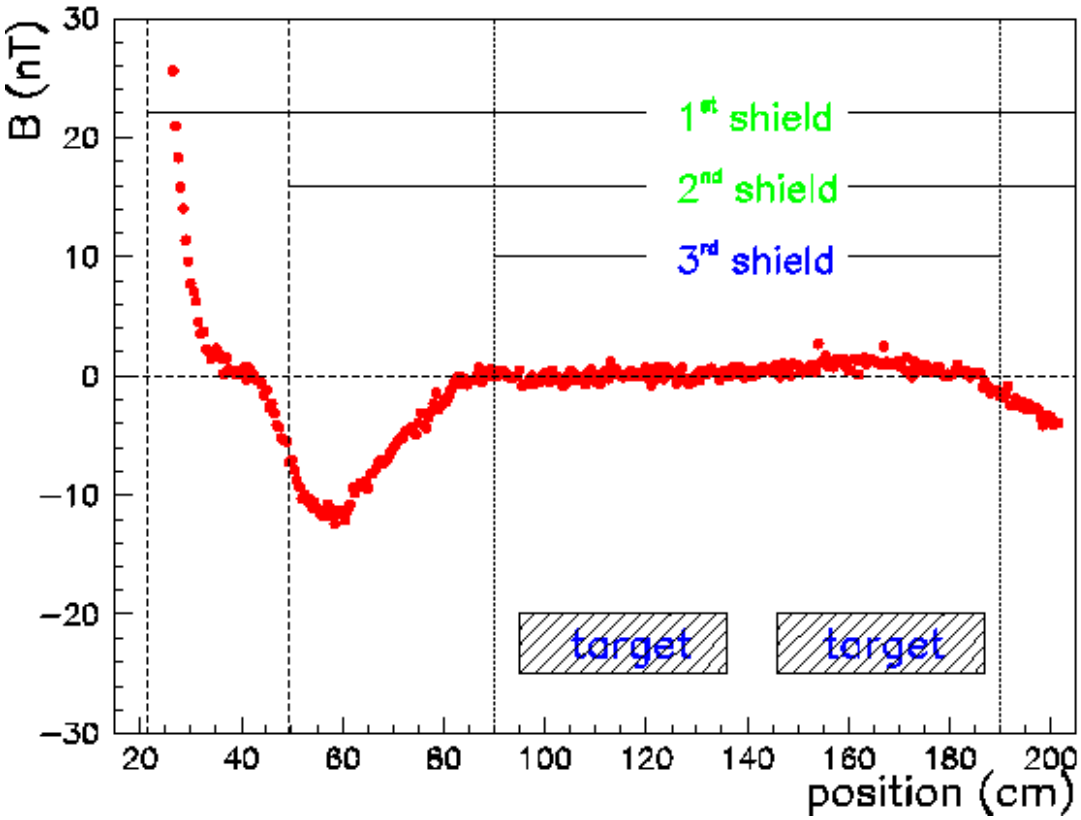

Figure 5.10: Plot of longitudinal fields in the magnetic-shielded region. Measurement is for three nested μ-metal shields, with end-caps installed on the outer two shields, the cryogenic shield at 300K, and no active shielding.

A Bartington Mag-01H type-F fluxgate magnetometer sensor is located approximately 1 cm inside the inner surface of the inner magnetic shield. This sensor provides the input for the PID-controlled compensation coil that surrounds the outer magnetic shield. This system uses the sensor information to generate an external field that damps out undesirable magnetic field changes that occur in the guide hall environment (e.g. the magnetic field ramping sequence of the Spin-Echo instrument).

Wrapped on the outside of the target vac-canister are 10 trim coil loops, which are spaced 7.6 cm apart along the entire length of the vac-canister. DAQ-controlled current-sources supply each coil independently to allow fine-tuning of the magnetic field in the target region.

At IUCF, the longitudinal magnetic field along the beam axis was mapped for all three nested shields (see Figure 5.10). The outer two shields had end caps installed, and the cryogenics shield was at 300K, so its permeability was roughly one third of what it would be at 4K. The compensation coils and trim coils were inactive. The longitudinal field was measured to be less than 20 μG in the target region.

During the commissioning of the experiment apparatus at NIST, a measurement of the longitudinal fields along the beam axis was performed using only the outer magnetic shields. As seen in Figure 5.11, the measured residual fields in the target region were less than 100 μG. Increased shielding performance in the target region is expected with the addition of the cryogenic magnetic shield, the field trim coils around the vac-canister, and the PID-controlled compensation coils.

Because μ-metal slowly acquires magnetization over time, it is periodically necessary to degauss the magnetic shields in order to restore the full permeability of the shielding material. To do this, two separate toroidal coils wrap around the shields – a 7-loop coil around the outer two magnetic shields and a 40-loop coil around the cryogenic shield. These coils are wired together in series to a Variac. The optimal degaussing procedure used about 125 amp-turns at room temperature. A 60 Hz AC current is ramped from 0 to

5 amps over 30 seconds, held at 5 amps for 30 seconds, then ramped back down to 0 amps over 30 seconds.

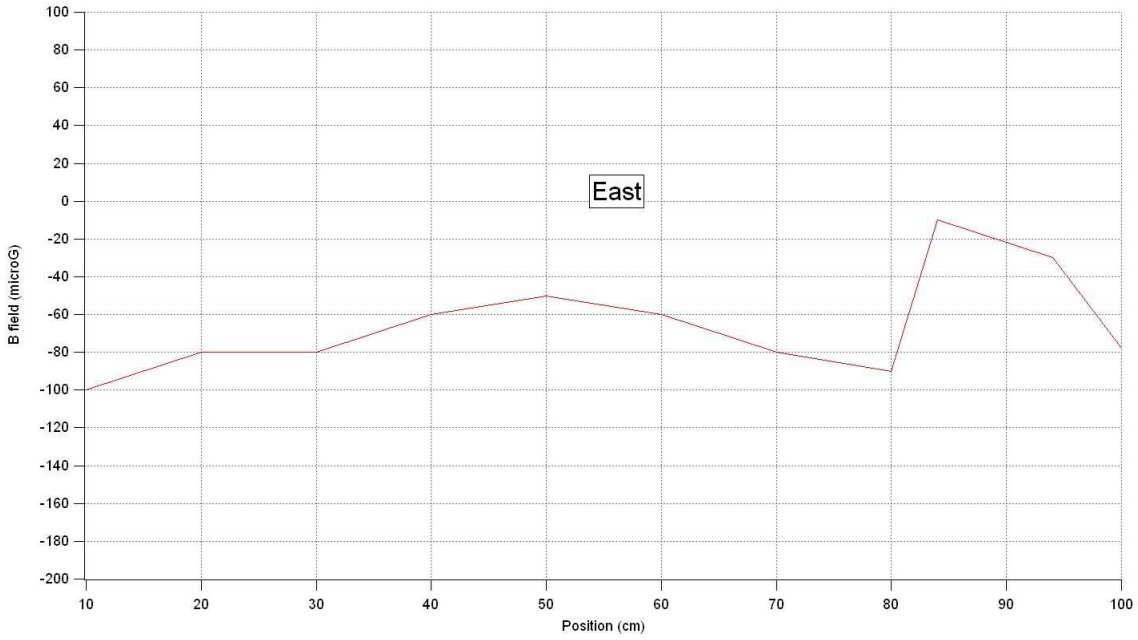

Figure 5.11: Plot of longitudinal fields in target region at NIST. Measurement used only two outer magnetic shields.

5.3.4 Output coil

After exiting the zero magnetic field target region, neutrons pass non-adiabatically into the output coil, which provides spin transport from the target region into the polarization analyzer in a similar method as the input coil. The main core is wound around a 96.5 cm long G10 core with inner dimensions large enough to accept the output guide (see Figure 5.12, adapted from [34]). A current sheet made from 1 mm diameter aluminum wire is located on the upstream end of the coil. Return coils are located on the top and bottom of the main core. This main coil generates a static vertical field of a few Gauss along the length of the output coil.

However, the output coil has an additional coil whose winding density increases with downstream position along the output coil and generates a horizontal field that increases with position along the coil (see Figure 5.13). When combined with the main field, the second coil rotates neutron spin by $\pi/2$ radians. Furthermore, the current for the second coil is computer-controlled to modulate in sign, so that the horizontal field will change signs. This allows the output coil to adiabatically rotate the neutron spin by $\pm\pi/2$ radians as neutrons are transported into the polarization analyzer. The output coil static vertical field is supplied by a HP 6286A DC power supply, and the alternating horizontal field is supplied by a Kepco BOP 20-5M bipolar power supply.

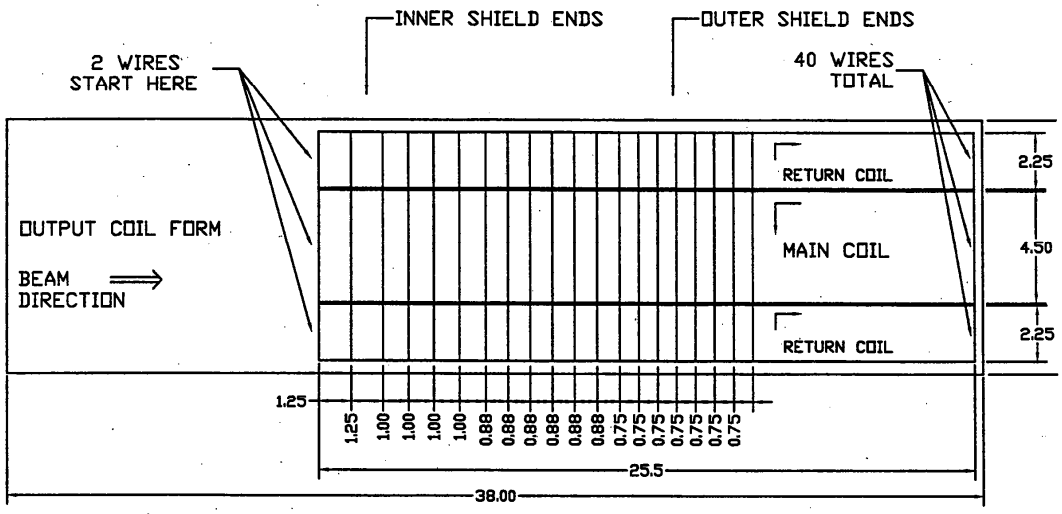

Figure 5.12: Diagram of the output coil showing the winding density of the flipping coil.

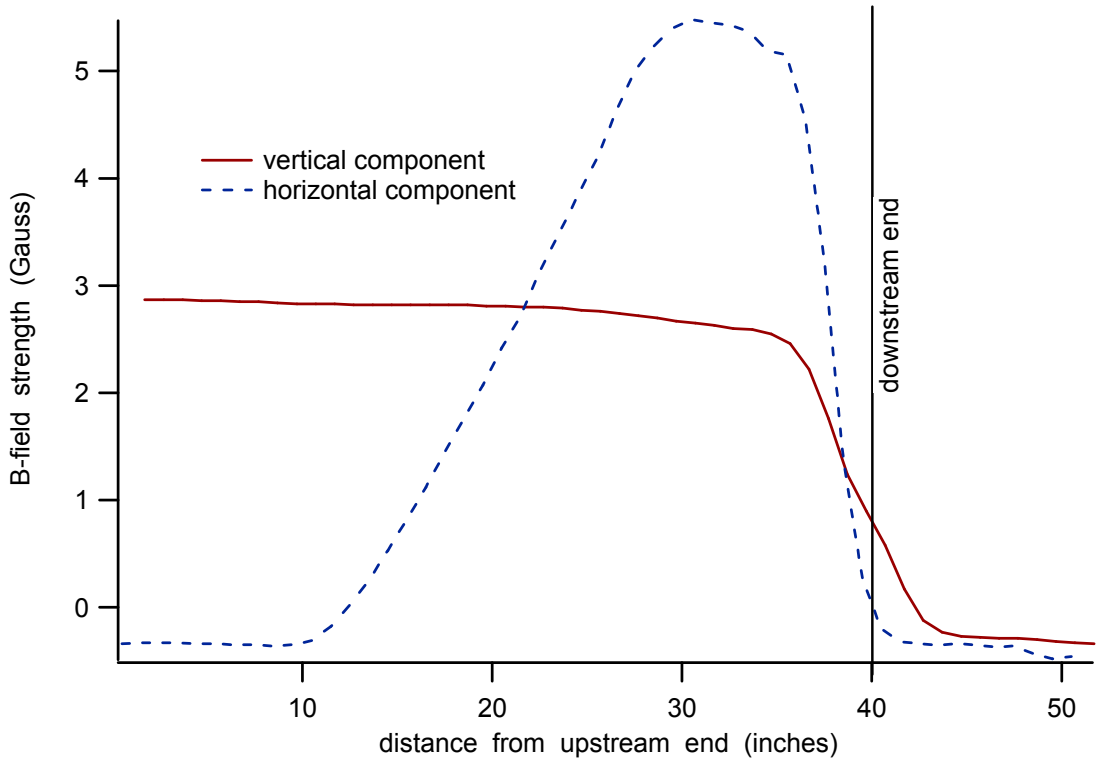

Figure 5.13: Plot of magnetic field inside the output coil. The main coil generates a static vertical field, while the flipping coil generates a horizontal field that increases along the length of the output coil. The sign of the horizontal field flips at a rate of 1 Hz during operation, thus rotating the neutron polarization vector alternately ± π/2 radians into the polarization analyzer.

5.4 Neutron detector

A current mode ^{3}He ion chamber is used to monitor the transmitted neutron beam. This type of detector has a well-understood detector efficiency as a function of neutron energy, a low gamma sensitivity, and a negligible gamma production within the device itself.

Figure 5.14 shows a diagram of the ^{3}He ionization chamber concept originally designed by Penn *et al.* [84] and modified by Blessinger [85] and Luo [86]. The chamber consists of a series of interspaced high voltage and grounded charge collecting plates,

which divide the detector volume into longitudinal segments. Half voltage annular rings are positioned between each high voltage plate and collection plate in order to shape the electric fields and to reduce fringe fields and sparking. The volume is filled with ^{3}He and a buffer gas.

Neutrons are detected through the following reaction:

$$n + {}^3\mathrm{He} \rightarrow {}^3\mathrm{H} + p + 0.78\ \mathrm{MeV} \tag{5.1}$$

The triton and proton ionize the gas mixture as they slow down. An average energy of 28 eV is required to produce an ion pair, so on average each absorbed neutron produces approximately 2.5×10^4 ion pairs. The electric fields produced by the high voltage rings

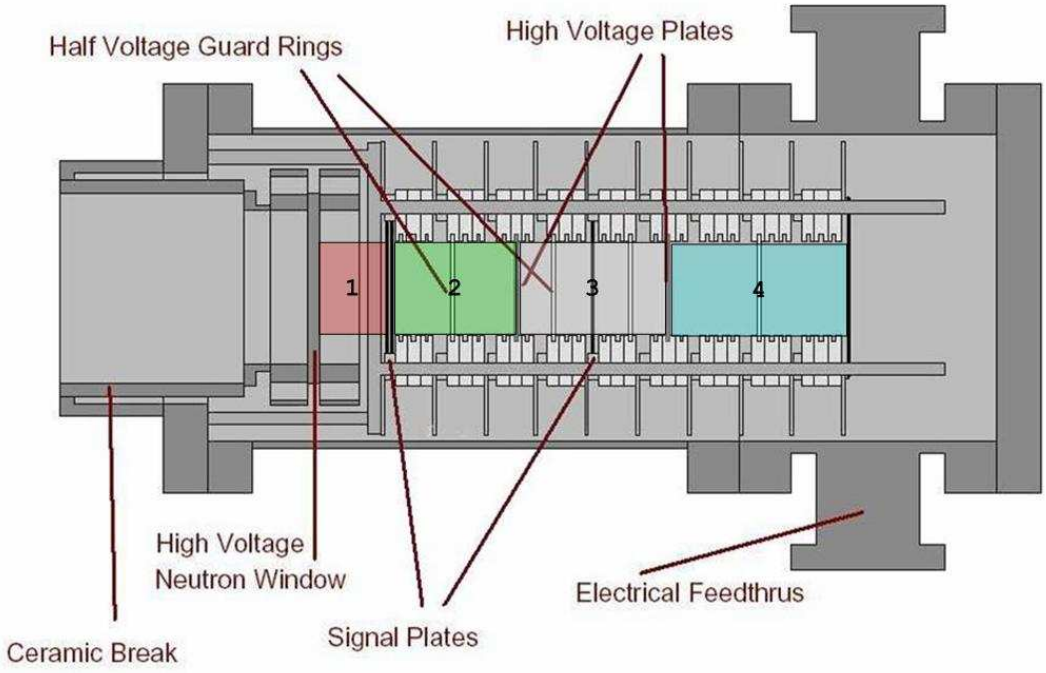

Figure 5.14: Diagram of the ^{3}He ionization chamber. Shaded area show the longitudinal segmentation of the detector for charge collection plates 1-4.

direct the ion pairs onto the grounded charge collection plates. The electronics used to integrate and read the current from each plate is discussed in Section 5.5.

The collection plates are divided into four quadrants each, so that left and right sub-beams from the target – as well as top and bottom halves – can be independently monitored. The plate quadrants are separated by 3 mm gaps and are labeled as shown in Figure 5.15.

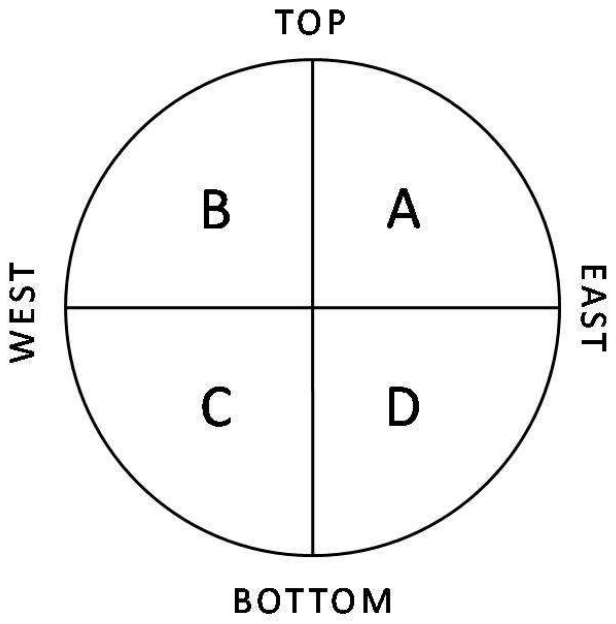

Figure 5.15: Diagram of detector plate quadrant identification. East and west directions are orientations within the guide hall at the NCNR (3 mm gaps between quadrants not shown for clarity).

The neutron absorption and proton range characteristics of the detector are determined by the pressure and composition of the gas mixture. A partial pressure of 167 Torr of ^{3}He was chosen to capture 98% of the neutron beam. Argon at a partial pressure

of 2280 Torr was chosen as the buffer gas to set the proton range to less than 3 mm. This range constraint for the proton is set by the 3 mm gaps between charge collection plate quadrants and the 3.5 mm partition thickness of the output guide, which determines the separation distance between left and right sub-beams. It is this sub-beam separation distance and the proton range within the detector that set the minimum amount of cross-talk between left and right-side detector plates. Cross-talk has been measured to be between 5% and 20%, but this included effects due to the relative misalignment of the detector with respect of the beam.

The ^{3}He absorption cross-section is proportional to $1/v$, so the distance that a neutron will penetrate into the detector before it is absorbed is proportional to its incident energy. Since the parity-conserving signal scales with neutron energy, but the parity-violating signal is independent of neutron energy, knowledge of the beam energy spectrum can serve as a valuable check on rotations due to residual fields. The energy resolution of the detector increases with the number of collection plates. However, each plate has a statistical noise associated with it, so signal resolution decreases with the number of plates. Simulations were performed [87] to study the overall statistical error as a function of the number of plates in the detector (see Figure 5.16). For this detector, the optimal number of plates was determined to be four. Additional plates beyond this amount provide only a minimal increase in signal (e.g., ten plates provide only a 2% improvement over four plates).

For the ^{3}He gas mixture and position of the four collection plates, the calculated fractions of neutrons absorbed for plates 1 through 4 (counting upstream through downstream) are 24%, 24%, 40%, and 12%.

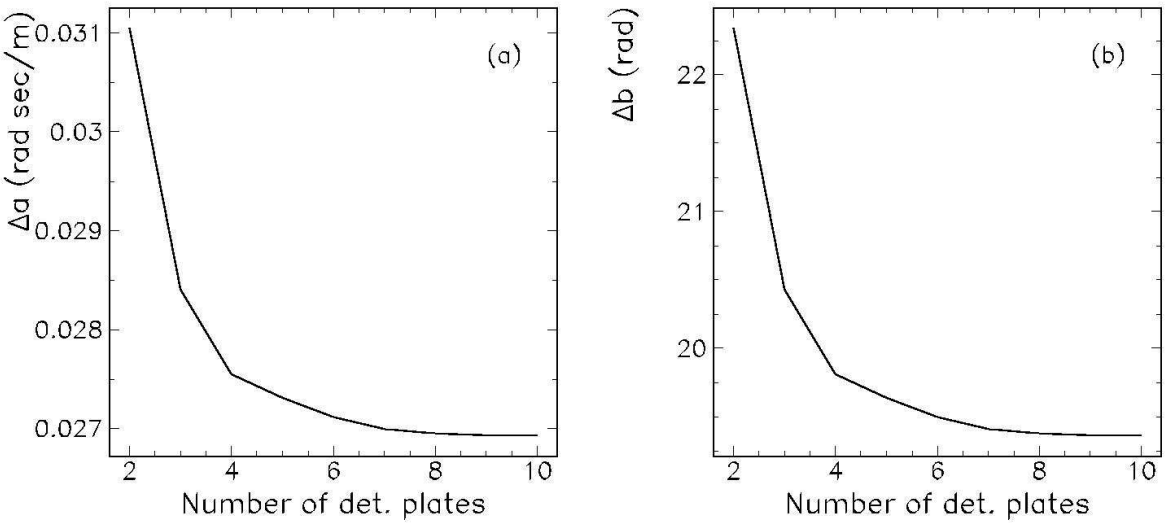

Figure 5.16: Plot of the number of charge collection plates as a function of signal error. Errors are given as: $a(1/V) + b$, where V is neutron velocity.

5.5 Signal processing and experimental control

Signals from the ion chamber are routed through combined integrator and pre-amplifier circuits in order to convert the collected currents from the 16 detector plates into output voltages. The integrating pre-amp circuit is based on the Burr-Brown ACF2101 Low-Noise, Dual Switched Integrator chip with an external integration capacitor. There are four pre-amp boxes mounted on the top of the detector, and each box contains two ACF2101 chips, processing four signals.

The computer controls the timing of the detector current integration with two incoming signals from a central pre-amp control box. This box serves to distribute the power and control signals to the four integrator boxes. The RESET signal shorts the charge collecting capacitors to drain the charge. The HOLD signal determines when charge is collected on the capacitors.

External capacitors are connected to the ACF2101 internal charge collection capacitor to optimize the output voltage. For maximum accuracy, the signal from the pre-amp should be in the upper range of operating voltage of the analog to digital converter (ADC), which accepts a maximum of 10 volts. For plates 1, 2, and 3, which collect charge from a current of about 30 nA per channel, 3.3 nF capacitors are used, and for plate 4, which collects charge of about 10 nA per channel, a 1.00 nF capacitor is used.

The voltage signal cables are routed from the apparatus on the beam line to the electronics rack behind the biological shield. A National Instruments PCI-6031E, 16-Bit, 64-Analog-Input Multifunction DAQ card connected via a National Instruments SH100100 Shielded Cable to a National Instruments SCB-100 Shielded Connector Block received the analog voltage signals. A Dell Dimension 8200 2.5GHz P4 computer with 512 MB of memory was used for data acquisition and experiment control. The computer program that controls the apparatus for the data acquisition sequence and signal processing is described in Section 7.4.

The computer controls the data acquisition sequence through digital output that is connected to an analog voltage and sent to the pre-amp control box. When data is not being collected, the control box keeps the RESET and HOLD signals at low voltage so that the capacitors are discharged. For increased accuracy in measuring the integrated detector current, the voltages in the integrating capacitors are recorded before and after the integration interval. This is carried out with a series of computer issued HOLD, RESET, and READ commands as depicted in Figure 5.17. The computer records the differences in capacitor voltages as an equivalent total collected charge for that particular state of the apparatus.

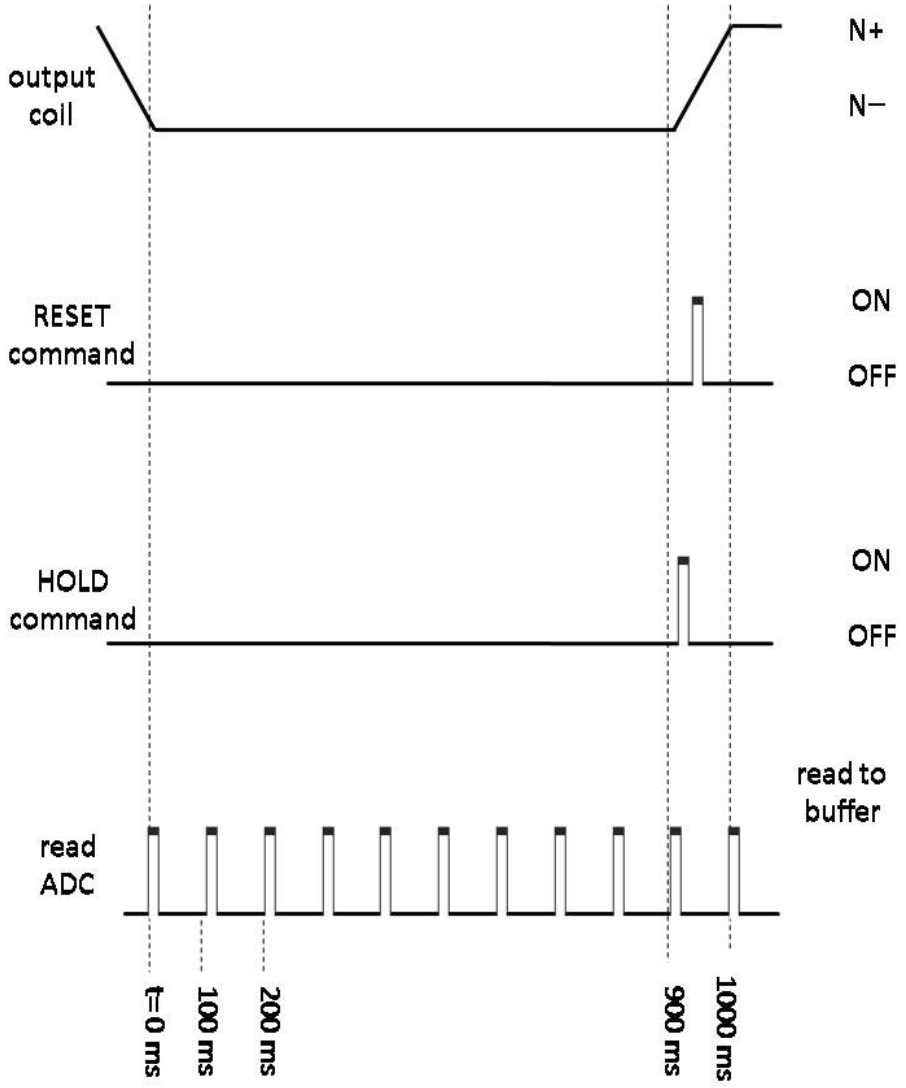

Figure 5.17: Diagram of timing and control of data acquisition sequence. RESET, HOLD and READ commands issues by the NSAC program run at the highest system priority with millisecond precision. Timing is synchronized to the hardware clocks on the DAQ board. Charge is determined by the difference between the $t = 0$ and $t = 900$ ms reads. After the ten read cycle sequence, a data point is generated and written to disk.

The detector and signal processing electronics were calibrated with a known current source. The calibrated current source was connected to each detector plate quadrant, and the collected charge was recorded as bits by the data acquisition program. The conversion of bits to nanoCoulombs was determined for each channel. The absolute calibration of each channel is not critical, since the spin-rotation measurements involve asymmetries, and thus ratios of collected charges. The detector channel assignments and calibration factors are presented in Table 5.1.

The computer program controlled the states of the apparatus through a sequence of digital signals and serial commands. Figure 5.18 shows the routing diagrams for these control signals. To control the stepping motor that rotates the pump, the computer issues serial commands to the Thermionics iSMC Stepper Motor Controller that controlled the Thermionics FRM-133-25 rotary motion feedthrough. The location of drainpipes was determined by the position of a pair of Thermionics FLML-133-25 pneumatic linear feedthroughs that controlled the strings. The air control valves for the actuators were opened or closed based on serial commands issued by the computer to an ADR 2205 relay board. The current regulated power supplies for the pi-coil, the output coil, and the trim coils, received computer-generated signals designating the sign and magnitude of the output current.

Table 5.1: Detector channel identification and calibration.

Channel	Plate	Detector Quadrant	Location	Pre-Amp Capacitor (uF)	Calibration: $\text{charge[nC]} = A * \text{bits} + B$	
					$A\ (\times 10^{-2})$	$B\ (\times 10^{-2})$
1	1	A	TOP/WEST	3.3	– 1.026	8.21
2	1	B	TOP/EAST	3.3	– 1.050	2.099
3	1	C	BOTTOM/EAST	3.3	– 1.050	0
4	1	D	BOTTOM/WEST	3.3	– 1.045	10.45
5	2	A	TOP/WEST	3.3	– 1.045	1.463
6	2	B	TOP/EAST	3.3	– 1.0395	– 7.275
7	2	C	BOTTOM/EAST	3.3	– 1.048	9.43
8	2	D	BOTTOM/WEST	3.3	– 1.043	11.47
9	3	A	TOP/WEST	3.3	– 1.048	9.43
10	3	B	TOP/EAST	3.3	– 1.041	11.45
11	3	C	BOTTOM/EAST	3.3	– 1.053	10.53
12	3	D	BOTTOM/WEST	3.3	– 1.043	10.43
13	4	A	TOP/WEST	1.0	– 0.3113	8.405
14	4	B	TOP/EAST	1.0	– 0.3064	10.11
15	4	C	BOTTOM/EAST	1.0	– 0.3136	11.29
16	4	D	BOTTOM/WEST	1.0	– 0.3033	10.62

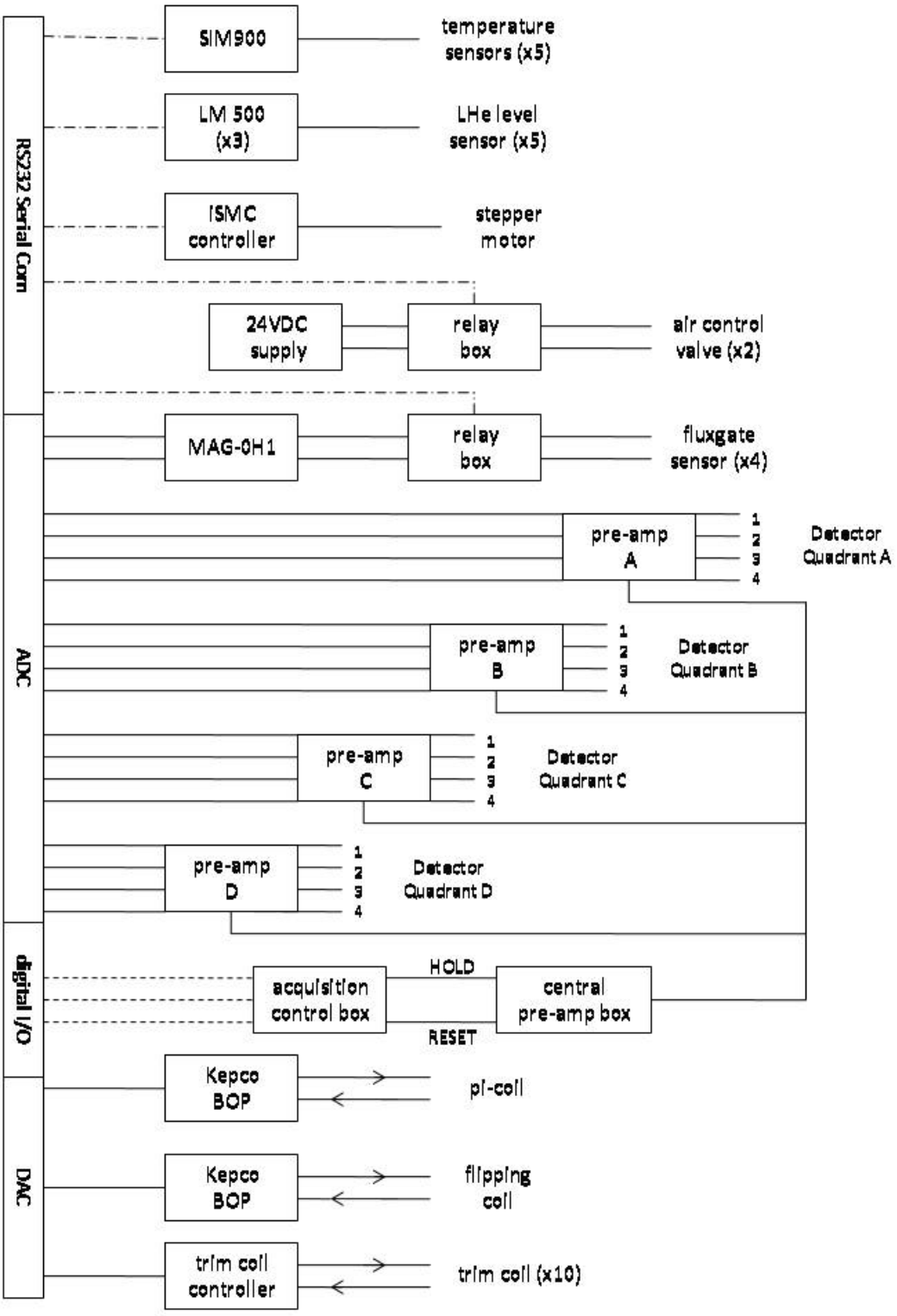

Figure 5.18: Signal processing and routing for the spin-rotation apparatus.

6 Liquid Helium Target

The target insert consists of two targets that are separated by the pi-coil (see Figure 6.1) and are enclosed within a cylindrical aluminum vacuum chamber, which isolates the target insert from the rest of the cryostat. A schematic of the target insert is shown in Figure 6.2. Each target is partitioned into separate left and right side chambers. These chambers are filled by a centrifugal pump from an 13 L liquid helium bath in the bottom of the vac-canister, and diagonal pairs of target chambers can be emptied using drainpipes. By alternately filling and draining diagonal pairs of target chambers, two target states are possible.

Two feedthrough tubes extend from the vac-canister to a room temperature motion control system that operates the pump and drainpipes. The volume of the liquid helium bath is maintained by a capillary impedance that connects the 4K-volume to the vac-canister.

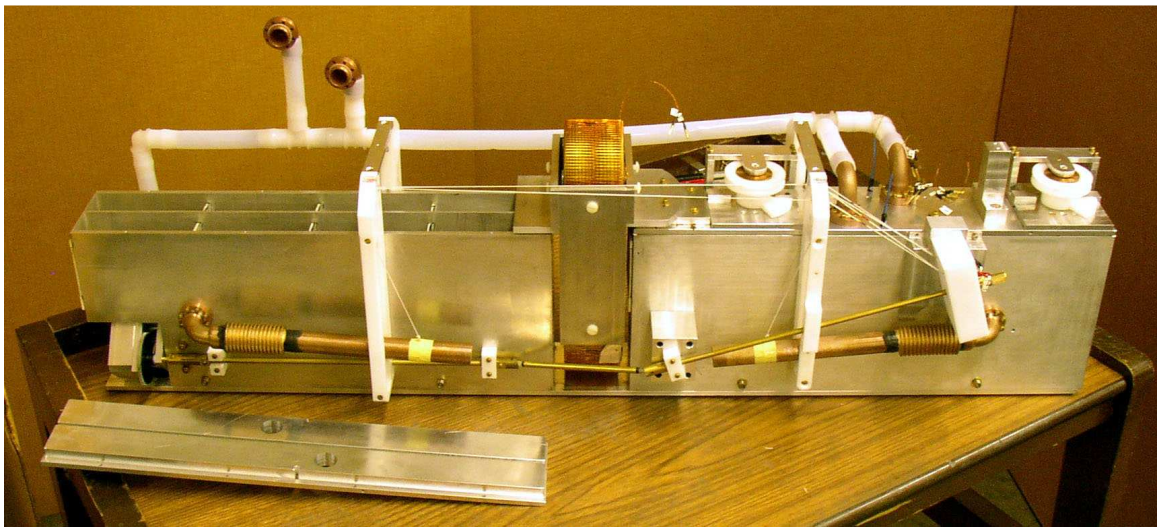

Figure 6.1: Photo of the liquid helium target. The upstream target is open to show left and right chambers and the collimation.

6.1 Constraints on liquid helium target design

Two mean free path lengths for neutrons passing through liquid helium determine the ideal thickness of the liquid helium target. For 5 Å neutrons at 4K, that length is about 1 m. That distance increases to 2 m for 7 Å neutrons. However, the 1 m length of the cold bore in the cryostat bounds the overall length of the target insert, which includes the vac-canister and any flanges on the end of the vac-canister. For ease of construction and optimal use of space, the target length is set to 42 cm.

The transverse dimensions for the target are set by the beam collimation at the exit of the supermirror polarizer, which is 45 mm tall by 55 mm wide. The inside dimensions of the target allow acceptance of as much of the beam as possible and allow room for internal collimation.

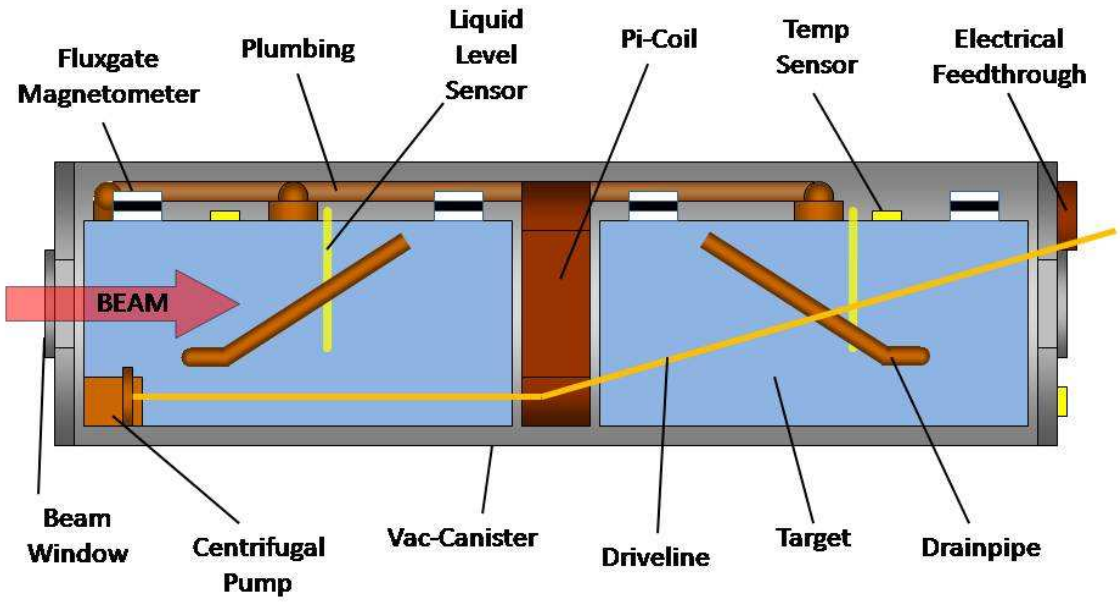

Figure 6.2: Diagram of the target insert (side view). The pi-coil is located between two targets that each have left and right target chambers. A pump and drain system fills and empties the target chambers with liquid helium from a bath at the bottom of the vac-canister.

A further constraint on the target is the need for no magnetic items to be inside the field-free target region. A limit of a 10 μG change in the residual field in the target region due to materials as measured 1 cm from a fluxgate magnetometer sensor was the restriction. This meant that only nonmagnetic materials were used, and that all hardware used on the target had to be checked for magnetic inclusions. This constraint also meant that the target required magnetic shielding from external fields. A 100 μG goal needs at least a 10^4 reduction for just the Earth's 0.5 G field, plus reduction of additional fields in the guide hall environment. This necessitates the use of passive mu-metal shielding, and active compensation coils to offset external time-dependent fields and to shape fields inside the target region. Magnetometry is needed to periodically sample the fields in the target region in order to control the compensation coils.

The polarimeter employs a target system that moves liquid forward and backwards of the pi-coil in order to measure asymmetries that are used to separate small parity-violating rotations from a larger parity-conserving signal. In order for this to work, only the position of the liquid helium should generate the parity-violating signal, and movement of the liquid should change the sign of the signal, but not the magnitude. Additionally, systematic effects due to the change in the beam spectrum because of target length differences should be small enough not affect the measurement of the parity-violating rotation. For a 10^{-6} rad/m measurement, this sets the length difference for all four target chambers to $\Delta L \leq \pm 0.01$ mm.

Since the density of liquid helium at 4.2K is 18% less than that of liquid helium at 2K [88], the capability to operate the target at different temperatures would provide a valuable check using essentially a longer target at 2K. At 2K, liquid helium becomes superfluid, so bubble formation and thermal gradients are suppressed. This allows for a check for scattering in liquid due to bubbles. Finally, the measured neutron small angle scattering cross section [72] in liquid helium increases by a factor of five from 4K to 2K (Figure 6.3). This allows another operational check of the system.

A final constraint on target design is the suppression of reflections from the walls of the target chambers. The critical glancing angle between helium and a chamber wall depends on the liquid or gas state of the helium as well as the temperature. These differences can cause systematic effects. The size and number of internal collimators in the target chambers should be sufficient to prevent reflections below a given neutron wavelength and is discussed in Section 6.4.2.

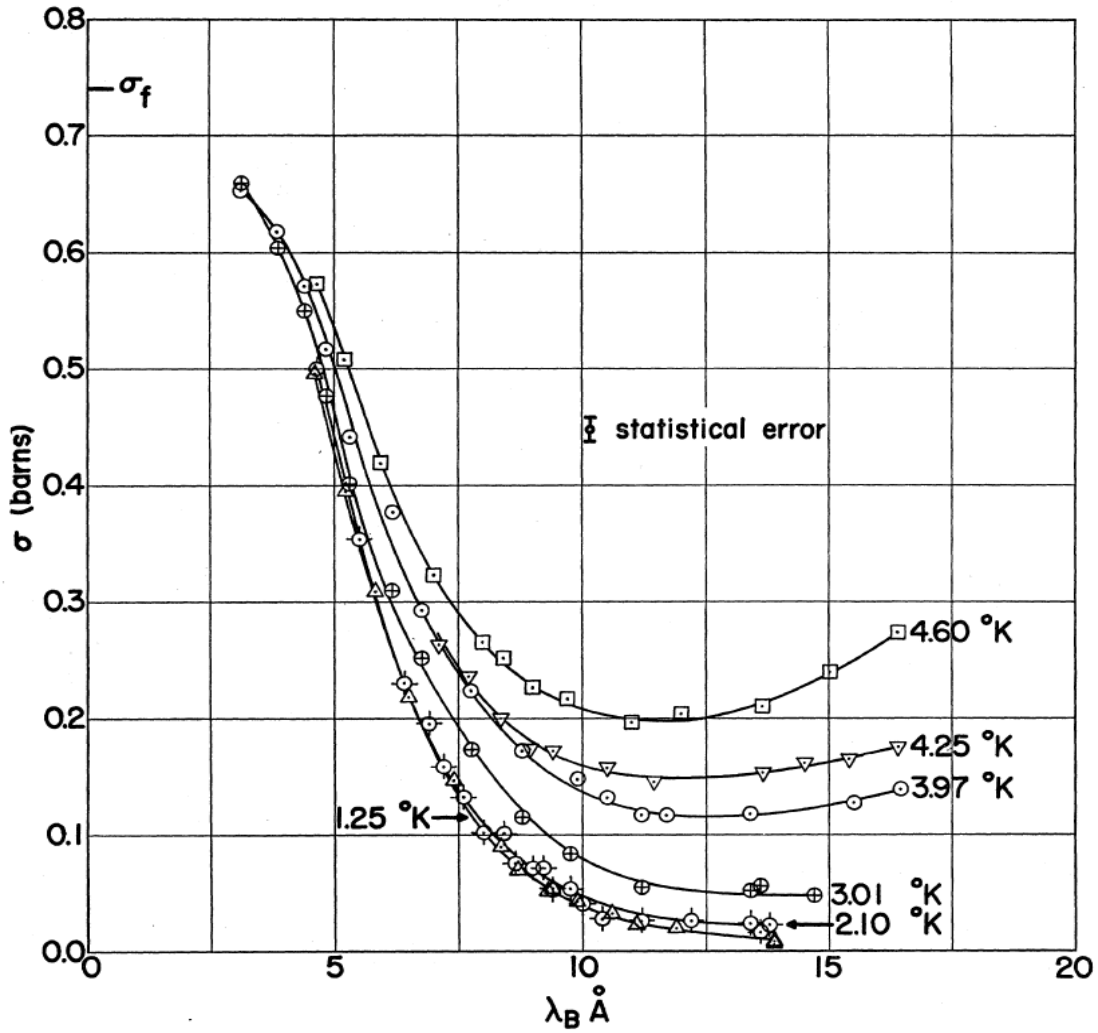

Figure 6.3: Plot of the measured neutron small angle scattering cross-section of liquid helium. σ_f is the measured neutron-^{4}He cross section for an isolated atom.

6.2 Cryostat

A horizontal bore, nonmagnetic cryostat was built by Oxford Instruments, Inc. This cryostat consists of two coaxial annular aluminum vessels housed within a cylindrical main vacuum vessel as shown in Figure 6.4. The outer 77K-volume can hold 50 L of liquid nitrogen and the inner 4K-volume can hold 30 L of liquid helium. The cylindrical interior surface of the 4K-volume forms the cold bore, which is 30.5 cm in diameter and 100 cm long. This cryostat has been repaired at IUCF by replacing the Viton o-rings with indium seals on the main vacuum for the liquid nitrogen and liquid helium fill stacks in order to fix leaks that developed during cryogenic operation. Stainless steel bellows on each fill stack have been replaced due to cryogenic leaks, and a fractured aluminum weld has been repaired on the 4K-volume.

The cryostat is supported within the outer two μ-metal magnetic shields with a set of four 2.5 cm diameter aluminum posts. These posts pass through small openings in the magnetic shielding in order to minimize the influence of external fields in the target region. An additional magnetic shield rests within the cold bore. This shield is constructed from Amuneal Cryoperm 10, which is a magnetic material that is engineered to possess a large magnetic permeability at low temperature. The target insert is positioned within the cryogenic magnetic shield inside the cold bore.

The measured hold time of the liquid helium volume in the cryostat is 30 hours, and the hold time of the liquid nitrogen volume is at least 50 hours.

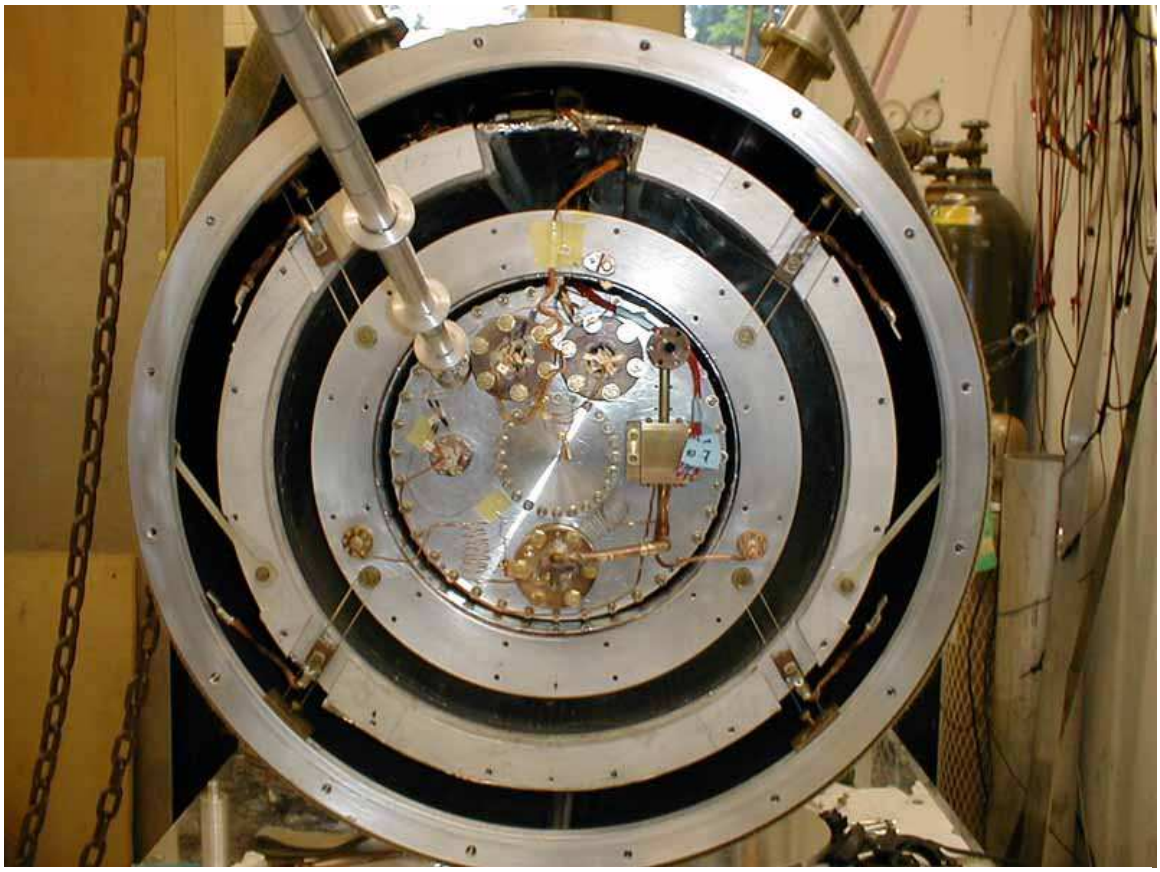

Figure 6.4: Photo of the interior of the cryostat with the target insert. The target insert rests within the 4K cold bore. Both the 4K-volume and the 77K-volumes are suspended within the cryostat by G10 straps. Cryogenic wiring is routed from the target insert to electrical feedthroughs at the top of the cryostat.

6.3 Target insert

The target is housed within a nonmagnetic vacuum chamber called the "vac-canister", which also contains the liquid helium bath that is used to fill the target chambers. The vac-canister rests on four 5.5 mm diameter silicon nitride ceramic balls that center the vac-canister within the diameter of the cryogenic magnetic shield. This prevents direct thermal contact between the vac-canister and the magnetic shielding, and thus between the target insert and the cold bore of the cryostat. The upstream end of the vac-canister is separated from the interior surface of the 4K thermal shield by a pair of #10-32 titanium bolts, which act as mechanical stops for the vac-canister inside the cryostat.

Motion-control and pump-out feedthroughs attach to the downstream end of the vac-canister and are thermally lagged to the 4K and 77K thermal shields in order to minimize the heat load on the target. An impedance built from a 50 cm length of 0.2 mm diameter cupronickel capillary tubing connects the liquid helium annular volume in the cryostat to the vac-canister. This impedance delivers a continual mass flow of liquid helium from the cryostat to the target insert to replace helium that has boiled off due to the heat load.

The vac-canister is a 95.3 cm long by 28.8 cm diameter aluminum cylinder with 26.7 cm inner diameter. Flanges at upstream and downstream ends are attached using indium seals and titanium hardware (see Figure 6.5). Both flanges have a centered 7.6 cm diameter hole for beam access, which are covered by a 0.8 mm thick machined-aluminum windows that are attached using indium seals and brass hardware. Aluminum Conflat half-nipples are welded onto the downstream flange to accept a pair of nonmagnetic electrical feedthroughs (70 mm), the motion-control feedthrough (34 mm), the pump-out feedthrough (34 mm), the capillary impedance (34 mm), and a spare access port (70 mm). All Conflat seals use nonmagnetic aluminum o-rings and brass hardware.

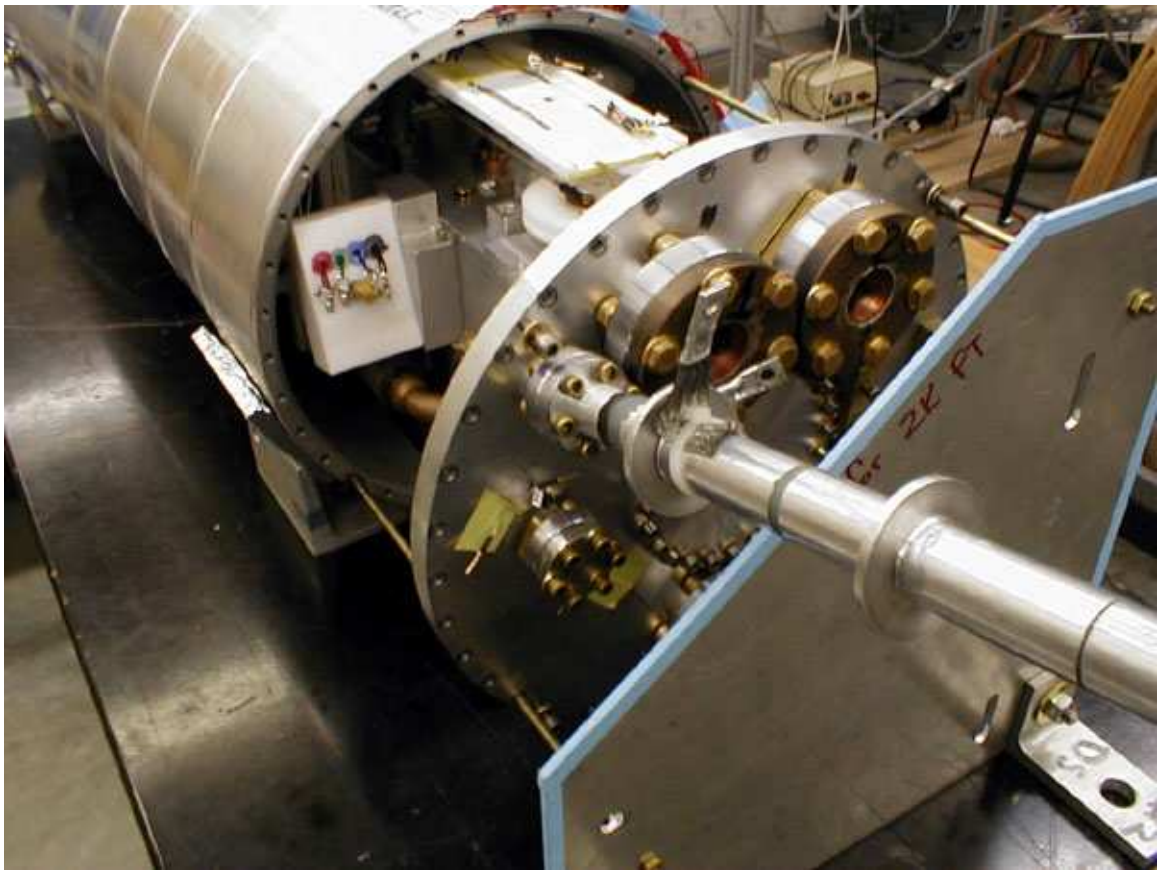

Figure 6.5: Photo of the assembly of the target insert. The downstream end of the target is shown being loaded into the vac-canister. The downstream vac-canister main flange is positioned for attachment of instrumentation wires into the two electrical feedthroughs (top center on flange) and strings and driveline connections into the motion control feedthrough (top left on flange).

6.3.1 Cryogenic refrigeration

During superfluid operation, an evaporative refrigerator system maintains the target temperature below the lambda transition temperature for liquid helium ($T_\lambda = 2.18$ K at saturated vapor pressure). An Alcatel RSV 601 B roots blower with an Alcatel 2033H ZM backing-pump pumps on the liquid helium bath inside the vac-canister to provide evaporative cooling. A Lake Shore Cryotronics 9005-001 vacuum regulator valve controls the conductance along the pumping line. Adjustment of the valve controls the vapor pressure above the helium bath and regulates the temperature of the target. For an operational temperature of 2K, the pressure in the vac-canister is maintained at 25 Torr.

As helium vapor is pumped out of the vac-canister, some of the liquid helium in the bath boils off, thus lowering the temperature of the remaining bath. This evaporative cooling continues at a rate sufficient to equilibrate the saturated vapor pressure for the bath temperature. The roots blower removes helium from the vac-canister, maintaining the desired temperature and so reducing the amount of liquid helium in the vac-canister.

Capillary tubing connects the 4K-volume in the cryostat to the vac-canister, allowing liquid helium from the cryostat to refill the vac-canister continuously. The diameter and length of the capillary as well as the pressure difference between its ends determine the impedance of the tube, which determines the rate of mass flow of helium into the vac-canister. However, a well-chosen length and diameter of capillary creates an impedance sufficient to enthalpically lower the temperature of liquid helium flowing through it. Pobell [89] and Richardson [90] describe the theory and design of evaporative refrigerators that employ such capillary impedances (known in low-temperature physics as a "1K-pot").

The amount of helium pumped from the vac-canister depends on the heat load and desired temperature of the target insert. The choice of impedance should match the mass flow of helium into the vac-canister to match the amount of helium pumped from the vac-canister. If the amount of impedance of the capillary is too large, insufficient helium will

flow into the vac-canister and the liquid helium bath will run dry. Conversely, if the amount of impedance is too small, an excess of helium will flow into the vac-canister and the liquid level of the bath will rise into the beam path.

To prevent the level of the liquid helium bath from rising into the beam path, an extension tube was glued into the pump-out feedthrough flange and directed down into the vac-canister. The lower end of this tube was positioned just below the lower edge of the beam window on the vac-canister main flange. When the liquid level rises into the beam path, it also rises above the end of the extension tube, so the roots blower then pumps on the liquid helium bath instead of the vapor above the bath, and quickly removes excess liquid helium from the vac-canister.

Furthermore, the rate of mass flow along the impedance is a function of the pressure difference between the vac-canister and the 4K-volume. Normally, the roots blower determined the pressure in the vac-canister, but over- or under-pressure on the 4K-volume in the cryostat can fine tune the pressure difference to achieve the desired liquid helium bath level is achieved. Measurements from the liquid level sensors mounted in the vac-canister can verify the level of the liquid helium bath. Additional level information can be provided by neutron data from the ion chamber, which indicates if the bath level goes above the beam path (a uniform decrease in beam intensity) or when there is insufficient liquid to fill the target chambers in a nominal length of time (an increase in beam intensity).

6.3.2 Nonmagnetic electrical feedthroughs

A demountable, nonmagnetic multipin electrical feedthrough was developed for use at low temperatures in the neutron spin-rotation experiment in order to bring electrical leads out of the vac-canister. The feedthrough was required to maintain vacuum outside of the vac-canister filled with superfluid helium. Because of the stringent magnetic field strength constraints in the target regions ($B < 100\ \mu G$), all materials must be nonmagnetic. Commercially available electrical feedthroughs were unsuitable due to the

presence of stainless steel or nickel, so custom-built feedthroughs were made by embedding brass pins in epoxy resin, based on an epoxy-to-copper seal design by Wheatley [91].

The feedthrough is built around a 70 mm CF flange machined from beryllium copper and has a 25.4 mm diameter bore. An OFHC copper tube with 1.0 mm wall thickness is inserted through the bore and hard-soldered flush to the outer face of the flange. The other end of the copper tube extends 20 mm past the knife-edge face of the flange and tapers to 0.1 mm wall thickness. The free end of the copper tube is potted within a plug of Stycast 2850FT epoxy resin that is room temperature cured with No. 9 catalyst. The Stycast plug also encases 30 brass 1.0 mm diameter pins arranged in a pattern of three concentric rings that optimize the spacing between pins. These pins extend 12.5 mm beyond both the front and back faces of the Stycast plug (see Figure 6.6).

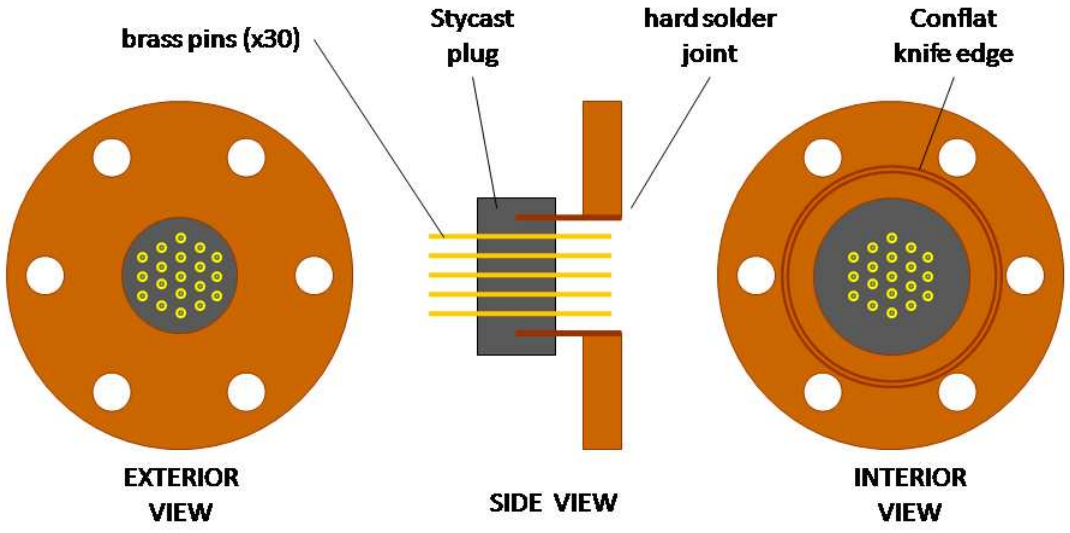

Figure 6.6: Diagram of the demountable, nonmagnetic electrical feedthrough.

The hard-solder joint on the outer flange face and the tapering of the copper tube wall are necessary to allow for differential thermal contraction during thermal cycling between the beryllium copper, OFHC copper, and epoxy resin.

A casting master was constructed from machined aluminum that had a set of predrilled holes to accept a pattern of brass pins. A mold was made of the master using Micro Mark 10:1 High Tear Strength RTV rubber. The flange assembly and brass pins were loaded into the mold, and epoxy resin was poured into the mold to as preset level, thus potting the pins and the tapered end of the copper tube.

After numerous thermal cycles between room temperature and liquid helium, and several thermal shock tests in liquid nitrogen, no leaks have been observed in the three feedthroughs that were built.

6.3.3 Motion control system

The target insert was connected to the motion control system and roots blower through two feedthrough tubes that penetrate the magnetic shielding. As seen in Figure 6.7, each tube was fashioned from a 19 mm diameter by 0.8 mm wall by 100 cm long section of G10 tube. G10 was chosen for its mechanical strength and low thermal conductivity. An aluminum 34 mm CF half-nipple flange was glued into one end of each tube with Stycast 2850 FT epoxy resin. A stainless steel bellows assembly was glued into the other end. The exterior of the exposed bellows has a stainless steel collar welded around it for use as an indium seal surface. To ensure that the tube did not develop leaks as well as to block light transmission through the G10 (which would introduce heat into the target), a thin coating of epoxy resin was applied over the outer surface of the G10, and the glue joints between the G10 and the metal flanges on each end were strengthened with filets.

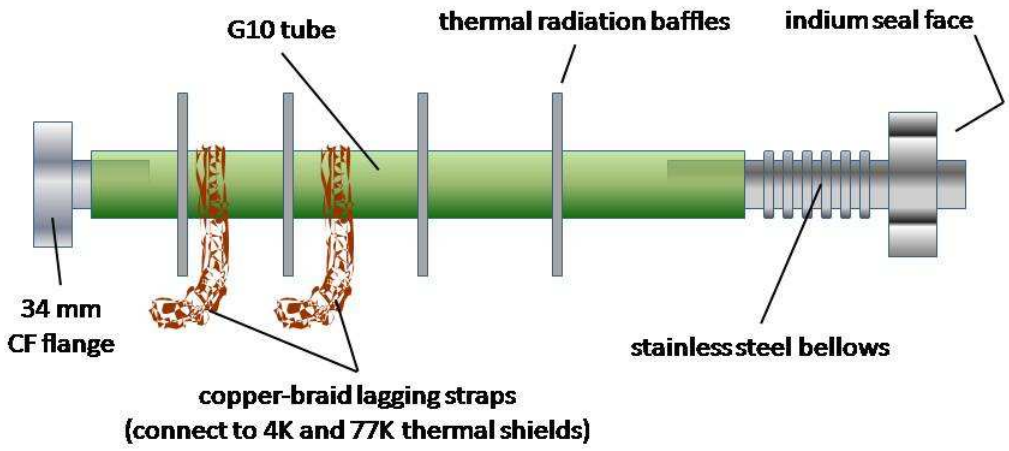

Figure 6.7: Diagram of the motion-control and pump-out feedthrough tubes. The motion-control feedthrough has an additional assembly for guiding string and pump driveshaft motion (not shown).

A pair of 50 mm diameter aluminum pipes attaches to the downstream face of the cryostat with KF-flanges and surround each feedthrough tube with a vacuum jacket. The other end of the aluminum pipe inserts into a motion control box via a fluorosilicone compression o-ring seal. This type of o-ring material remains plastic through a wider range of temperatures than typical silicone or fluorocarbon o-rings. This is important since the motion control boxes – and by thermal contact, the compression o-ring seals – get very cold during liquid helium transfers to the target insert because of the cold helium exhaust gas. However, even fluorosilicone can become too cold to remain plastic enough to hold a vacuum seal, so heater tape is used to keep the o-ring seal intact during liquid helium transfers.

In order to suppress 300K thermal radiation from being incident on the vac-canister face through openings in the thermal shielding, a set of three baffles is glued around each tube. Copper-braid thermal lag-straps are connected between each tube and the 77K and the 4K heat shields to suppress the heat conduction along each tube into the target insert.

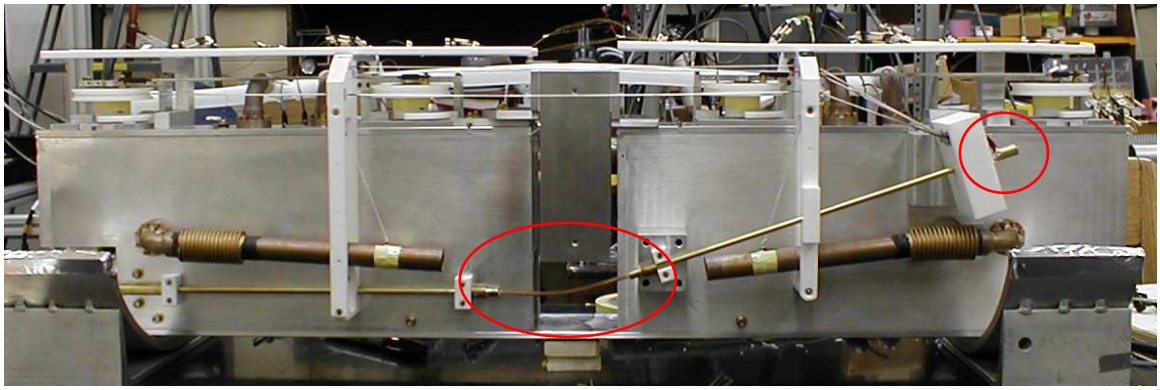

Figure 6.8: Photo showing the centrifugal pump driveline. The driveshaft within the motion-control feedthrough transmits torque from the stepper motor to a pump driveline via a brass quick-disconnect coupling. The driveline bends through a copper braided-rope flexi-shaft and couples to the centrifugal liquid helium pump (not shown). The driveline is supported by Teflon guides attached to the target.

The pump-out feedthrough has an internal set of baffles to suppress 300K thermal radiation from being incident directly into the target. The motion control feedthrough contains a subassembly that consists of four small diameter carbon-fiber tubes that sheath the control strings. These carbon-fiber tubes were glued into a set of baffles, which have a additional guide hole for the driveshaft. This subassembly was glued to the end of the 34 mm CF flange, but not along the rest of its length, so that the subassembly can move within the G10 tube during cool down. At the end of this feedthrough is a Teflon plug that has access holes drilled through for strings and the driveshaft. The plug is held in place by the flared ends of an auxiliary liquid helium transfer tube (a 6.3 mm diameter G10 tube with brass tubes glued on each end).

The stringent magnetic requirements of the target system require a novel method of changing target states – namely, a method to fill and drain diagonal pairs of target chambers without changing the magnetic fields inside the target region. This is accomplished with the use of a centrifugal pump that is immersed in the liquid helium bath at the bottom of the vac-canister and a set of flexible drainpipes that connect to the

bottom of each target chamber. Teflon tube plumbing connects the centrifugal pump to the tops of the target chambers.

Within the vac-canister, the centrifugal pump connects to a driveline that is comprised of sections of 4.8 mm diameter brass rod, a copper flexi-shaft, and brass couplings as shown in Figure 6.8. This driveline couples to a carbon fiber driveshaft in the motion control feedthrough. The other end of the driveshaft extends into the motion control box and couples to a Thermionics iSMC stepper motor with FRM-133-25 rotary motion feedthrough via a stainless steel double universal joint.

6.4 Target design

The liquid helium target is built from completely nonmagnetic materials, and all components are measured to produce changes in the ambient magnetic field of less than 10 μG when moved past a fluxgate magnetometer sensor at 1 cm distance. This includes the targets and lids, all hardware, Stycast 2850 FT epoxy resin with No. 9 and No. 23 LV catalysts, indium and Gore-Tex (expanded PTFE cord) seals, ^{6}Li-plastic collimators, all components of the centrifugal pump, plumbing, and drain system, the pi-coil, instrumentation and cryogenic wiring, the ice-getters, and the vac-canister and its fittings. Numerous pieces of hardware were rejected due to magnetic inclusions or surface contamination from magnetic tooling residues.

The targets were milled and finished from solid stock aluminum with a wire EDM machine at the University of Washington. Aluminum was chosen as the target material since it is nonmagnetic, possesses a high thermal conductivity, and has a low neutron scattering and absorption cross section. Each target has two side-by-side isolated target chambers that are 417 mm long by 33.5 mm wide by 60 mm tall and are separated by a 3 mm thick septum. The difference in target length for all four target chambers was measured as less than 0.01 mm. This is important for the suppression of systematic errors from neutron spectrum shifts as described in Section 4.2.3. A photo of the liquid helium target is shown in Figure 6.9.

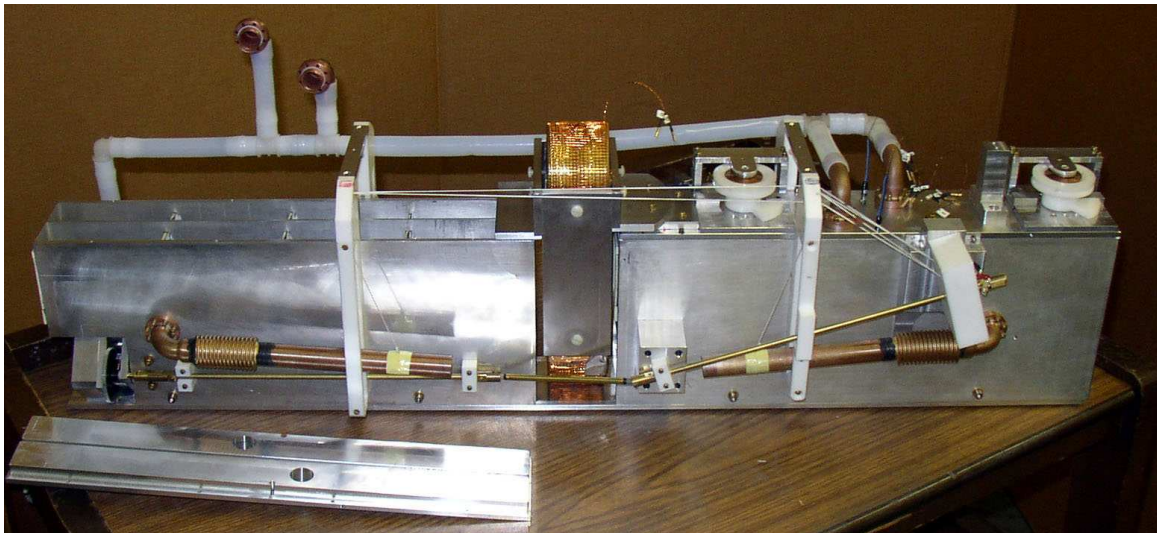

Figure 6.9: Photo of the liquid helium target. The pi-coil is located between the targets. The centrifugal pump driveline is in front of the target and connects to the pump on the lower left side of the photo. Plumbing is located on top and behind the target. Magnetometers are shown on top of the right target lid.

6.4.1 Pi-coil

Located between the targets, the pi-coil consists of a pair of side-by-side 16 cm tall by 4 cm by 4 cm square cross-section solenoids (see Figure 6.10). A pair of curved solenoids provide flux return on the top and bottom. Each solenoid has an aluminum core that is wrapped with three layers of 28 gauge polyurethane-insulated copper magnet wire with a winding density of 10 wires per cm per layer.

Designed and built at the University of Washington [34], the pi-coil generates an internal field that precesses the transverse component of neutron spin by π radians about the vertical axis ($+\hat{x}$-direction). A Kepco BOP 20-5M bipolar power supply provides the current for the pi-coil.

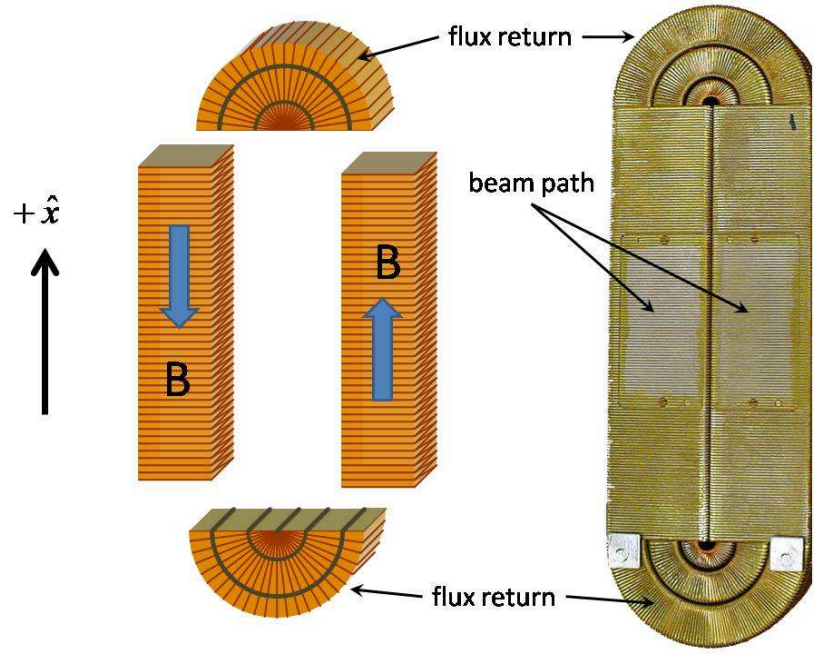

Figure 6.10: Diagram and photo of the pi-coil. The coil is wound so that left and right solenoids produce vertical magnetic fields through the region of the passing neutron beam. These fields are oriented opposite to each other, and curved solenoid sections on top and bottom provide flux return for both coils. A face-view photo of the pi-coil is shown on the right.

6.4.2 Neutron beam collimation

It is necessary to prevent neutrons reflecting from the inside surfaces of the target chambers in order to suppress possible target-dependent systematic effects, since the critical angle for reflection between aluminum and helium changes significantly for a liquid helium—aluminum interface and a ^{4}He-gas—aluminum interface. This phenomenon leads to a different set of neutron trajectories getting to the ion chamber in a target-dependent manner. Furthermore, the material density for helium and aluminum is temperature-dependent as well, leading to additional differences between critical angles at the helium / aluminum interface (see Table 6.1).

θ_C (mrad/Å)	4K	2K
liquid helium	0.679	0.654
helium gas (saturated vapor pressure)	0.798	0.808

Table 6.1: Critical angles between aluminum 6061 and helium interface at 4K and 2K.

Inside of each target chamber, three collimators prevent neutrons from reflecting off the chamber walls and reaching the detector. Collimators are positioned at ¼, ½, and ¾ of the target chamber length. Each collimator is 5 mm wide along the top, bottom, and outer chamber walls, and 2 mm wide along the chamber septum, thus defining a beam within a target chamber that is 26.5 mm wide and 50 mm tall. The geometry and spacing of the collimators is sufficient to prevent 20 Å neutrons coming from the guide from reflecting off target walls (Figure 6.11). The collimators are built from a lithium loaded polymer matrix material (manufactured by Ingenieurburo Stronciwilk, Berlin, Germany), which is attached to an aluminum backing with Emerson & Cumin Stycast 2850FT and cured at room temperature with catalyst 23LV. This material has a 90% enrichment of ^{6}LiF with typical loading of ~70% LiF by weight; a coefficient of linear absorption of 28.5 cm^{-1} for 1.8 Å neutrons; and a γ-production of 0.0003 photons / neutron for 2.3 Å neutrons. Additionally, ^{6}LiF collimators glued on the upstream face of each target define the left side and right side neutron beam with the same collimation as the inside of the target chambers.

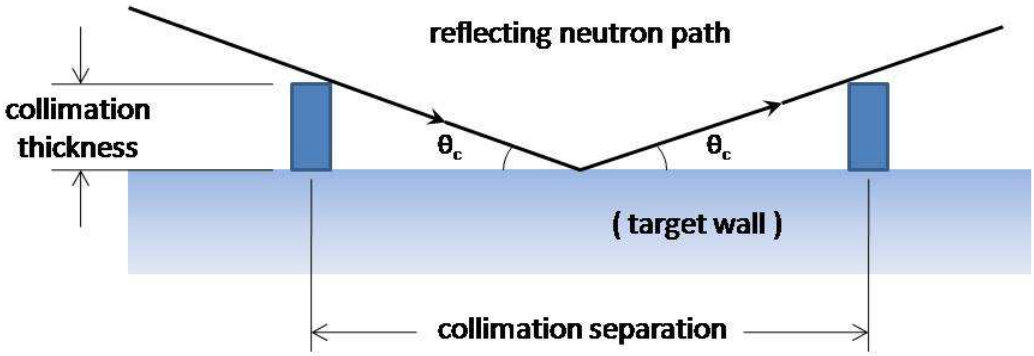

$$\text{separation} = 2\frac{(\text{thickness})}{\tan(\theta_c \cdot \lambda)}$$

Figure 6.11: Diagram of the target collimation geometry.

6.4.3 Instrumentation

In order to monitor the liquid levels in the bath and in each of the target chambers, five Cryomagnetics 2D resistive-wire liquid level sensors and three Cryomagnetics LM-500 cryogenic liquid level monitors are used. Each sensor requires 70 mA of current to operate plus a brief burst of higher current to initially de-ice the sensor. Since this generates undesired magnetic fields in the target chambers, the level sensors remain inactive during data collection times.

Scientific Instruments Si410 silicon diode temperature sensors were installed on the lids of both targets, the downstream face of the vac-canister, and the liquid helium and liquid nitrogen jackets within the cryostat. These sensors require an excitation current of 10 μA and are deactivated during data collection.

A Bartington Mag-01H single axis fluxgate magnetometer was multiplexed to four low-temperature Mag type-F probes. These fluxgate sensors were mounted above the targets as shown in Figure 6.12. Each sensor requires 10 mA of excitation current (26 mW of excitation power) to operate.

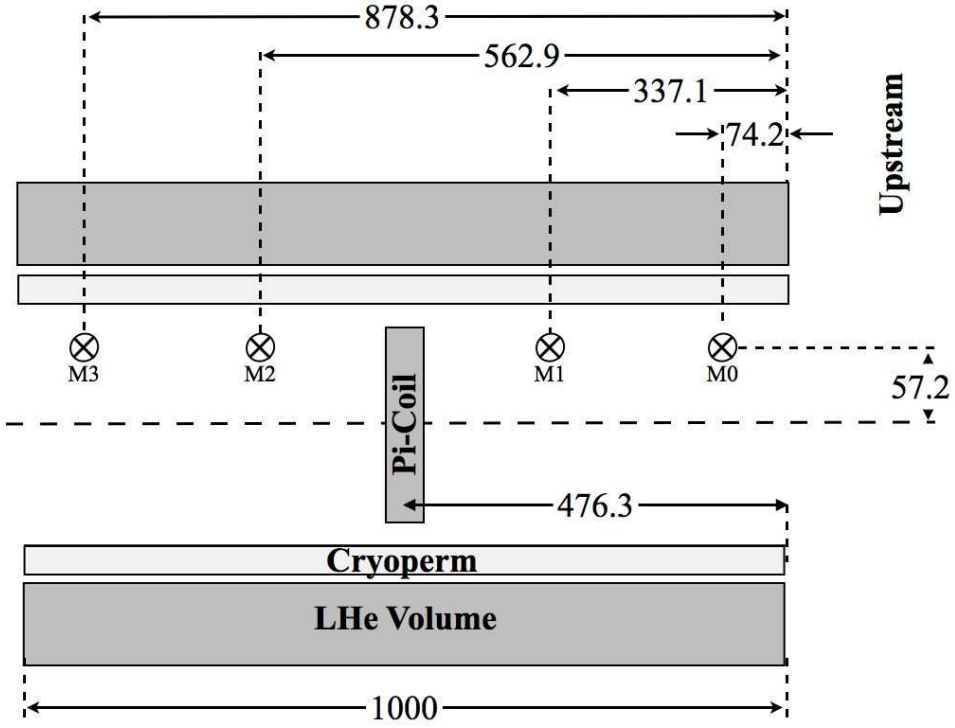

Figure 6.12: Diagram of positions of magnetometer sensors in the target region (side view cross section through cryostat cold bore); all measurements in mm.

6.4.4 Pyroelectric ice collectors

The centrifugal pump has gears and other moving parts that can be jammed by solid impurities in the liquid helium. It is known that liquid helium from a typical research dewar often has embedded ice crystals. Water ice and liquid air may also be accidentally introduced into the target system during liquid helium transfers. One method of

protecting the centrifugal pump from ice is by attracting it to a pyroelectric object. Usually, pyroelectric materials become polarized during temperature changes, which produce a strong electric field at each end of the polarized crystal. These materials become electrically neutral once the temperature is constant. However, cesium nitrate belongs to a subclass of materials that spontaneously polarize at cryogenic temperatures and remain polarized at constant temperature in a cryogenic environment [92]. Cesium nitrate powder was mixed in a 2:1 ratio with BJB type TC-854 urethane resin, cast into 75 mm diameter by 5 mm thick discs, and allowed to cure at room temperature for 24 hours. A hole was drilled through the center of each disc. One disc was bolted onto the lower section of each target so that it would be immersed in the liquid helium.

6.4.5 Liquid helium pump and drain system

The throughput of the centrifugal liquid helium pump is a function of the impellor speed. The pump has a 4:1 gear ratio. A limiting factor of pump speed is the 300 RPM maximum rotational speed of the stepper motor feedthrough. That sets the max pump speed at 20 Hz. During calibration cooling tests, the stepper motor was run at 30 RPM, and the pump was able to simultaneously fill all four target chambers in less than two minutes. However, pump performance decreased as the level of liquid helium in the vac-canister dropped. It was surmised that when the liquid helium level dropped below the pump inlet holes, the impellor was not completely immersed in liquid, thus reducing the throughput of the pump. A snorkel plate was installed over the pump inlet holes, which effectively lowered the pump inlet by approximately 3 cm. Target fill times confirm that installation of the snorkel increased the range of liquid levels in which the pump could effectively operate. This implies that longer data runs are possible before refilling the target insert is necessary.

The target chambers are emptied by drainpipes that are raised or lowered by 50 lb. test braided polyester strings. The strings are routed through the target and into the motion control feedthrough; from there, the strings enter the motion control box and

connect onto the ends of a pair of Thermionics FLML-133-25 pneumatic linear feedthroughs. The drainpipes are raised and lowered in pairs – diagonal pairs of target chambers. The ends of each drainpipe have a small brass collar glued inside; the ID of these collars are tapered to a knife edge in order to suppress superfluid film creep. The target chambers can be completely drained in less than one minute.

Sections of Teflon tube that connect to the top of each target chamber have a small hole drilled into the top surface to prevent vapor lock during filling and draining. The strings are routed along the target with Teflon guide blocks that have through holes in them.

During target filling, it was observed that running the stepper motor at the maximum rate of 300 RPM would stall the motor or seize the pump driveshaft. A safe speed of 120 RPM was demonstrated to not stall or seize the system. This motor speed was set for the target operation during the January 2008 reactor cycle.

6.5 Heat load estimates on the insert

During operation, the target insert is subject to a heat load from the outside environment as well as from the warmer parts of the cryostat. This heat load primarily affects the temperature of the liquid helium inside the vac-canister and rate of helium boil off. The impedance is designed to continually refill the vac-canister with enough liquid helium to replace the boil-off. This requirement of keeping a stable level of liquid helium in the target is necessary for switching target states in a timely manner. Additionally, the size of the heat load on the target system is designed to be small, so that the rate of boil for the liquid helium is small. However, even with construction materials and methods designed to minimize the heat load to the target, some small amount of heat does transfer to the target insert.

There are two states of target operation: one with normal liquid helium at 4.2K, and one with superfluid helium at approximately 2K. The following heat load estimate is for

the 4.2K target temperature (see Table 6.2), with a brief discussion of heat load corrections during superfluid operation.

The steady-state heat conduction $\dot{Q}$ through a material between temperatures T_1 and T_2 is given by

$$\dot{Q} = (A/L) \int_{T_1}^{T_2} \kappa \, dT \tag{6.1}$$

with cross-section area A, length L, and thermal conductivity κ. Assuming the vac-canister is thermalized to 4.2K due to the liquid helium bath inside it, then those objects that connect the vac-canister to a warmer surface conduct heat into the target insert. These include the motion-control and pump-out feedthroughs, and the cryogenic wiring.

Both feedthroughs are constructed from a 100 cm long by 19 mm diameter by 0.8 mm wall thickness section of G10 tube that is coated with a 0.4 mm thick layer of Stycast 2850 FT epoxy. With one end anchored at 300K, each feedthrough delivers 14.2 mW of heat into the target. The motion-control feedthrough has an extra assembly within it, which is comprised of four carbon fiber string sheaths ($100\ \text{cm long} \times 3.2\ \text{mm OD} \times 1.8\ \text{mm ID}$), two braided polyester motion-control strings ($100\ \text{cm long} \times 1.6\ \text{mm}^2$), an auxiliary liquid helium transfer tube made from carbon fiber and G10 tube ($100\ \text{cm long} \times 6.4\ \text{mm OD} \times 5.0\ \text{mm ID}$), and a carbon fiber pump driveshaft ($100\ \text{cm long} \times 4.8\ \text{mm diameter}$). This subassembly adds another 5.3 mW to the heat load. Both feedthroughs have a static column of helium gas within it that conducts 8.4 mW to the target from room temperature.

The cryogenic wires are also a source of heat conduction. There are approximately 60 36-AWG twisted-pair phosphor bronze wires with polyimide insulation and 22 26-AWG twisted-pair OFHC copper wires with Kynar (PVDF) insulation that extend between the room-temperature electrical feedthroughs and the target insert. However, these wires are thermally lagged around a cold finger that is attached to the liquid nitrogen annular volume within the cryostat. From this 77K anchor, the wires extend ~50

cm to the target insert and deliver ~16 mW of heat to the target insert, with the OFHC wires conducting nearly 15 mW of the total.

Current passing through the trim coil loops that are wound around the vac-canister and the degaussing coil (which does not directly contact the target insert) produces heat due to ohmic resistance. For the trim coils, the heat generated during operation is negligible due to the small currents involved (10's of μA) and small resistance for OFHC wire at liquid helium temps (< 1Ω). In contrast, the heat generated during degaussing of the cryogenic magnetic shield is substantial (up to 5 A), and this heats both the liquid helium annular volume and the magnetic shielding. An accidental touch contact between the degaussing coil and the vac-canister would cause local heating of the vac-canister. However, since degaussing happens infrequently (once every few days) and occurs between data runs, the time-averaged heat load is small.

The heat load from instrumentation within the target is large though. In order to minimize heat generated within the target, their operation is restricted to only those times when sensor information is necessary. In practice, this means that sensors are sequentially energized during target maintenance cycles and deactivated prior to the next data cycle. This has the added benefit of eliminating residual magnetic fields within the target regions that are generated from current-carrying sensor leads. The following sensor heat estimates are based on an activation time of 30 seconds on for every ten minutes of data-taking (power off).

The target has five resistive liquid helium level sensors that each have a resistance of 27.3 Ω and require an excitation current of 70 mA, which generate 33.4 mW. The three silicon diode temperature sensors each have a resistance of 4.5 Ω and require an excitation current of 10 μA, which generate 0.07 nW. The four fluxgate magnetometer sensors each have a resistance of 20 Ω and require an excitation current of 10 mA, which deliver 0.4 mW of heat.

Another source of introduced heat in the target is the pi-coil. The measured resistance at cryogenic temperatures is 2 Ω, and the current supplied to the pi-coil is 150 mA. However, the pi-coil is energized only 2/3 of the time. Thus the time-averaged generated heat due to the pi-coil is 35 mW.

Finally, the centrifugal liquid helium pump introduces heat into the liquid helium bath from mechanical efficiency losses during operation. Pump designs similar to the one used for this experiment have been characterized by the Cryogenics Division of the National Bureau of Standards [93] with typical efficiencies in the 10% to 15% range for optimal pump speeds. Based on review data for liquid helium centrifugal pumps with a non-optimized impellor design and low pumping speed, an estimated efficiency of 1% for the pump used in this experiment seems reasonable. For a crude estimate of the delivered heat by the pump into the liquid bath, consider that the pump can fill all four target chambers (840 cm^2) in about two minutes from a liquid helium bath about 10 cm below the target chambers. This requires about 0.85 mW of power. A 1% efficiency implies that the pump generates 85 mW of heat. If the pump operates for two minutes out of every 13 minutes (one minute drain time, then 10 minutes for data-taking), then the time-averaged heat load is 13 mW.

Thus, the total heat load for the normal liquid helium target (4.2K) is 153.3 mW. When the target is run in superfluid helium mode, the effects of the temperature difference between the cold bore and the vac-canister must now be included in the estimate.

To begin, the heat load $\dot{Q}$ on a surface at temperature T_1 due to a radiative surface at T_2 is given by:

$$\dot{Q} = \alpha \, \sigma \, A \left({T_2}^4 - {T_1}^4 \right) \tag{6.2}$$

with surface absorptivity α, Stefan-Boltzmann constant σ, and area A. The vac-canister surface is a 95.3 cm long by 28.8 cm diameter cylinder that has almost 4π coverage by a 4.2K surface, thus the radiative heat load is 1.3 μW.

Differences in conductive heat transfer from 300K or 77K and the 2K target insert are negligible compared to the 4.2K case. However, in order to keep the target at 2K, the roots blower must pump on the liquid helium bath to maintain a helium vapor pressure of ~25 Torr. This means that there is no static column of helium gas in the pump-out feedthrough that can transfer heat to the target insert. The mass flow of helium pumped out of the target is replaced from the liquid helium annular volume in the cryostat through the impedance. The dimensions and pressure gradient on each side of the capillary generate sufficient impedance to lower the temperature of the liquid helium from 4.2K to 2K, so that no heat is transferred via the column of liquid helium (see Pobell [89]), but the 0.2 mm diameter by 50 cm long piece of cupronickel capillary conducts 0.13 mW to the vac-canister.

The vac-canister is mounted within the cold bore of the cryostat, but is physically separated from the cold bore by a set of four silicon nitride ceramic balls that allow 1.5 mW of heat flow. A pair of titanium #10-32 bolts space the upstream face of the vac-canister from the 4K-thermal shield. These bolts deliver 7 μW of heat to the target insert. Finally, the heat load due to conduction through the residual gas in vacuum between the vac-canister and the surrounding 4K-surface can be approximated by:

$$\dot{Q} = A\,\kappa\,P\,(T_2 - T_1)/T_{AVG}{}^{\frac{1}{2}} \tag{6.3}$$

with area A, thermal conductivity κ, pressure P, and temperatures T_1, T_2. Due to cryopumping on both surfaces, helium is the residual gas in vacuum governing the heat-flow. For a 10^{-3} Torr cryostat main vacuum pressure, the heat load on the target insert is 7 mW.

In summary, the combined heat load during superfluid operation is 153.5 mW.

Table 6.2: Heat load estimates for the liquid helium target.

(heat given in mW)	*Normal Operation (4.2K)*	*Superfluid Operation (2K)*
Radiative cooling between cold bore and vac-can	**--**	**0.0013**
Conduction through residual gas at 10^{-3} Torr	**--**	**7**
Conduction along ceramic spacers	**--**	**1.5**
Conduction along titanium vac-can stops	**--**	**0.007**
Conduction along 2K-feedthrough		
G10 tube	*4.7*	*4.7*
Stycast layer	*9.5*	*9.5*
Helium-gas	*8.4*	*8.4*
Carbon fiber tubes	*3.5*	*3.5*
Polyester strings	*0.05*	*0.05*
Centrifugal pump driveshaft	*1.8*	*1.8*
2K-feedthrough subtotal	**27.9**	**27.9**
Conduction along 4K-feedthrough		
G10 tube	*4.7*	*4.7*
Stycast coating	*9.5*	*9.5*
Helium-gas	*8.4*	--
4K-feedthrough subtotal	**22.6**	**14.2**
Conduction along impedance	**--**	**0.13**
Conduction along wires	**15**	**15**
Introduced heat from the pi-coil	**35**	**35**
Introduced heat from sensors	**33.8**	**33.8**
Introduced heat from centrifugal pump operation	**13**	**13**
Total	**147.3**	**147.5**

7 Data Acquisition

Assembly of the spin-rotation apparatus on the NG6 beam line at the NCNR at NIST began in February 2006. Calibration and commissioning of the neutron polarimeter took place during 10 reactor cycles over 21 months. During this time, the neutron beam was characterized, the polarimeter was set up, the data acquisition program was debugged, instrumentation brought online, and motion control established. Additionally, data for room-temperature targets was taken in order to characterize possible systematic effects. Beginning with the January 2008 reactor cycle, data for the liquid helium target spin-rotation measurement was taken.

7.1 Characterization of the neutron beam

An extensive series of characterization measurements were conducted on the apparatus components that were assembled and tested at Indiana University, including the adiabatic RF spin-flipper, neutron guides, the ion chamber, room temperature and cryogenic magnetic shielding, room temperature solid and liquid targets, and the liquid helium target. As the spin-rotation apparatus was assembled at NIST, detailed measurements of beam wavelength distribution, divergence, and fluence rates as well as beam imaging were performed at various positions along the neutron polarimeter. These measurements of the neutron beam and the performance of the polarimeter are necessary to set limits on various classes of possible systematic effects.

The wavelength distribution of the neutron beam is measured using a detector consisting of Bicron BC-702 Thermal Neutron Scintillator coupled to a photomultiplier tube (PMT), which is positioned downstream of a chopper spinning at 60 Hz. The output from the PMT passes through a pre-amp, a discriminator, gate and delay, and is converted to TTL; this signal inputs into a multichannel scaler. A photodiode next to the detector triggers the scaler when it detects light from a LED that passes through the

chopper aperture. The wavelength distribution is generated from count rates from the scaler.

	Total flux (neutrons / cm^2 s)	Transmission
Before supermirror polarizer	1.2×10^9	--
After supermirror polarizer	3.1×10^8	26%
After input coil & 2 m guide	1.4×10^8	45%
After output coil & 1.25 m guide	5.3×10^7	38%
After analyzer	1.3×10^7	25%

Table 7.1: Typical neutron beam fluence rates and transmission along the polarimeter. Effective total flux is based on measurements from a calibrated fission chamber using thermal neutron capture flux. The target region contained an evacuated room temperature vac-canister.

Beam divergence was measured by collimating the beam with a 0.33 cm diameter hole and taking a beam image at some distance downstream. The diameter of the beam image and the distance from the collimation determined the divergence.

Fluence rates are measured using flux monitors: the LND 3003 uncalibrated fission chamber ("papa bear") and the NIST calibrated fission chamber ("baby bear"). As apparatus components are installed on the beam line, each is aligned using a theodolite. Then, by "rocking" the component through a small angle and measuring the flux rates with a fission chamber, the optimal throughput is determined. Transmission rates along the apparatus are determined by fluence rates before and after a component and are summarized in Table 7.1.

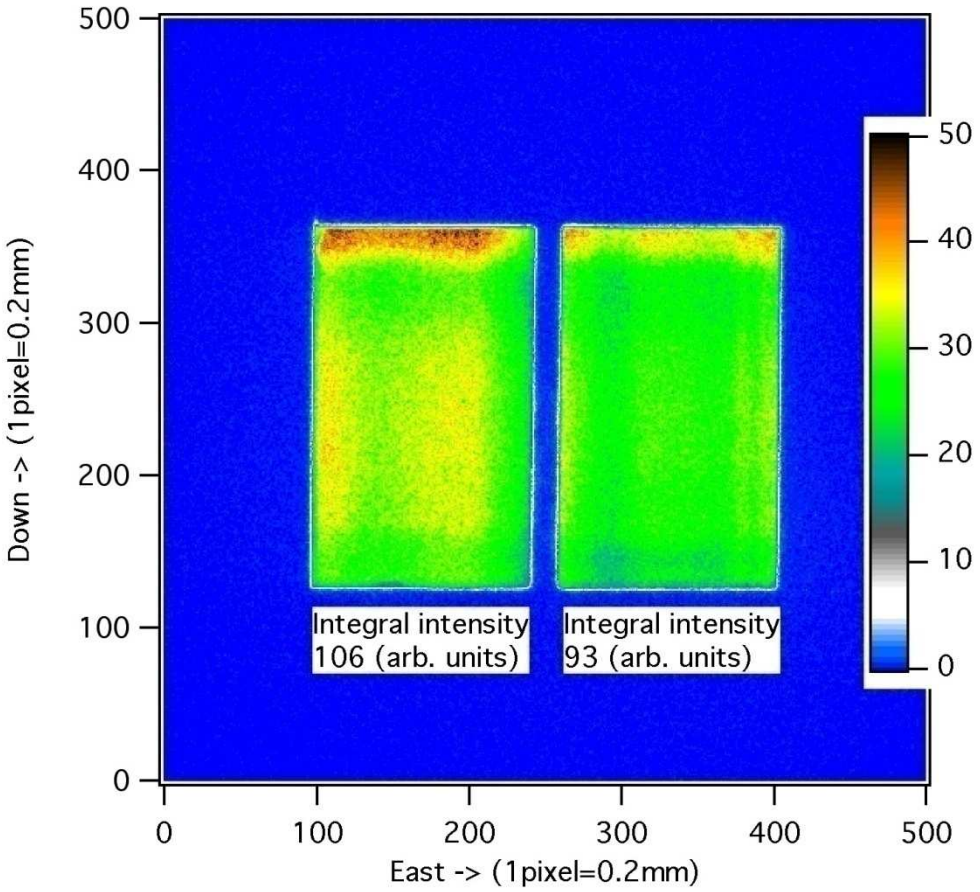

Figure 7.1: Image of the neutron beam intensity downstream of the output coil. Be and Bi filters were cold, and the neutron guides had helium gas flow. The target region contained an evacuated vac-canister at room temperature.

Dysprosium foils were used to image the beam. These images are used for surveying the beam path and observing intensity distributions within beam phase space at interesting points through the polarimeter. For instance, images show well-defined beam edges and partitioning from collimation along the polarimeter as seen in Figure 7.1.

7.2 Setting polarimeter parameters

Setting up the polarimeter for data-taking requires a set of procedures to ensure that the apparatus is aligned and optimized. Since adjusting one system will probably affect a different system elsewhere in the apparatus, the procedures are designed to be iterative in nature and should converge to optimal running parameters.

At the heart of the spin-rotation apparatus is the pi-coil, which generates an internal field that defines the vertical axis ($\hat{x}$-direction) for the entire polarimeter. The input coil is positioned so that the spin-rotation angle, as measured by count rate asymmetry, is independent of pi-coil current, and then the input coil is rotated until the change in the measured asymmetry between the pi-coil on and off states is minimized. The spin coil is then energized and rotated to a position that further minimizes the change in count rate asymmetry for the pi-coil states. Then, the output coil is rotated to minimize measured background rotations. Once the coils and guides are positioned, the polarization analyzer is positioned to transmit roughly equal signal to the left and right sides of the detector, which is positioned to minimize the cross-talk between the left and right side signal and to ensure that the beam is incident normal to the detector.

The choice of pi-coil current determines the magnetic precession angle, which is wavelength dependent. However, since the neutron beam is polychromatic, many neutrons will be either under-rotated or over-rotated. The nominal current is therefore set to rotate the mean wavelength by π radians.

Experimentally, this is determined by measuring the asymmetry as a function of pi-coil current for each plate in the detector over a range of currents. The longitudinal segmentation of the ion chamber provides wavelength distribution information about the neutron beam spectrum as a function of detector plate. Plates 2 and 3 collect charge from those neutrons close to the mean wavelength, while plate 1 collects charge from longer wavelength neutrons and plate 4 collects charge from shorter wavelength neutrons (see Figure 5.14 for plate numbering). The optimized pi-coil current produces a minimum

asymmetry for plates 2 and 3, and therefore precesses the majority of the beam $\pi \pm \pi/4$ radians.

After the polarimeter is aligned and the pi-coil current is set, the polarization product is measured (see Chapter 4). The measured count rate asymmetry is the product of the neutron polarization from the supermirror polarizer *P*, the analyzing power of the polarization analyzer *A*, and the neutron spin-rotation angle φ:

$$\frac{N_+ - N_-}{N_+ + N_-} = PA \sin\varphi \tag{7.1}$$

The polarization product is determined by measuring the count rate asymmetry for a spin-rotation angle that is large relative to a rotation caused by residual magnetic fields in the target region. This large spin-rotation angle is produced by rotating the input coil out of alignment by a few degrees. A second asymmetry measurement is made with the input coil rotated out of alignment by a few degrees in the opposite direction as the first. By taking a ratio of the asymmetry difference between the two coil positions to the angular difference between coil positions, the accuracy of the polarization product measurement is increased:

$$PA = \left(\left(\frac{N_+ - N_-}{N_+ + N_-}\right)_1 - \left(\frac{N_+ - N_-}{N_+ + N_-}\right)_2\right) / (\sin\varphi_1 - \sin\varphi_2) \tag{7.2}$$

The angle between clockwise and anticlockwise positions is about 4 ½ degrees. The angular position of the input coil is measured using a micrometer mounted to the input cradle and support frame. The difference measurement is independent of the exact angle for each position and reproducible to an estimated one part in 10^3. Instead of the input coil, the spin coil can be rotated for polarization product measurements. It is mounted separately from the input coil and designed to rotate through 9 degrees.

For a measurement of the polarization product using 0.01% counting statistics, the room-temperature solid targets require about 4 minutes of beam time. The room-

temperature liquid targets require about 400 minutes of beam time each because of scattering effects. The liquid helium target demonstrates less scattering, but the measurement requires time-consuming target state changes and so requires approximately 40 minutes of beam time with the current duty cycle timing.

At this point, the magnetic fields in the target are minimized. Time-varying fields from the guide hall environment are suppressed with a set of compensation coils that are mounted around the outer magnetic shields. A fluxgate magnetometer sensor continuously measures the residual field between the cryostat and the outer magnetic shields. A PID controller uses this field measurement as a sense feedback for controlling the current supply that feeds the coils and is set to minimize the average field in the target region as measured by the fluxgate sensors on the target.

Next, the current supplies for the trim coils mounted around the vac-canister are adjusted to generate a static offset field that nulls the average of measurements for the four fluxgate magnetometer sensors (*M0*, *M1*, *M2*, *M3*) that are located on the target. The averaged residual field strength can also be determined from neutron spin angle data. The current supplies are then adjusted for the trim coils to produce an additional gradient field that equalizes the averaged value of the upstream sensors ($(M0 + M1)/2$) and the averaged value of the downstream sensors ($(M2 + M3)/2$).

7.3 Systematic checks with room temperature targets

The spin-rotation apparatus was tested through an extensive series of measurements using room temperature targets. These tests began with straightforward measurements for checking the operation of the polarimeter, and extended into studies of possible systematic effects that were expected to be seen during operation with the liquid helium target. Well-chosen room temperature targets were used to study certain systematic effects whose size would be amplified by the nature of the target. The sizes of these systematics could then be scaled down and bound for the liquid helium target.

7.3.1 Solid target studies

As an initial check of the status of the polarimeter, a 1 cm thick, machined 6061 aluminum block was connected to a pneumatic driven linear actuator, which translated the aluminum block left and right within a room-temperature vacuum chamber of similar properties as the vac-canister. Upstream of the aluminum target, a collimator was positioned that split the beam into two separate left and right halves. The pi-coil was mounted downstream of the target in roughly the same location it would be for the liquid helium target configuration, and the vacuum chamber was mounted in the target region where the vac-canister would eventually be supported inside of the cryostat. The air control valves were computer-controlled by a program that operated the movement sequence.

No parity-violating spin angle was measured for the aluminum target at the 10^{-6} rad/m level. This implies that the combined thicknesses of neutron beam windows in the target region and the aluminum core of the pi-coil will not create a false parity-violating signal in subsequent measurements of other targets at the design sensitivity.

Additional solid targets – tin, lead, and lanthanum – were machined to a thickness of order 1 cm, but measurements in these targets proved difficult. First, the systematic error associated with a difference in target length when coupled to a residual magnetic field for the liquid helium target is $\Delta L < 0.01$ mm (see Section 4.2.3). For a target length of order 1 cm, the required ΔL is less than 1 μm. The targets were not machined to that precision, and the apparatus designed to move the targets across the beam was not designed for kinematic movement.

However, a more serious issue for these targets is that the NG6 beam is a polychromatic beam, and the Bragg cutoff for these targets is typically around 5 Å. The path length for those neutrons that Bragg scatter within the target increases. This fundamentally prevents any precision measurement of parity-violating neutron spin rotation in solid targets on the NG6 polychromatic beam.

7.3.2 Room-temperature liquid target studies

Once the room temperature solid targets had been studied, the apparatus was reconfigured to operate with room-temperature liquid targets. A sealed aluminum vessel was fashioned with quartz beam windows epoxied to upstream and downstream faces. A thin septum separates the inner volume into left and right cells, and a small hole at the bottom of the septum connects these cells (see Figure 7.2). Teflon tubing connects into vent holes above each cell. The liquid target assembly was filled and mounted within the vac-canister, with beam collimation placed upstream and the pi-coil placed downstream of the target. The vac-canister was positioned in the target region as before.

The Teflon tubes were connected to a computer-controlled gas handling system, which pressurized one of the target cells and released pressure on the other cell. This has the effect of filling one cell with liquid and emptying the other cell, to the extent that the collimated neutron beam is incident on the cells. Alternately, pressurizing and venting cells performs the same function as mechanically moving a target transversely across a beam, but with much better positional repeatability, since the vessel that defines the cell volumes does not move.

Measurements were then performed with liquid D_2O and liquid tetrachloroethylene (C_2Cl_4) targets in order to amplify certain systematic effects by two to three orders of magnitude over what was expected for the liquid helium target. D_2O was chosen to test small angle scattering systematics and C_2Cl_4 to amplify effects from the neutron spectrum change.

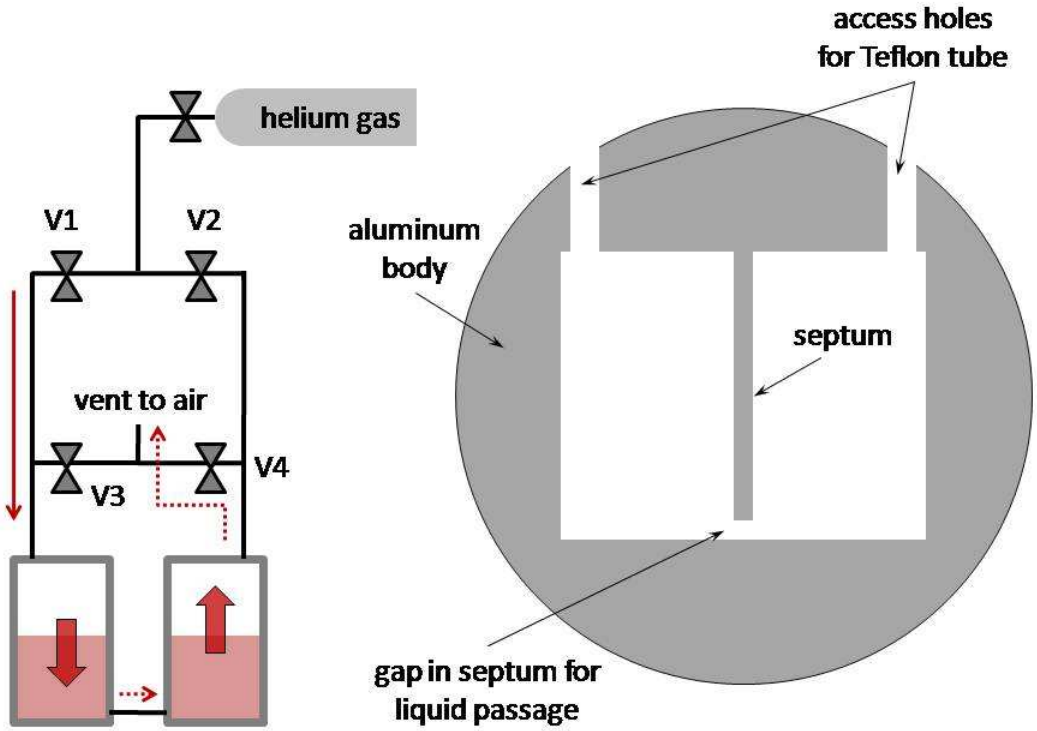

Figure 7.2: Diagram of the room temperature liquid target system. A cross-section on the right shows the aluminum container that holds the liquid in left and right side cells. A gas handling system applies overpressure to one cell by opening valve V1 and vents the other cell to air by opening valve V4. Once the liquid has moved from the higher pressure cell, the valves are closed and the pressure difference keeps the liquid in one cell for the duration of the measurement. Opening the other set of valves (V2, V3) reverses the direction of gas flow, and fills the other cell in the same manner.

During the liquid D_2O runs, a downstream tilt of the neutron polarization vector from vertical ($+\hat{y}$) of about 10 mrad was detected in the beam once it exited the neutron supermirror polarizer. This tilt was undetected in previous beam characterization measurements, which were not sensitive to quadratic effects. This small polarization tilt couples with non-forward scattering in the targets to give a nonzero apparent parity-violating correlation that is visible when the pi-coil is powered off. To correct this, a secondary neutron precession coil (the "spin coil") is mounted on the downstream face of the input coil. After installation, measurements show that this effect is suppressed while leaving unchanged a systematic effect believed to be caused by neutron scattering in the targets.

Other measurements performed with the liquid D_2O target used a 1 mG internally-generated longitudinal magnetic field to demonstrate that the size of the systematic effects due to small angle neutron scattering coupled with residual fields scales with the residual internal longitudinal magnetic field as expected. The results can then be scaled down to a smaller residual field, thus establishing an upper limit on such effects in the liquid helium target, where scattering effects are expected to be much lower for a given field strength.

However, measurements with liquid D_2O and liquid C_2Cl_4 demonstrate that small angle neutron scattering within these targets is a large effect. Additionally, one of the same difficulties with the solid targets is a problem with these liquid targets – namely, target length difference. The beam windows were attached to the target body using resin epoxy, which was not applied and cured in a manner that ensured a precision thickness. The thickness of the liquid formed by the target cell was of order 1 cm. By using the same arguments as the solid targets, the liquid targets could not have had the required precision to suppress systematic effects associated with target length differences.

7.3.3 Liquid helium target

Once the studies with the room-temperature liquid targets were complete, the liquid helium target apparatus was assembled on the beam line. The cryostat was mounted on the apparatus frame and the outer magnetic shields installed around it. Neutron guides and spin transport were then installed, and the polarimeter was aligned to the previously surveyed beam path. The target insert was mounted into the cryostat cold bore, and the spin-rotation apparatus was adjusted so that the beam passes through the geometric center of the liquid helium target as sighted by a theodolite. Polarimeter parameters were then set by the methodology as described in Section 7.2.

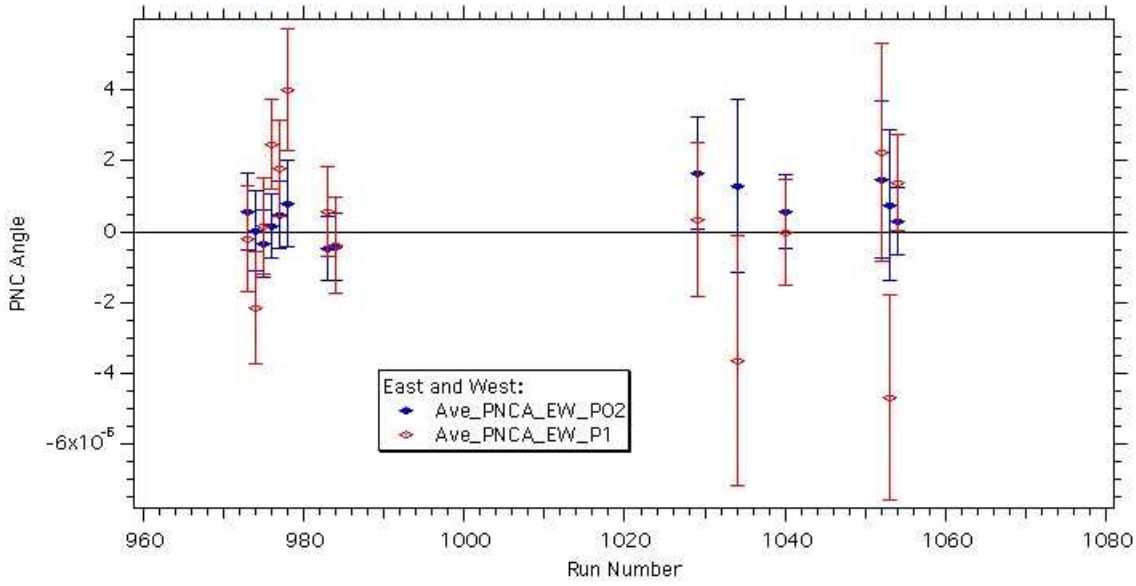

Figure 7.3: Plot of parity-violating spin angles for liquid helium target null runs.

After cooling the cryostat and liquid helium target to 4K, the target was emptied of any liquid, and a series of data runs were taken to ensure that the empty target produced zero parity-violating spin angle. As of mid-January of 2008, 7.3 days of live time were collected over 14 runs under various thermal conditions ranging from 4K to room temperature as shown in Figure 7.3. The weighted average parity-violating angle for the pi-coil:ON state was $(5.8 \pm 7.5) \times 10^{-7}$ rad/m and for the pi-coil:OFF state was

$(1.5 \pm 1.1) \times 10^{-6}$ rad/m. These measurements are preliminary and have not been corrected for the polarization product. Additional offline analysis is ongoing.

7.4 Data acquisition and control

Data were taken for each state of the apparatus as determined by target state, pi-coil current, output coil flipping state, spin coil voltage, and RF spin-flipper state (see Figure 7.4 for sequence). Erik Swanson wrote the computer control and data acquisition program – the NSAC (Neutron Spin-Rotation Acquisition and Control) – that directed the control sequence for the apparatus and managed the data retrieval and storage. The software was written entirely in Visual C++ using National Instruments Lab Windows CVI 7.0 for the graphical user interface (GUI) routines and the routines that interact with National Instruments hardware.

The NSAC program flipped the output coil state and initiated the charge collection routine depicted in Figure 5.17. Since the integrator voltage was read at the initiation and termination of the charge collection interval, the recorded signal was proportional to the current accumulated during a specified amount of time, for a designated state of the apparatus, and was independent of voltage offsets.

Timing is synchronized to hardware clocks on the DAQ board, which is set up to read and buffer selected ADC channels at a periodic rate. Once this operation is complete, the DAQ board raises a flag that is detected by a C++ thread running at the highest system priority with millisecond precision, which then initiates a transfer of the buffered ADC reads into memory. This happens at a 10 Hz rate.

After nine read cycles (900 ms), the current in the output coil is set to its new value. One read cycle (100 ms) is dedicated to letting the field transients settle before starting the integration period. This fixes the acquisition dead time at 10%. Within this period, the NSAC program enables the RESET of the integrators, but the actual time of RESET is determined by the hardware clock on the DAQ board. The charge is then determined

by the difference is the $t = 0$ and $t = 0.9$ s reads. Keeping the RESET synchronized to the same clock as the reads is important because internal leakage in the integrators contributes a non-linearity when the ion chamber currents are low. If the East-West asymmetry were perfect, the signal would be insensitive to this.

At the end of the ten read cycle sequence, a new data point is generated and written to disk. This data acquisition and control scheme works with modern PC's but clearly the faster the computer, the better. The most dependency on CPU speed is in the performance of the GUI and not the actual acquisition of the data.

A specified number of output coil flips constitute each pi-coil state. A pi-coil cycle is built by sequentially stepping through the three different pi-coil states $(+,0,-)$ for a given target state. Five pi-coil cycles are run in sequence, and then the target state is switched by initiating the target changeover sequence. The completion of five pi-coil cycles, a target change, another five pi-coil cycles, and another target change constitute a target cycle (see Figure 7.4), at which point the NSAC program calculates such values as target asymmetry and spin angles.

For most data runs, we ran with 10 output coil flips per pi-coil state for a total of 300 seconds of data acquisition for each target state. The 350 seconds of dead time associated with the target changeover sequence imposed a practical limit to the length of the target state.

The target changeover sequence begins by energizing all instrumentation in the target. The drainpipes associated with the full target chambers from the previous target state are lowered. The centrifugal pump spins up and begins filling all four target chambers. The liquid helium entering chambers with lowered drainpipes fills slowly (if at all) as compared to the chambers with raised drainpipes. Liquid level sensors continuously monitor the status of the fill for each target chamber as well as the liquid helium bath.

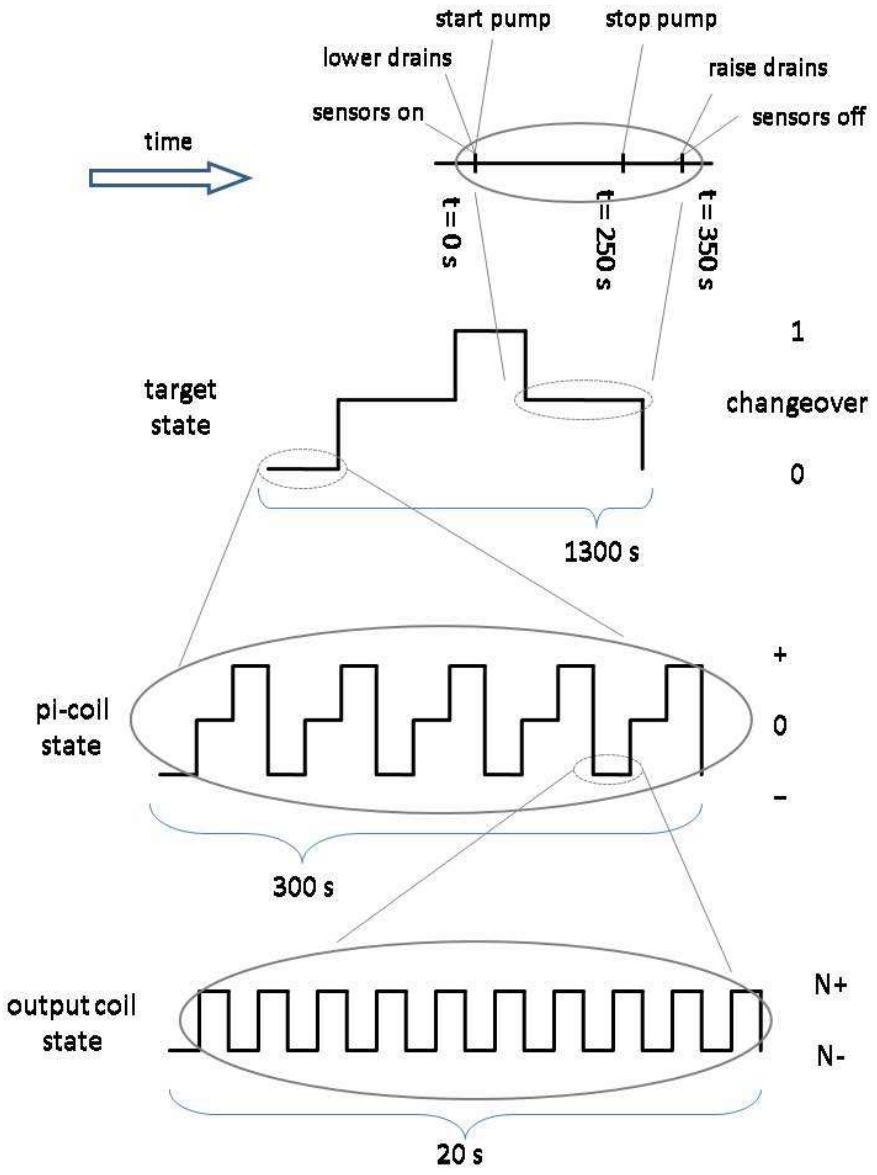

Figure 7.4: Diagram of the polarimeter control sequence. For a data run, target cycles are repeated until the run is terminated.

After a predetermined time in which the target chambers with raised drainpipes should be full of liquid helium, the centrifugal pump stops. Another predetermined amount of time passes while target chambers with lowered drainpipes empty out completely. This drain time also allows turbulence to subside, the temperature in the target to equilibrate, and bubbles to settle out so that the liquid helium density can become homogeneous. The length of these predetermined times are conservative estimates based on previously measured target fill and drain times. The current pump time is 250 seconds and drain time is 100 seconds. Once the drain time is over, all instrumentation in the target is powered off, and the drainpipes are raised; the target is now in the new state, and data acquisition can resume.

The target state is determined by which drainpipe is lowered during the target changeover sequence. For our configuration, target state 0 corresponds to full target chambers on the upstream east and the downstream west side. The neutrons travel north in the beam line. Target state 1 corresponds to the other two chambers filled; upstream west side and downstream east side.

Two primary modes of acquisition were used. The data acquisition mode cycled through the polarimeter states during normal data collection runs. For measuring the polarization product of the polarimeter, the program executed the measurement sequence described in Section 7.2 by prompting the experimenter to rotate the input coil and enter its position.

For some runs, the drainpipe actuator control leads are exchanged, which reverses the target assignments and changes which set of chambers is filled first in the target cycle. Similarly, the assignment of the pi-coil states is changed by reversing the pi-coil leads. Many possible spurious or correlated effects are removed by averaging the results taken with randomly altered sequencing of the states of the system.

7.5 Experimental difficulties

There is a large dead time in the current data-taking sequence. This is partly due to the lengthy fill and drain times of the target chambers. The fill time is 250 seconds and the drain time is 100 seconds, while the data taken for a given target state is 300 seconds, which gives a dead time of 54%. The fill and drain times are purposefully set longer than required to ensure that target chambers are definitely full or empty. These times could be relaxed slightly, and the fill time for the target chambers could be lowered by increasing the centrifugal pump rate.

The liquid helium hold time during which the target levels operate within a data taking range is about 6 hours. We have operated with three fills per day, which means with the previous dead time, we get about 3 hours per fill or 9 hours of data per day. This ignores filling through the impedance or increasing the hold time. Given that the current heat load on the insert is unlikely to be significantly reduced below current levels, adjusting the impedance of the capillary seems the best way to increase the hold time of the target insert. However, pumping on the insert to make an pressure difference between it and the liquid helium annular volume has not increased the hold time. In fact, it has the opposite effect, as the hold time is reduced to 2 hours. Applying overpressure on the liquid helium annular volume or increasing the impedance of the capillary seems like the next practical choice.

The magnetic fields in the target region are larger in amplitude than those observed at room temperature without active suppression. Therefore, the cold apparatus sees the change in fields. The magnitude of the field needs to be minimized, the temporal gradient of the field needs to be eliminated, or the fluctuation seen by the fluxgate sensors need to be canceled, or a combination of all three.

Cryogenic and vacuum issues are a constant threat. A loose indium seal on one of the vac-canister beam windows required about 10 days to diagnose and repair. Transfer hoses on several occasions have become frozen within the liquid helium fill stack on the

cryostat, and had to either remain in place for several hours or were warmed with a heat gun until they thawed enough for extraction.

Our ability to acquire data has been compromised by ice entering the motion-control feedthrough and seizing the motion-control strings and pump driveshaft, and entering the pump-out feedthrough and blocking the liquid helium transfer line. These situations require warming-up the target insert to purge the ice.

8 Data Analysis and Results

The NSAC program allows online analysis during a run by computing the asymmetries and ratios of these asymmetries of completed target cycles for specified polarimeter parameters. The asymmetry A is defined as the difference over the sum:

$$A_P^T(D) = \frac{\bar{N}^+(D,T,P) - \bar{N}^-(D,T,P)}{\bar{N}^+(D,T,P) + \bar{N}^-(D,T,P)} \tag{8.1}$$

where D signifies a part of the detector (e.g. west side), T denotes the target state (T0, T1), and P stands for the pi-coil states (P0, P1, P2 with P1 being the zero-current state). The sum of all reads for one complete sequence with the output coil in state 0 is given by $\bar{N}^+(D,T,P)$, where the polarimeter states are represented by variables D, T, and P which each having the same value. Similarly, $\bar{N}^-(D,T,P)$ corresponds to a sum with the output coil in state 1. For asymmetries and ratios, the mean values of the reads and their sums are equivalent.

The spin angles involve averages of the asymmetries. They are calculated for both the pi-coil:ON and pi-coil:OFF states. For pi-coil:ON, the asymmetries for the P0 and P2 states are averaged together.

$$\text{spin angle west}\left(\text{pi-coil:ON}\right) = \frac{1}{4}\left(A_{P0}^{T0}(W) + A_{P0}^{T1}(W) + A_{P2}^{T0}(W) + A_{P0}^{T1}(W)\right) \tag{8.2}$$

$$\text{spin angle east}\left(\text{pi-coil:ON}\right) = \frac{1}{4}\left(A_{P0}^{T0}(E) + A_{P0}^{T1}(E) + A_{P2}^{T0}(E) + A_{P0}^{T1}(E)\right) \tag{8.3}$$

$$\text{spin angle total}\left(\text{pi-coil:ON}\right) = \frac{1}{2}\begin{pmatrix}\text{spin angle west}\left(\text{pi-coil:ON}\right) \\ +\ \text{spin angle east}\left(\text{pi-coil:ON}\right)\end{pmatrix} \tag{8.4}$$

$$\text{spin angle west}\left(\text{pi-coil:OFF}\right) = \frac{1}{2}\left(A_{P1}^{T0}(W) + A_{P1}^{T1}(W)\right) \tag{8.5}$$

$$\text{spin angle east}\left(\text{pi-coil:OFF}\right) = \frac{1}{2}\left(A_{P1}^{T0}(E) + A_{P1}^{T1}(E)\right) \tag{8.6}$$

$$\text{spin angle total}\left(\text{pi-coil:OFF}\right) = \frac{1}{2}\begin{pmatrix}\text{spin angle west}\left(\text{pi-coil:OFF}\right)\\ +\ \text{spin angle east}\left(\text{pi-coil:OFF}\right)\end{pmatrix} \tag{8.7}$$

On the other hand, the parity-violating (PV) angles involve differences in asymmetries of the detector halves and target states, since the measured parity-violating angle changes sign depending on the east / west half of the detector and the target state.

$$\text{PV angle west}\left(\text{pi-coil:ON}\right) = \frac{1}{4}\left(A_{P0}^{T0}(W) - A_{P0}^{T1}(W) + A_{P2}^{T0}(W) - A_{P0}^{T1}(W)\right) \tag{8.8}$$

$$\text{PV angle east}\left(\text{pi-coil:ON}\right) = \frac{1}{4}\left(A_{P0}^{T0}(E) - A_{P0}^{T1}(E) + A_{P2}^{T0}(E) - A_{P0}^{T1}(E)\right) \tag{8.9}$$

$$\text{PV angle total}\left(\text{pi-coil:ON}\right) = \frac{1}{2}\begin{pmatrix}\text{PV angle west}\left(\text{pi-coil:ON}\right)\\ +\ \text{PV angle east}\left(\text{pi-coil:ON}\right)\end{pmatrix} \tag{8.10}$$

$$\text{PV angle west}\left(\text{pi-coil:OFF}\right) = \frac{1}{4}\left(A_{P1}^{T0}(W) - A_{P1}^{T1}(W)\right) \tag{8.11}$$

$$\text{PV angle east}\left(\text{pi-coil:OFF}\right) = \frac{1}{4}\left(A_{P1}^{T0}(E) - A_{P1}^{T1}(E)\right) \tag{8.12}$$

$$\text{PV angle total}\left(\text{pi-coil:OFF}\right) = \frac{1}{2}\begin{pmatrix}\text{PV angle west}\left(\text{pi-coil:OFF}\right)\\ +\ \text{PV angle east}\left(\text{pi-coil:OFF}\right)\end{pmatrix} \tag{8.13}$$

8.1 Preliminary results for the liquid helium target

The current data set for the liquid helium target through mid-January 2008 uses 1.5 days of live time collected from 18 runs over 3.2 days of beam time over 16 calendar days as shown in Figure 8.1. These runs have spin coil settings of $+10\ V$, $-10\ V$, and no spin coil energized. The parity-violating spin angle for the pi-coil:ON states was measured as $(-5.0 \pm 18.8) \times 10^{-7}$ rad/m. The parity-violating spin angle for pi-coil:OFF state was measured as $(4.8 \pm 2.3) \times 10^{-6}$ rad/m. These are weighted averages for all runs and have not been corrected for polarization product. These results are preliminary and require additional statistics from the ongoing measurement as well as additional offline analysis.

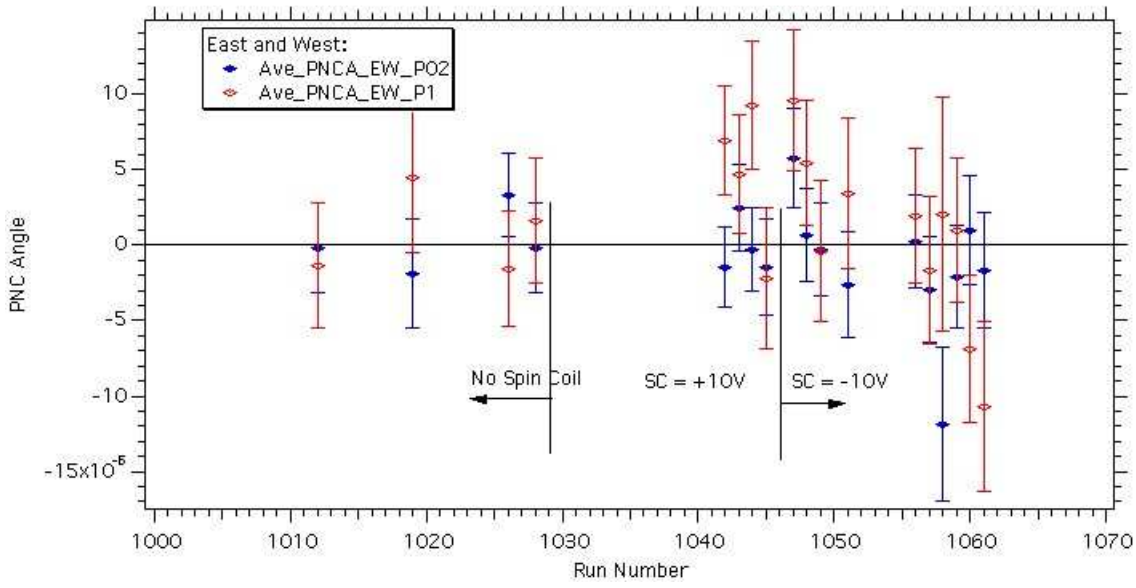

Figure 8.1: Plot of the parity-violating spin angles for liquid helium target. Blue data represent averaged values for opposite polarity pi-coil-on states, and red represent pi-coil-off states.

9 Discussion

The preliminary data from the parity-violating neutron spin rotation of cold neutrons through a 42 cm long liquid helium target give a measurement of:

$$\varphi_{PV}\left(\vec{n},\ ^4\mathrm{He}\right) = (-5.0 \pm 18.8\ [\mathrm{stat}]) \times 10^{-7}\ \mathrm{rad/m}$$

which does not include corrections due to polarization product or systematic error.

9.1 New constraints on nucleon-meson weak couplings

As of mid-January 2008, not enough statistics have been collected during the first three weeks of data-collection to attain the precision required to further constrain any of the nucleon-meson weak couplings from their current experimental values. Additional run time for this ongoing experiment is required to improve the statistical accuracy of the measurement.

9.2 Spin rotation in liquid helium at the SNS

There are a number of advantages that the pulsed neutron beam at the SNS will possess for the suppression of systematic effects in future spin-rotation measurements. Among the advantages are the following:

The magnitude of the pi-coil field can be ramped in phase with the SNS source to precess the polarization of all neutrons in a broad velocity class by π radians. At NIST, where one must accept a large range of neutron velocities to increase counting statistics and compromise by choosing a mean magnetic field in the pi-coil that over-rotates the slower neutrons and under-rotates the faster neutrons in the velocity distribution, the size of the signal in the polarization analyzer is reduced by a factor of two. This reduction will not be present at the SNS. In addition, the neutron velocity spread at the SNS is

narrow enough (~1%) that one can use higher fields in the pi-coil to precess the neutrons by both π and 3π radians. This will increase any non-vertical fields from the pi-coil and their possible associated systematic effects by a factor of three, thereby making a much cleaner test for possible systematic effects from non-ideal internal pi-coil fields. This very valuable test is done less efficiently at a steady-state neutron source, since neutron velocities would need to be restricted in a narrower region.

The parity-violating spin-rotation signal is independent of neutron velocity in the cold and thermal neutron range of energies. However, the rotation due to residual magnetic fields, which depends on the time spent in the field and is the most significant source of systematic error, is proportional to $1/v$. Therefore, the data can be analyzed simply as a function of neutron time-of-flight to confirm the absence of magnetic field effects. Relative changes in the internal magnetic fields as recorded by magnetometers inside the target can be correlated with neutron time-of-flight and therefore neutron energy, which allows the possibility to remove effects of any magnetic noise. Although a similar test is possible at a steady-state source using the $1/v$ absorption of the ion chamber, it is less sensitive.

The systematic effects that might depend on small angle scattering of the neutrons in the target are a strong function of neutron energy in the cold neutron energy regime. Such effects can be artificially amplified by increasing the internal magnetic field in the target region and looking for a difference between the upstream and downstream spin-rotation signals. The same test performed at a steady-state source possesses less diagnostic information due to the absence of neutron energy information.

The presence of stated magnetic field policies at the SNS are sufficiently restrictive that the existing field cancellation system on the current apparatus – based on its performance experience at NIST – would be more than sufficient to suppress noise in the neutron polarimetry from fluctuating fields at the required 1×10^{-7} level.

9.3 Spin rotation in liquid hydrogen

The most fundamental system for studying the nucleon-nucleon weak interaction is $\vec{n} + p$. While the parity-violating neutron spin rotation in hydrogen is sensitive to isovector and isoscalar nucleon-meson weak couplings, the isovector coupling term f_π is expected to dominate. The rotary power of spin rotation in parahydrogen is predicted to be larger than that for helium – in the range $(0 - 9) \times 10^{-7}$ rad/m [94] – but the neutron scattering within a parahydrogen target would be larger as well, and so would decrease the available neutron counting statistics. For a two-sigma target length of 15 cm, a measurable signal with a decent neutron count rate could be resolved with a measurement sensitivity of less than 5×10^{-8} rad/m. Additionally, the spin-rotation measurement in helium would provide invaluable experimental experience with the neutron polarimeter and cryogenics apparatus that would be similar to that needed for a measurement in a liquid parahydrogen target.

References

[1] D. Griffiths, *Introduction to Elementary Particles* (John Wiley & Sons, Inc, New York, 1987).

[2] T. D. Lee, and C. N. Yang, Phys. Rev. **104**, 254 (1956).

[3] C. S. Wu *et al.*, Phys. Rev. **105**, 1413 (1957).

[4] B. Heckel *et al.*, Phys. Lett. B **119**, 298 (1982).

[5] B. Heckel *et al.*, Phys. Rev. C **29**, 2389 (1984).

[6] M. J. Ramsey-Musolf, and S. A. Page, Ann. Rev. Nucl. Part. Sci. **56**, 1 (2006).

[7] F. Halzen, and A. D. Martin, *Quarks & Leptons: An Introductory Course in Modern Particle Physics* (John Wiley & Sons, Inc., 1984).

[8] G. Arnison, Phys. Lett. B **166**, 484 (1986).

[9] G. Arnison, Z. Phys. C **30**, 1 (1986).

[10] G. Arnison, Z. Phys. C **47**, 11 (1990).

[11] F. Abe, Phys. Rev. D **44**, 29 (1991).

[12] S. Abachi *et al.*, Phys. Rev. Lett. **75**, 1456 (1995).

[13] C. S. Wood *et al.*, Science **275**, 1759 (1997).

[14] E. G. Adelberger, and W. C. Haxton, Ann. Rev. Nucl. Part. Sci. **35**, 501 (1985).

[15] W. Haeberli, and B. R. Holstein, in *Symmetries and Fundamental Interactions in Nuclei*, edited by W. C. Haxton, and E. M. Henly (World Scientific, Singapore, 1995).

[16] C.-P. Liu, Phys. Rev. C **75**, 065501 (2007).

[17] B. R. Holstein, Fizika B **14**, 165 (2005).

[18] S. L. Zhu *et al.*, Nucl. Phys. A **748**, 435 (2005).

[19] B. Desplanques, J. F. Donoghue, and B. R. Holstein, Ann. Phys. **124**, 449 (1980).

[20] R. Machleidt, in *Advances in Nuclear Physics*, edited by J. W. Negele, and E. Vogt (Plenum Press, New York, 1989), pp. 189.

[21] B. Desplanques, Phys. Rep. **297**, 1 (1998).

[22] U.-G. Meissner, and H. Weigel, Phys. Lett. B **447**, 1 (1999).

[23] D. B. Kaplan, and M. J. Savage, Nucl. Phys. A **556**, 653 (1993).

[24] E. M. Henley, W.-Y. P. Hwang, and L. S. Kisslinger, Phys. Lett. B **440**, 449 (1998).

[25] S. Kistryn, and e. al., Phys. Rev. Lett. **58**, 1616 (1987).

[26] J. Lang *et al.*, Phys. Rev. C **34**, 1545 (1986).

[27] C. A. Barnes *et al.*, Phys. Rev. Lett. **40**, 840 (1978).

[28] P. G. Bizetti, Lett. Nuovo Cim. **29**, 167 (1980).

[29] G. Ahrens *et al.*, Nucl. Phys. A **390**, 486 (1982).

[30] E. G. Adelberger, and W. C. Haxton, Ann. Rev. Nucl. Part. Sci. **35**, 501 (1983).

[31] K. Elsener *et al.*, Phys. Rev. Lett. **52**, 1476 (1984).

[32] V. V. Flambaum, and D. W. Murray, Phys. Rev. C **56**, 1641 (1997).

[33] W. S. Wilburn, and J. D. Bowman, Phys. Rev. C **57**, 3425 (1998).

[34] D. M. Markoff, *Measurement of the Parity Nonconserving Spin-Rotation of Transmitted Cold Neutrons Through a Liquid Helium Target* (PhD Thesis, University of Washington, Seattle, 1997).

[35] B. R. Holstein, *Weak Interactions in Physics* (Princeton University Press, Princeton, 1989).

[36] G. Barton, Il Nuovo Cim. **19**, 512 (1961).

[37] G. S. Danilov, Phys. Lett **18**, 40 (1965).

[38] S. R. Beane, and M. J. Savage, Nucl. Phys. B **636**, 291 (2002).

[39] B. Desplanques, Nucl. Phys. A **242**, 423 (1975).

[40] B. Desplanques, Nucl. Phys. A **335**, 147 (1980).

[41] B. Desplanques, Phys. Lett. B **512**, 305 (2001).

[42] R. Schiavilla, J. Carlson, and M. Paris, Phys. Rev. C **67**, 032501 (2003).

[43] R. Schiavilla, J. Carlson, and M. Paris, Phys. Rev. C **70**, 044007 (2004).

[44] E. Hadjimichael, E. Harms, and V. Newton, Phys. Rev. Lett **27**, 1322 (1971).

[45] V. F. Dmitriev *et al.*, Phys. Lett. **125**, 1 (1983).

[46] L. Stodolsky, Phys. Lett. **50B**, 352 (1974).

[47] M. Forte *et al.*, Phys. Rev. Lett. **45**, 2088 (1980).

[48] B. R. Heckel, *Parity Non-Conserving Neutron Spin Rotation* (PhD Thesis, Harvard University, Cambridge, 1981).

[49] S. Saha, (PhD Thesis, University of Washington, Seattle, 1990).

[50] M. Bini *et al.*, Phys. Rev. Lett. **55**, 795 (1985).

[51] H. C. Evans, Phys. Rev. Lett. **55**, 791 (1965).

[52] E. D. Earle *et al.*, Nucl. Phys. A **396**, 221 (1983).

[53] K. A. Snover *et al.*, Physical Review Letters **41**, 145 (1978).

[54] E. G. Adelberger, AIP Conf. Proc. **69**, 1367 (1981).

[55] E. G. Adelberger *et al.*, Phys. Rev. C **27**, 2833 (1983).

[56] K. Elsener *et al.*, Phys. Lett. B **117**, 167 (1982).

[57] K. Neubeck, H. Schober, and H. Waffler, Phys. Rev. C **10**, 320 (1974).

[58] N. Kniest *et al.*, Phys. Rev. C **41**, R1336 (1990).

[59] J. D. Bowman *et al.*, Chinese J. Phys. **32**, 6 (1994).

[60] J. D. Bowman *et al.*, Ann. Rev. Nucl. Part. Sci. **43**, 829 (1993).

[61] P. D. Eversheim *et al.*, Phys. Lett. B **256**, 11 (1991).

[62] S. Kistryn *et al.*, Phys. Rev. Lett. **58**, 1616 (1987).

[63] J. Lang *et al.*, Phys. Rev. Lett **54**, 170 (1985).

[64] M. Horoi, and B. A. Brown, Phys. Rev. Lett. **74**, 231 (1995).

[65] B. Desplanques, Bull. APS **42** (1997).

[66] F. C. Michel, Phys. Rev. **133**, B329 (1964).

[67] D. J. Richardson, R. Golub, and S. K. Lamoreaux, *Ultra-cold Neutrons* (Adam Hilger, 1991).

[68] D. J. Hughes, *Neutron Optics* (Interscience Publishers, Inc., New York, 1954).

[69] Y. Avishai, Phys. Lett. B **112**, 311 (1982).

[70] J. S. Nico, private communication.

[71] R. E. Glick, J. Phys. Chem **65**, 1552 (1961).

[72] H. S. Sommers, J. G. Dash, and L. Goldstein, Phys. Rev. **97**, 855 (1955).

[73] Landau, and Lifshitz, *Statistical Physics, part 2* (Pergamon Press, 1980), p. 370.

[74] Y. M. Tsipenyuk, and R. P. May, arXiv: cond-mat, 02070278v1 (2002).

[75] Y. Abe, and N. Morishima, Nucl. Instrum. and Methods A **459**, 256 (2001).

[76] M. Sarsour, *Simulation for neutron spin rotation* (Neutron Spin Rotation: internal report, IUCF, Bloomington, 2004).

[77] H. P. Mumm, Rev. Sci. Instrum. **75**, 12 (2004).

[78] J. S. Nico *et al.*, J. Res. NIST **110**, 137 (2005).

[79] A. K. Freund, Nucl. Instrum. Methods **213**, 495 (1983).

[80] O. Schaerpf, Physica B **156-157**, 631 (1989).

[81] O. Schaerpf, Physica B **156-157**, 639 (1989).

[82] A. N. Bazhenov *et al.*, Nucl. Instrum. Methods A **332**, 534 (1993).

[83] S. V. Grigoriev, A. I. Okorokov, and V. V. Runov, Nucl. Instrum. Methods A **384**, 415 (1997).

[84] S. D. Penn *et al.*, Nucl. Instrum. Meth. A **457**, 332 (2001).

[85] C. S. Blessinger, *npdg H / ^{3}He ion chamber technical note* (NPDG: internal report, Indiana University, Bloomington, 2000).

[86] D. Luo, (Neutron Spin Rotation: internal report, Indiana University, Bloomington, 2004).

[87] A. M. Micherdzinska, and D. Luo, *Optimal number of detector plates* (Neutron Spin Rotation: internal report, Indiana University / IUCF, Bloomington, 2004).

[88] J. J. Niemala, and R. J. Donnelly, J Low Temp Phys **98**, 1 (1995).

[89] F. Pobell, *Matter and Methods at Low Temperatures* (Springer-Verlag, Berlin, 1996).

[90] R. C. Richardson, and E. N. Smith, *Experimental Techniques in Condensed Matter Physics at Low Temperatures* (Addison-Wesley, Reading, Massachussetts, 1998).

[91] J. C. Wheatley, Rev. Sci. Instrum. **35**, 765 (1964).

[92] J. D. Brownridge, Cryogenics **29**, 70 (1989).

[93] P. M. McConnell, in *NBSIR 73-316* (National Bureau of Standards, 1973).

[94] Y. Avishai, and P. Grange, J. Phys. G **10**, L263 (1984).

Vita Page

Christopher Dale Bass was born in 1969 in Evansville, Indiana to Terry and Patricia Bass. He earned a B.S. degree in Physics from Indiana University in 1999. He entered the graduate program at Indiana University and earned a M.S. degree in Physics in 2001. He began the physics Ph.D. program in 2001 and began work with Professor W. Michael Snow on the Neutron Spin Rotation experiment. He has accepted a NRC Postdoctoral Research position with the Fundamental Physics Group at the NCNR in Gaithersburg, Maryland.